UNIVERSIDADE DE SÃO PAULO
Escola de Engenharia de São Carlos

Contributions to a constitutive model for Ultra-High Performance Fiber-Reinforced Concrete

Contribuições para um modelo constitutivo para o concreto de altíssimo desempenho com fibras

Paula de Oliveira Ribeiro

Tese de Doutorado do Programa de Pós-Graduação em Engenharia Civil (Engenharia de Estruturas) da Escola de Engenharia de São Carlos, Universidade de São Paulo

EESC · USP

Paula de Oliveira Ribeiro

Contributions to a constitutive model for Ultra-High Performance Fiber-Reinforced Concrete

Contribuições para um modelo constitutivo para o concreto de altíssimo desempenho com fibras

CORRECTED VERSION

Original version is available at São Carlos School of Engineering

Thesis presented to the São Carlos School of Engineering, University of São Paulo, as one of the requisites for the obtaining of the Doctor's degree in Civil Engineering (Structures).

Supervisor: Associate Professor Ricardo Carrazedo

São Carlos

2023

Ficha catalográfica elaborada pela Biblioteca Prof. Dr. Sérgio Rodrigues Fontes da EESC/USP com os dados inseridos pelo(a) autor(a).

Ribeiro, Paula de Oliveira
R484c Contributions to a constitutive model for Ultra-High Performance Fiber-Reinforced Concrete / Paula de Oliveira Ribeiro; orientador Ricardo Carrazedo. São Carlos, 2023.

Tese (Doutorado) - Programa de Pós-Graduação em Engenharia Civil (Engenharia de Estruturas) e Área de Concentração em Estruturas -- Escola de Engenharia de São Carlos da Universidade de São Paulo, 2023.

1. UHPFRC. 2. Constitutive model. 3. Finite element method. I. Título.

Eduardo Graziosi Silva - CRB - 8/8907

FOLHA DE JULGAMENTO

Candidata: Engenheira **PAULA DE OLIVEIRA RIBEIRO.**

Título da tese: "Contribuições para um modelo constitutivo para o concreto de altíssimo desempenho com fibras".

Data da defesa: 01/02/2023.

Comissão Julgadora	**Resultado**
Prof. Associado **Ricardo Carrazedo (Orientador)** (Escola de Engenharia de São Carlos – EESC/USP)	APROVADA
Prof. Titular **Antonio Domingues de Figueiredo** (Escola Politécnica/EP-USP)	APROVADO
Prof. Dr. **Luís Antonio Guimarães Bitencourt Junior** (Escola Politécnica/EP-USP)	APROVADO
Prof. Dr. **Romel Dias Vanderlei** (Universidade Estadual de Maringá/UEM)	APROVADO
Prof. Associado **Vladimir Guilherme Haach** (Escola de Engenharia de São Carlos – EESC/USP)	APROVADO

Coordenador do Programa de Pós-Graduação em Engenharia Civil (Engenharia de Estruturas):
Prof. Associado **Vladimir Guilherme Haach**

Presidente da Comissão de Pós-Graduação:
Prof. Titular **Murilo Araujo Romero**

I dedicate this thesis to my parents, Sueli and Paulo.

ACKNOWLEDGEMENTS

Firstly, I would like to thank God for always being with me.

My profound gratitude to my parents, Paulo and Sueli, for all their love and dedication. I also thank my family and friends for their support.

I sincerely thank my boyfriend, Evandro, for his encouragement, patience, care, and attention.

I want to thank my advisor, Ricardo Carrazedo, for his patience, confidence and dedication, and Pablo Krahl and Caroline Oliveira for the discussions and important contributions to the research results.

My thankfulness to all the teachers who have been through my life and, in particular, to the professors who evaluated and contributed to the final version of this thesis.

My gratitude to the employees of EESC/USP for all their support and special thanks to my friends at SET. You are amazing!

Finally, I thank the National Council for Scientific and Technological Development (CNPq) for the financial support provided for this research.

Abstract

RIBEIRO, P. O. **Contributions to a constitutive model for Ultra-High Performance Fiber-Reinforced Concrete**. 2023. 159p. Thesis (Ph.D.) - São Carlos School of Engineering, University of São Paulo, São Carlos, 2023.

Ultra-High Performance Fiber-Reinforced Concrete (UHPFRC) has drawn the attention of researchers due to its high strength, ductility, and durability, enabling projects with structural elements with thinner and lighter sections. The literature reports several experimental studies focused on a better understanding of the mechanical behavior of that material. Regarding numerical models, many phenomena such as fiber distribution and orientation, fiber interaction (group effect), and anisotropic behavior must be considered. This research aims to overcome some of the limitations of current models. The influence of fiber orientation and distribution on material response was investigated from the elastic to the nonlinear phase. In the study of the elastic phase, expressions that correlate the phases' characteristics to the composite elastic properties were proposed. In addition, the effect of fibers on the dynamic properties of UHPFRC was evaluated by an impact acoustic test. In the nonlinear phase, a homogeneous model based on micromechanical phenomena and that considers the effect of fiber content and orientation, group effect, and direction dependence on the UHPFRC mechanical behavior was proposed. The group effect, which has been little studied, was analyzed updating finite elements models through Genetic Algorithms (GA) and experimentally investigated by a multi-fiber pullout test. Tension, compression, and bending tests validated the numerical model and analyzed the fiber orientation effect on the mechanical behavior of UHPFRC. According to numerical and experimental results, the orientation of the fibers influences the dynamic and elastic properties of the composite, which behaves anisotropically, and the nonlinear response of UHPFRC is strongly impacted by fiber arrangement. Therefore, a homogeneous numerical model has been developed for representing the anisotropy induced by fibers in the nonlinear response of UHPFRC. The present study has contributed to the research area with investigations on the UHPFRC mechanical behavior and development of a constitutive model that represents the particularities of the composite.

Keywords: UHPFRC; constitutive model; finite element method.

Resumo

RIBEIRO, P. O. **Contribuições para um modelo constitutivo para o concreto de altíssimo desempenho com fibras**. 2023. 159p. Thesis (Ph.D.) - São Carlos School of Engineering, University of São Paulo, São Carlos, 2023.

O Concreto de Altíssimo Desempenho com Fibras (em inglês Ultra-High Performance Fiber-Reinforced Concrete - UHPFRC) tem ganhado a atenção dos pesquisadores devido à alta resistência, ductilidade e durabilidade, permitindo projetos com elementos estruturais com seções mais delgadas e leves. Na literatura existem diversos trabalhos experimentais que permitem um melhor entendimento do comportamento mecânico deste material. Em relação aos modelos numéricos, ainda existem muitos fenômenos que devem ser considerados, como a influência da distribuição e orientação das fibras, o efeito de grupo e a dependência de direção. Nesse contexto, esta pesquisa visa superar algumas das limitações dos modelos atuais. A influência da orientação das fibras foi investigada desde a fase elástica até a fase não linear do material. No estudo da fase elástica, foram propostas expressões que correlacionam as características das fases com as propriedades elásticas do compósito. Além disso, o efeito das fibras nas propriedades dinâmicas do UHPFRC foi avaliado por meio do ensaio de impacto acústico. Na fase não linear, foi proposto um modelo homogêneo baseado em fenômenos micromecânicos capaz de considerar o efeito do conteúdo e orientação das fibras, efeito grupo e dependência de direção na resposta mecânica do UHPFRC. O efeito grupo, pouco estudado na literatura, foi investigado pela técnica de atualização de modelos em elementos finitos por meio de Algoritmos Genéticos (AG) e também experimentalmente por meio do ensaio de arrancamento de múltiplas fibras. Para validação do modelo numérico e investigação do efeito da orientação das fibras no comportamento mecânico do UHPFRC, foram realizados ensaios experimentais de tração, compressão e flexão de amostras concretadas por diferentes metodologias. Com base nos resultados numéricos e experimentais, conclui-se que a orientação das fibras influencia as propriedades dinâmicas e elásticas do compósito, que se comporta de maneira anisotrópica. Além disso, a resposta não linear do UHPFRC é fortemente impactada pelo arranjo das fibras. Sendo assim, um modelo numérico homogêneo foi desenvolvido para representar a anisotropia induzida pelas fibras na resposta não linear do UHPFRC. De maneira geral, o presente estudo contribui com a área de pesquisa ao investigar o comportamento mecânico do UHPFRC e apresentar contribuições para um modelo constitutivo capaz de representar as particularidades do compósito.

Palavras-chave: UHPFRC; modelo constitutivo; método dos elementos finitos.

Contents

ONE

INTRODUCTION

This first chapter is devoted to the problem statement, the objectives that motivated the research, the original results from the study, and the organization of the thesis.

1.1 Problem statement

Ultra-High Performance Fiber-Reinforced Concrete (UHPFRC) is a special class of cementitious composite materials that exhibits exceptional mechanical and durability properties. It is produced with Portland cement, reactive and inert admixtures, small size aggregates, superplasticizers, and steel fibers. The optimization of the mixture constituents provides a high packing density to the hardened composite, hence, ultra-high strength. Moreover, the concrete has high durability due to the dense microstructure, as illustrated in fig. 1 [1, 2, 3].

Figure 1 – Dense UHPC microstructure

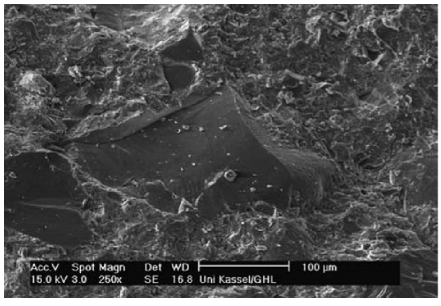

Source: Fehling et al. [1].

High-strength concrete generally undergoes a sudden failure after the first crack. The addition of fibers to UHPC delays the fast interconnection between early age microcracks and activates toughening mechanisms between fiber and matrix [2]. Despite such a positive effect, the mechanical behavior of the material depends heavily on the concrete production

process. In general, it is considered that the fibers are randomly oriented and homogeneously dispersed in the concrete; however, in practice, their orientation to a specific direction will probably occur, leading to anisotropic behavior of the concrete [4].

The development of the UHPFRC is accompanied by two fields of study: the experimental study and the development of constitutive models that allow the performance of numerical tests. Despite the accuracy of experimental analysis results, several researchers employ numerical analysis to identify phenomena not directly measured during an experiment, or analyze other situations not investigated experimentally. Compared to numerical models, experimental tests are more expensive and require more time and human resources to be performed [4].

Studies have shown a strong correlation between the fiber distribution characteristics and the mechanical properties of UHPFRC [5]. However, little numerical research has taken a systematic approach from microscopic to macroscopic view. Constitutive models usually adopted in UHPFRC simulations are developed for conventional concrete; they do not involve the phenomena between fiber and matrix and consider the material isotropic. More advanced models that include discrete fibers in the matrix demand a high computational cost.

This thesis reports on the development of numerical and experimental studies for the understanding of the mechanical behavior of UHPFRC and investigates the effect of steel fibers on its elastic, dynamic, and nonlinear response. A homogeneous numerical model that considers fiber content and orientation in the composite mechanical response has been developed and validated with experimental tests.

1.2 Research objectives

The general objective of this study is to contribute to a constitutive model for UHPFRC and the specific objectives involve:

- the understanding of the effect of fibers on the dynamic properties of the material;
- a study of the effect of fibers on the elastic properties of the composite;
- an evaluation of the isotropic or anisotropic behavior of the material;
- the understanding of the factors that govern the tensile response of the composite and how fibers provide ductility to the material;
- a review of UHPFRC modeling methodologies already developed; and
- an evaluation of the feasibility of developing a homogeneous model that captures the effects of fiber content and orientation on the nonlinear response of UHPFRC.

1.3 Original features

The research focuses on both development of a constitutive model for UHPFRC and investigation of the effect of fibers on the mechanical behavior of the composite. A consistent methodology for understanding the composite meso and micromechanical behavior helps solve the problem on a macroscale, contributing to the wide use of the material in real structures. This thesis will provide the following contributions to the corresponding research field:

- experimental and numerical analyses of the UHPFRC anisotropy and evaluation of the fiber effect on the dynamic properties of the composite through an impact acoustic test;
- a numerical analysis of the fiber effect on the UHPFRC elastic properties and proposition of expressions that correlate the fiber content and orientation with the elastic properties of the material;
- numerical and experimental evaluations of the group effect, which has been little explored in the literature;
- an experimental evaluation of the concrete casting procedure on the fiber orientation coefficient, hence, on the tensile and flexural response of the composite; and
- proposition of a UHPFRC modeling methodology that considers several factors, namely fiber content and orientation, group effect, fiber-matrix interface, spalling, and snubbing effect.

1.4 Organization of the thesis

This thesis is organized as follows:

- Chapter 2 reviews the literature on the modeling of the UHPFRC nonlinear behavior and discusses the main phenomena that occur in the composite, preparing theoretical concepts for a better understanding of the research.
- Chapter 3 is devoted to a study of the effect of fibers on the dynamic properties of UHPFRC through an experimental approach. An impact acoustic test was applied to cylindrical, dogbone, and prismatic samples cast according to different methodologies so that the influence of fiber content and orientation on the natural frequencies of the samples could be evaluated, revealing an orthotropic behavior of the material.

- Chapter 4 addresses a relationship among the elastic constants of UHPFRC and the fiber content and orientation. A numerical homogenization technique and models in finite elements generated a database with fiber content, orientation, and elastic constants. The relationship between among variables was then evaluated and regression models that predict elastic properties as a function of both characteristics and distribution of the phases are proposed.
- Chapter 5 provides a constitutive model based on micromechanics that models the nonlinear tensile behavior of UHPFRC and was validated with results from the literature and with the two-phase modeling previously developed by the research group.
- Chapter 6 describes an experimental investigation of the mechanical behavior of UHPFRC. The same samples subjected to the impact acoustic test (chapter 3) were used and compression, tension, and bending tests were performed. The results of an image analysis showed an evident influence of fiber orientation on both tensile and bending responses. Pullout tests performed aimed to understand the behavior of the fiber-matrix interface.
- Chapter 7 presents the Concrete Damaged Plasticity (CDP) model, implemented in Abaqus software, and its applications. It was implemented via UMAT subroutine towards modifications to the constitutive model and considers the effect of fibers on the mechanical response of UHPFRC. The traditional and modified CDP model was validated with experimental results and the constitutive model proposed in chapter 5 was used in all models developed.
- Finally, chapter 8 provides the main conclusions drawn.

Although the chapters complement each other and contribute to a constitutive model for UHPFRC, they also provide their contributions independently; therefore, the order of their reading can be chosen by the reader.

TWO

A REVIEW ON THE MODELING OF THE TENSILE BEHAVIOR OF UHPFRC

This chapter is devoted to a review on the influence of mechanical phenomena on the tensile behavior of UHPC, especially in the cracked phase, with a focus on straight steel fibers, and discusses the existing analytical and numerical approaches for the representation of such a behavior.

2.1 Introduction

Ultra-High Performance Fiber-Reinforced Concrete (UHPFRC) is a particular class of fiber reinforced cementitious composites that exhibits exceptional mechanical and durability properties. The optimization of the volume fractions of the mixture constituents provides a high packing density to the hardened composite, hence, ultra-high strength [1, 2, 6].

The tensile behavior of UHPFRC is complex. First cracking stress and location are typically controlled by a matrix defect. After that, several mechanisms between the fibers and the matrix such as interaction between fibers (group effect), fiber pullout (fiber-matrix interface), spalling, snubbing effect, fiber orientation, and distribution then determine the material behavior in the post-peak. Stress is transferred from the fiber to the matrix at cracks, and multiple cracks can occur. Material production and casting interfere with fiber distribution, thus governing the material mechanical behavior [6]. Such an influence has boosted research towards evaluations of the relationship between fiber distribution and orientation for a better use of material strength and understanding of the amount of strength that can be effectively employed in the design. Analyses of fiber distribution with techniques such as image analysis of cut sections provide fiber orientation properties associated with the casting process and material tensile behavior. In general and, according

to those studies, depending on fiber content and orientation, the material displays a strain-hardening or strain-softening behavior. A strain-hardening regime is characterized by multiple cracks and a stress redistribution that provides higher strength and ductility prior to the localization of a strain at one crack. The strain-hardening response can be divided into three parts. In part 1, the behavior is elastic, followed by the development of microcracking and fiber beginning of pullout, since they act mainly in the post-cracking phase by forming bridges between the crack faces. In part 2, a strain-hardening behavior with multiple cracks is displayed. Finally, in part 3, strain localization results in softening behavior [7] (see fig. 2). Part 2 does not occur in the strain-softening response.

Figure 2 – UHPFRC tensile behavior

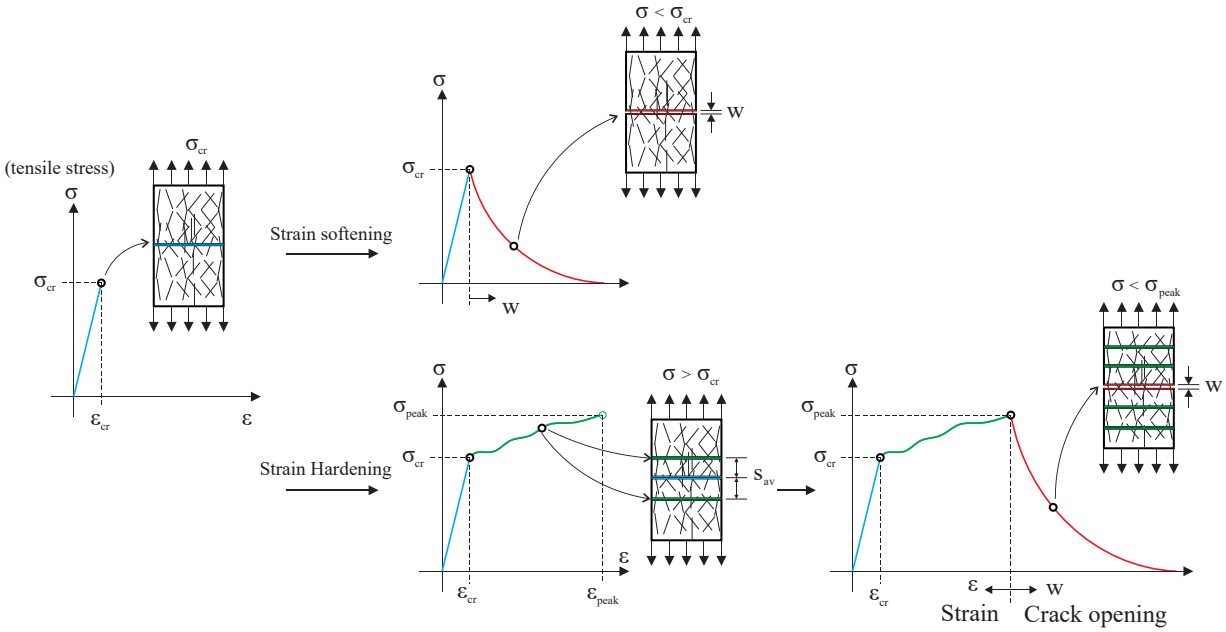

Source: the author.

The addition of fibers to UHPC delays the interconnection between microcracks and activates toughening mechanisms between fiber and matrix [2]. Therefore, fiber reinforcement is an efficient way to convert brittle concrete into a pseudo-ductile material [8]. On the other hand, despite such a positive effect, the UHPC mechanical behavior depends on the fiber distribution and orientation associated with the production process. Fiber orientation is strongly influenced by material rheology, casting procedure adopted, and formwork geometry. As an example, thin elements tend to orient the fibers to the flow direction due to wall effect preponderance. In contrast, when a panel is cast from its center, fibers have a tendency to line up with an orientation perpendicular to the radial flow [9]. In practice, the preferential fiber orientation along a specific direction will probably occur, leading to an anisotropic behavior of the concrete [4]. Such a trend must be understood towards better predictions of structural behavior. Moreover, models must consider fiber orientation and distribution and evaluate the influence of cast process and the shape of the structural elements different from laboratory samples [10].

Among the several modeling techniques that consider fiber orientation are multiphase modeling [11, 12, 13, 14], inverse analysis of experimental results [15], homogenization theory [16, 12], and analytical formulations based on micromechanical phenomena [10, 17, 18]. French standard [19] recommends designing UHPFRC structures considering fiber orientation and has introduced an orientation factor K, which expresses the effect of UHPFRC placement on the structure, determined by inverse analysis from a bending test in defining the composite tensile behavior. The concern over fiber orientation shows the importance of considering it in UHPFRC structures.

Despite the exceptional properties of UHPFRC and the current modeling techniques, the widespread use of the composite is limited. One of such limiting factors is the development of specific and validated analytical models for designing. Several researchers still use isotropic models implemented in non-specialized finite element commercial software to simulate the UHPFRC. Therefore, models that consider fiber-induced anisotropy and micromechanical phenomena for evaluating the performance of structural elements of UHPFRC must be designed [6].

This chapter reviews the main micromechanical phenomena and current modeling methodologies. Since UHPFRC is a particular class of FRC, many of the considerations are general.

2.2 Factors that influence the mechanical behavior of the material

This section presents factors/phenomena that influence the mechanical behavior of UHPFRC and discusses the following aspects: fiber behavior during pullout, fiber orientation and distribution, fiber content and group effect, fiber aspect ratio, and matrix strength.

2.2.1 Fiber Pullout

The mechanical properties of fiber-reinforced cement-based composites significantly depend on the stress transfer efficiency during fiber bridging. Fiber pullout test enable assessments of the fiber/matrix interface performance, which is of great importance in predicting the mechanical behavior of a composite. The fiber-matrix interface properties are affected by cement hydration (curing time and age), matrix density (packing), and surface treatment of the fiber, coating, or mechanical crimping [20, 21, 8]. The tests are usually performed with the fiber embedded in both sides of the sample, or in only one. They can also be conducted from single or multiple fibers, as illustrated in fig. 3. Tests with multiple fibers show an interaction between fibers, depending on their distance interfering with the load supported by them. Fu et al. [22] emphasized research on multiple fiber pullout is critical for understanding stress transfer in real composites.

Figure 3 – Fiber pullout test (a) single-sided specimen and single fiber; (b) double-sided specimen and single fiber; c) single-sided specimen and multiple fibers; (d) double-sided specimen and multiple fibers

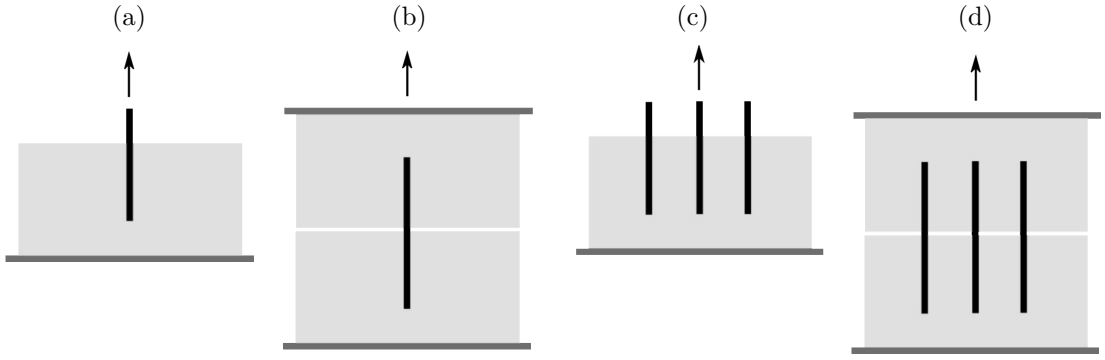

Source: the author.

Pullout tests provide parameters used in constitutive models for UHPFRC. Average bond strength τ is an important fiber-interface property and can be calculated by eq. (2.1) with the maximum load from pullout experiments (P_{max}), initial embedded length (l_e), and fiber diameter (d_f). τ is an input parameter for the obtaining of a pullout response with analytical models. An embedding length uniformly distributed in the 0 to $l_f/2$ domain is usually assumed; therefore, its average value is $l_f/4$ [23].

$$\tau = \frac{P_{max}}{\pi d_f l_e} \tag{2.1}$$

Pullout tests must be performed with straight and inclined fibers, since most fibers have inclinations with the crack surface in the composite. Krahl et al. [24] tested fibers with inclinations of 0º, 30º, and 45º inclinations to the loading direction. Snubbing and spalling effect mechanisms occur in inclined fibers due to increased frictional stresses at the end of the fiber tunnel. The snubbing effect positively influences the pullout load, whereas the spalling one is harmful, since it reduces the fiber contact area and stress transfer capacity. Considering the two simultaneous effects with opposite influences on the test response, [25, 26, 6] agreed on the existence of an optimal fiber orientation that improves the material ultimate carrying capacity and ductility in terms of energy absorption. The maximum pullout load of a steel fiber increases with the inclination until a certain angle around 30º [6]. For larger inclinations, spalling prevails and fibers can fail due to significant shear forces.

Function $g(\theta)$, defined by eq. (2.2), correlates inclined fiber pullout load $P(\theta)$ and straight fiber pullout load $P(\theta = 0)$. Li [18] adopted the function $g(\theta) = e^{f\theta}$ for nylon and polypropylene fibers, where θ is the inclination angle and f is the snubbing coefficient, considered an increase in bond strength. Regarding steel fibers, the fiber inclination causes matrix spalling for large angles, which must be considered. Zhou and Qiao [21] and Lee, Kang, and Kim [27] used $g(\theta) = e^{f\theta}cos\theta^k$ for UHPFRC with two coefficients to characterize the snubbing (coefficient f) and spalling effects (coefficient k) due to the inclination of the steel fiber in the matrix. Both coefficients are empirical.

$$P(\theta) = P(\theta = 0)g(\theta) \tag{2.2}$$

2.2.2 Fiber orientation

Fiber orientation in UHPFRC is influenced by flow patterns during the fresh state, the rheological performance of the mixture, casting methods, wall effect, mixture extrusion, and external electromagnetic field [28, 29, 9, 30]. The material mechanical performance can be significantly improved when the fibers are preferably aligned in the principal tensile stress direction [6, 31, 5]. Despite the significant improvement, fiber orientation during pouring can result in UHPC anisotropy.

Zhou and Uchida [32] studied the relationship between fiber orientation and post-cracking behavior of UHPFRC. A panel was molded from its center. When a panel is cast from its center, fibers have a tendency to line up with an orientation perpendicular to the radial flow [9]. Prismatic samples were cut with angles of 0º, 30º, 60º, and 90º angles between the sample axis and the panel radial direction (fig. 4) and the mechanical behavior of the samples was evaluated in three-point bending tests. Fiber orientation was obtained with image analysis and 3D visualization from X-ray computed tomography (CT). The post-cracking flexural strengths of specimens cut at angles of 60º, 30º, and 0º angles were, respectively, 80, 40, and 10% of that for specimens cut at an angle at 90º, indicating a linear dependence on the contribution of fibers close to the fracture surfaces (fig. 5).

Figure 4 – (a) Cutting locations of specimens in circular UHPFRC panel (b) Fiber orientation in the 1-m-square panel cast from its center with the use of a visualization model concrete

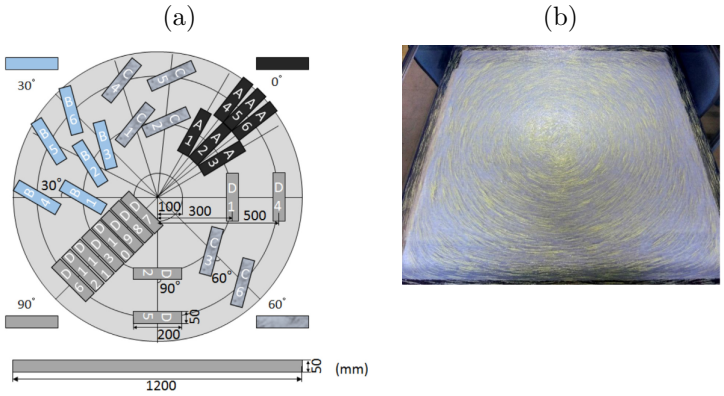

Source: Zhou and Uchida [32].

Figure 5 – Flexural stress

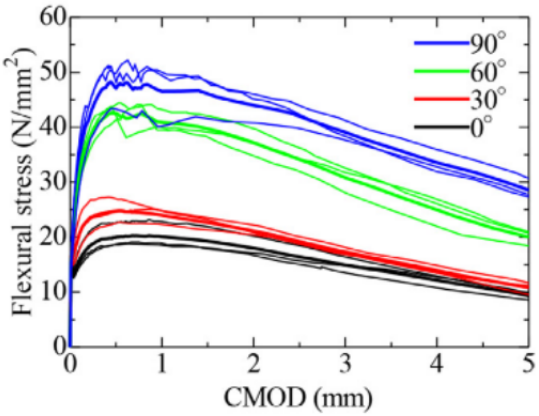

Source: Zhou and Uchida [32].

Fiber orientation can be evaluated by several tests such as image analysis, CT scan, translucent, viscous fluid, and electrical or magnetic methods [28]. Image analysis calculates fiber orientation based on high-resolution photographs. A fiber projected into the cutting plane is approximated by an ellipse so that the angle between the fiber axis and the normal cutting direction can be calculated by eq. (2.3):

$$\theta = \arccos(d_f/l), \tag{2.3}$$

where d_f and l are smallest and largest axis of the ellipse of the fiber in the cutting plane. Note for $d_f/l = 1$, the fiber is circular, hence, parallel to the direction normal to the cutting plane. Conversely, when d_f/l tends to zero, l is much larger than d_f, i.e., the fiber is perpendicular to the direction normal to the cutting plane.

An alternative definition is orientation coefficient η_θ [33, 6, 23, 10, 32], which can be determined as the mean of the cosine of the orientation angle of the fibers that cross

the cut section, according to eq. (2.4).

$$\eta_\theta = \frac{1}{n_f}\sum_{i=1}^{n_f}\cos(\theta)_i, \tag{2.4}$$

where n_f is the total number of fibers in a cutting plane and θ_i is the angle between the longitudinal axis of the fibers and the direction normal to the cutting plane. The equation indicates all fibers are aligned parallelly to the direction normal to the cutting plane when $\eta_\theta = 1$ and perpendicularly when $\eta_\theta = 0$.

Table 1 shows the orientation coefficient obtained from tensile samples and determined in relation to the loading direction of the sample. The results illustrate the influence of the casting method on the orientation coefficient, hence, on the mechanical behavior of the composite. Research indicates that η_θ is 0.5 for uniformly random 3D distribution of fibers [30]. Note most samples show a tendency to preferential alignment with one direction. A high orientation coefficient can be achieved by techniques such as electromagnetic field (see the results of Abrishambaf [10]).

Table 1 – Influence of the casting method on the orientation coefficient

Author	Comments	η_θ
Duque and Graybeal [6]	Extracted from slab perpendicular to flow direction	0.65
Duque and Graybeal [6]	Extracted from slab at 45º to flow direction	0.74
Duque and Graybeal [6]	Extracted from slab parallel to flow direction	0.83
Duque and Graybeal [6]	Mold cast specimens	0.85
Kang and Kim [5]	Concrete casting parallel to tensile stress direction	0.65
Kang and Kim [5]	Concrete casting transversal to tensile stress direction	0.43
Abrishambaf et al. [10]	Well-oriented fibers - V_f =1.5%	0.89
Abrishambaf et al. [10]	Not-oriented fibers - V_f =1.5%	0.71
Abrishambaf et al. [10]	Well-oriented fibers - V_f =3%	0.87
Abrishambaf et al. [10]	Not-oriented fibers - V_f =3%	0.74

Source: the author.

2.2.3 Fiber content/Group effect

Zhou and Qiao [21] showed an increase in volumetric fiber fraction improves the composite tensile strength; however, the improvement rate is not linear and can decrease when high fiber contents are used. The authors proposed a model for the prediction of the UHPFRC tensile behavior based on the analytical pullout model of Lee, Kang, and Kim [27] and the results were validated in direct tensile tests. An underestimated response was obtained for low fiber volume, i.e., the efficiency of fiber reinforcement decreases with increasing fiber volume fraction due to the group effect, which affects the fiber pullout strength because stress overlap occurs in the concrete between the fibers, reducing their efficiency. Most analytical and numerical models do not consider the group effect, although it significantly influences the material response.

Li, Wang, and Backer [8] observed fiber bundling in synthetic fibers reinforced concrete. The formation of fiber bundles reduces its contact area interacting with the matrix and can introduce zones of weakness into the composite due to lower resistance in those regions. Kim and Yoo [34] investigated the group effect on the steel fibers experimentally examining the influence of the distance between fibers on the pullout behavior of fibers immersed in UHPC. Three types of fibers, namely straight, hooked, and twisted and four distances between fibers were investigated towards representing composites with volumetric fractions of 1%, 2%, and 7% of fibers and the case of fiber bundle (clustering). The twisted steel fiber showed the highest pullout strength in the single fiber test, followed by hooked and straight steel fibers. The average bond strength of the multiple fiber specimens decreased 22%–30% compared to the single fiber specimen. The bundled fiber specimens showed a 52% decrease. The correlation between the pullout behavior of single aligned fibers in the matrix and the flexural behavior is relatively low due to several influential parameters. So, the prediction of the composite behavior through only single fiber pullout test results is difficult.

Huo et al. [35] proposed a constitutive model for FRC, considering the interaction between neighbor fibers and suggested the group effect becomes significant when the spacing between fibers s is smaller than an influence diameter d_{eff}. By analogy with the pile group effect under negative friction resistance, $d_{eff} = 6d_f$ (fig. 6) was adopted, according to which the critical fiber volumetric fraction is 4.58%. After that limit, the group effect must be considered - the smaller the s spacing, the more significant the group effect. Note the experimental results of Kim and Yoo [34] indicate the group effect occurs for UHPFRC with 1% of fiber content. Therefore, further investigations on that topic should be carried out. No experimental investigations on the influence of matrix reinforcement on group effect have been reported.

Figure 6 – Schematic diagram of fiber spacing

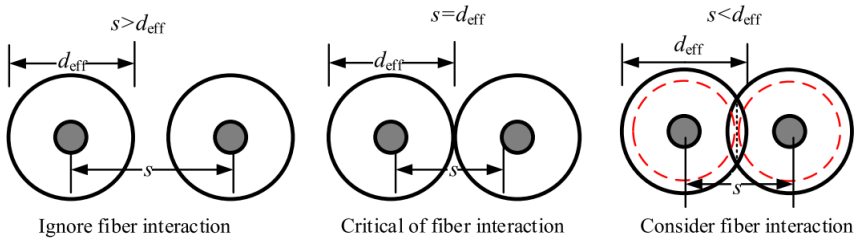

Source: Huo et al. [35].

2.2.4 Fiber embedded length

Fibers initially adhere to the matrix and then develop friction during composite straining. The load carried by both mechanisms naturally depends on the embedment length, since the fiber load is transferred to the matrix by shear. Abrishambaf, Pimentel, and Nunes [10] proposed a constitutive model for predicting the tensile behavior of UHPFRC. They performed a pullout test with a single fiber immersed in the UHPC matrix with 3 and 6mm embedded lengths and 0º, 30º, and 60º inclinations. The maximum pullout force was reported occurred with 6 mm embedded length and 30º inclination (see fig. 7).

Figure 7 – Influence of fiber orientation and embedded length on pullout force

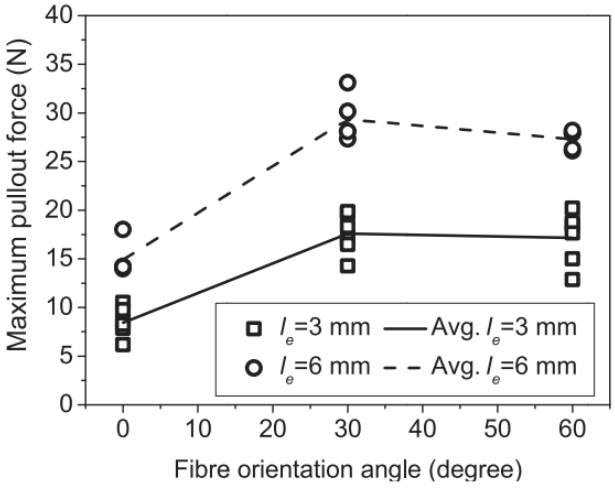

Source: Abrishambaf, Pimentel and Nunes [10].

2.2.5 Fiber length and diameter

Zhou and Qiao [21] investigated four fiber aspect ratios for UHPC reinforced with straight steel fibers through analytical models and lf/df of 6/0.16, 13/0.2, 19/0.3, 25/0.38 mm/mm corresponding to 37.5, 65.0, 63.3, and 65 aspect ratios. The results showed the higher the aspect ratio, the greater the material's tensile strength. According to the authors, the larger fiber aspect results in fewer fibers crossing the crack plane, hence,

lower interference between them. On the other hand, a short fiber results in a higher fiber density in the crack plane and a higher group effect. Fibers of 13/0.2, 19/0.3, and 25/0.38 mm/mm provided close tensile strengths. However, UHPC with longer fibers showed higher energy absorption. According to the authors, longer fibers have higher bridging forces and stronger partial debonding action and straining hardening process.

2.2.6 Matrix strength

The increase in matrix strength tends to refine and enhance the interface between fiber and matrix. As an example, silica fume, whose average dimension is typically smaller than that of cement, densifies the interfacial transition zone between the two phases, increasing pullout load and the energy dissipated and favoring the development of strain hardening composites. In this sense, Chan and Chu [36] investigated the effect of incorporating silica fume in the reactive powder concrete and observed silica fume can improve fiber-matrix interfacial properties. Figure 8 shows the pullout response for different silica fume contents. The optimal silica fume was around 20%, since the improvement after 20% was negligible.

Figure 8 – Fiber pullout curves for different silica fume contents

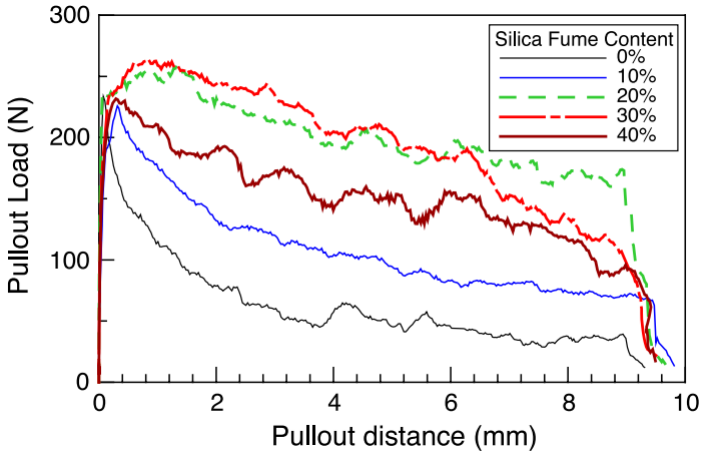

Source: Chan and Chu [36].

2.2.7 Fiber distribution effect

The distribution of fibers dispersed in the matrix is rarely totaly uniform and their orientation is not ideally random. As an example, if the fiber length ratio to a structural element thickness is large, the fibers tend to assume a 2D distribution. Due to vibration, a preferred 2D distribution can also be observed in thick components, resulting in an anisotropic behavior. The uniformity of fiber distribution is hihgly influenced by the mixing and consolidation process and the analytical treatment of fiber distribution can be based on stereological models [37].

Shen and Brühwiler [38] introduced a uniformity factor μ_2 for considering local fiber distribution in UHPFRC elements. The factor is a scalar indicator of the uniformity degree in the local fiber distribution. $\mu_2 = 1$ when all fibers are oriented and equally spaced, corresponding to a homogeneous material in the loading direction, whereas $\mu_2 < 1.0$ corresponds to an anisotropic behavior (fig. 9). The authors investigated the influence of μ_2 on the tensile response through an experimental campaign and concluded fiber distribution is an important factor in tensile behavior. The strain-hardening response is directly dependent on the local fiber distribution. Some regions with a poor fiber distribution become critical for an entire sample, since the remaining parts cannot develop the hardening capacity.

Figure 9 – Uniformity factor: (a) $\mu_2 = 1.0$ (b) $\mu_2 < 1.0$

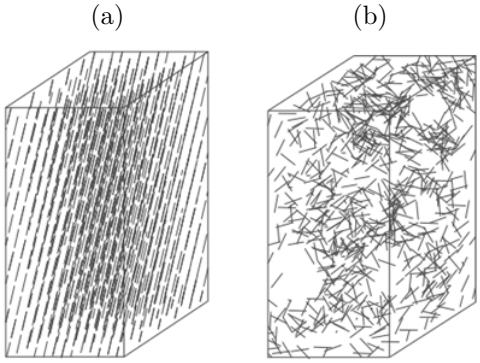

Source: Shen and Brühwiller [38].

2.2.8 Fiber hybridization

The typical fibers used in UHPFRC are high-strength straight steel ones usually coated for enhancing friction and protecting against corrosion. However, hybrid solutions have been investigated towards improvements in composite performance due to synergistic effects [39, 40]. Mainly different fibers (in diameter and length) can reinforce cracking on different scales. As an example, the combination of different sizes of steel fibers [41, 42] and different types of fibers can reinforce different crack sizes and enhance strength and toughness. Yu, Chen, and Leung [43] studied the crack-bridging relations of strain-hardening cementitious composites (SHCC) with fixed total volume fraction (2.5%) of hybrid polyvinyl alcohol (PVA) and steel fibers. According to eq. (2.5), the numerical model considered the superposition of the contribution of the different components (matrix - σ_m, steel - σ_{steel}, and PVA - σ_{PVA}). The authors concluded the hybridization of PVA/steel fibers results in a positive synergetic effect at a single-crack level under uniaxial tension.

$$\sigma = \sigma_m + \sigma_{PVA} + \sigma_{steel} \tag{2.5}$$

Fiber hybridization can also improve the composite performance under high-temperature conditions. Mindeguia et al. [44] investigated such a behavior using a device to measure temperature, pore vapor pressure, and mass loss of concrete specimens. Five concrete mixtures with a constant aggregate volume, but different water/cement ratios were tested. The study aimed at a better understanding of the thermo-hydraulic behavior of concrete exposed to high temperatures and its correlation with possible spalling. Spalling has two main mechanisms, namely a thermomechanical process, which involves high-temperature variables and induces high compressive stresses in the concrete, and a thermo-hygral one associated with the movement of fluids present in the concrete due to pressure gradients and molar concentration. Water vapor begins to condense and cause pressure on the pores, possibly exceeding the tensile strength and initiating fragmentation [44]. The results showed (1) the low concrete compaction (high w/c ratio) induces greater permeability to fluids and facilitates water escape; (2) low permeability involves high pore pressure accumulation, therefore, the lower the w/c rate, the higher the pore pressure; and (3) the denser the concrete, the higher the vaporization temperature. Those findings explain why UHPC, which is a concrete with a low w/c ratio, is more susceptible to spalling than conventional concrete. In this sense, [45, 46, 47, 48] indicated polypropylene fibers for preventing explosive spalling. Li and Zhang [45] evaluated the behavior of UHPC without fibers, with only polypropylene (PP) fibers, and with steel and PP fibers and observed the addition of PP fibers did not change the material mechanical properties. In contrast, the addition of steel fibers increased compressive and tensile strength and elasticity modulus. Tests have shown a simultaneous inclusion of PP and steel fibers can fully prevent explosive spalling. Li, Tan, and Yang [46] also showed the use of hybrid PP and steel fibers even low dosages in UHPC prevented explosive spalling due to a significant permeability increase. The synergistic effect on increased permeability was attributed to enhanced connectivity of empty PP fiber tunnels by multiple microcracks generated from the thermal expansion of both fibers.

2.3 Modeling methodologies

This section presents some methodologies used in the UHPFRC modeling, including analytical models based on micromechanical phenomena, multiple cracking modeling, multiphase modeling, inverse analysis, and models based on homogenization theory.

2.3.1 Analytical models based on micromechanical phenomena

Analytical models based on micromechanical phenomena have been developed and implemented towards simulating fiber-reinforced concrete [10, 17, 18]. They take parameters from a microscopic view and study the phases (fiber, matrix, and fiber-matrix interface properties) on a macroscopic scale, as illustrated in fig. 10. Li [49] highlighted micromechanical models consider microscale phenomena (e.g., interfacial slippage with chemical or adhesive debonding and microcrack opening) and aspects on higher scales, such as fiber length. Other features (e.g., composite composition, fiber surface treatment, and porosity) are indirectly considered by matrix properties and interfacial parameters. In such methodologies, fiber distribution and orientation are considered statistically. Fibers are not explicitly considered, so it presents advantages relative to computational cost compared to multiphase models being more prominent solutions for structural analysis.

Figure 10 – Scaling up modeling of FRC

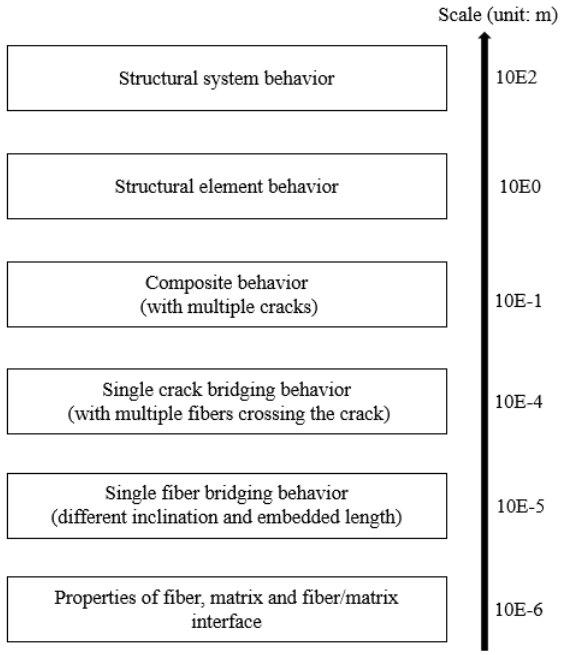

Source: Yao and Leung [50].

2.3.2 Modeling multiple cracking

A fundamental behavior of strain hardening composites is developing multiple cracks under tensile stresses while increasing the load. Such an increase occurs because the bridging fibers can carry more stress than the matrix, as shown in fig. 11. Therefore, the tensile strength of the composite is reached when the crack bridging reaches its maximum value. The fibers load transfer mechanism promotes successive neighbor cracks during the process and both crack spacing (s) and width (w) govern the strain at peak load. The micromechanics-based design considers the aforementioned processes and can be a powerful tool for tuning component performance, selecting ingredients for mixing optimization, and developing new strain hardening materials.

Figure 11 – Development of crack bridging and multiple cracking developments

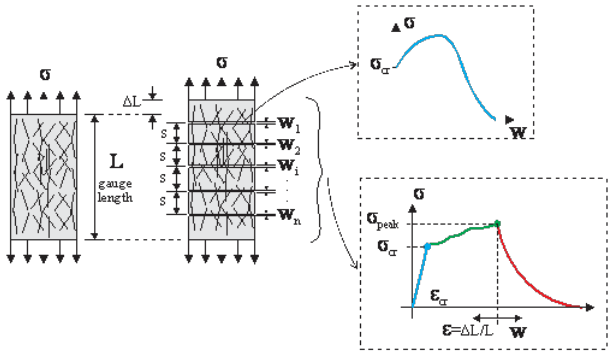

Source: the author.

The composite deformation can be calculated assuming a crack spacing model and the stress-crack opening curve (σ-w). Total deformation ε is then obtained by eq. (2.6):

$$\varepsilon = \varepsilon^{el} + \varepsilon^{cr} = \frac{\sigma}{E} + \frac{\sum w_i}{L}, \tag{2.6}$$

where, $\sum w_i$ is the sum of all crack openings developed until the applied stress, as depicted in fig. 11.

Micromechanical models are of general use for the development and prediction of the behavior of any class of fiber-reinforced cement-based composites, despite being applied mainly to ECC. However, some variables such as snubbing effect coefficient, parameters for statistical distributions of matrix strength, and fiber distribution require adaptation and some mechanisms evidenced in experimental tests are not included in models (e.g., fiber group effect, real distribution and size of flaws to determine crack strength, and fiber orientation and distribution). Fiber orientation is typically adopted with 3D and 2D patterns.

2.3.3 Multiphase modeling

Recent research has investigated methodologies for FRC modeling and several studies have developed models that include discrete fibers immersed in concrete. Bitencourt Jr et al. [11] simulated a composite with a discrete and explicit representation of steel fibers. The material was comprised of concrete, discrete fibers, and a fiber-matrix interface. The steel fibers were modeled with the use of truss elements with an elastoplastic constitutive model in one direction. A non-rigid coupling procedure was proposed for modeling the complex nonlinear behavior of the fiber-matrix interface - an appropriate constitutive damage model adopted described the relationship between shear stress and relative sliding between the matrix and each fiber individually. Qsymah [12] simulated the composite with two phases, namely matrix and fibers. The model was based on an in-situ micro X-ray computed tomography (μXCT) wedge splitting test. The behavior of the fiber-matrix interface was considered indirectly through the constitutive law of fibers based on the pullout of the fibers, as proposed by Cunha, Barros and Sena-Cruz [13, 51] and Soetens et al. [14]. Discrete fiber simulation is a natural way to simulate a composite and capture fiber distribution and orientation. However, the methodology is limited by computational cost.

2.3.4 Inverse analysis

In several studies, the stress-strain relationship is obtained by inverse analysis of experimental results [52, 53, 15]. Kang et al. [15] studied the tensile fracture properties of UHPFRC for fiber content ranging from 0% to 5%. The composite tensile response was obtained from bending tests with inverse analysis and the authors suggested a trilinear softening curve to represent the tensile behavior of the material. Baby et al. [53] proposed an inverse analysis method to determine the tensile behavior of UHPFRC from four-point flexural tests. According to the methodology, the tensile stress-strain curve profile is not previously assumed and is obtained from the bending moment versus midspan deflection experimental response. Stephen et al. [52] employed an optimization algorithm to determine the crack stress-opening curve for FRC with polymer and steel fibers. The curve parameters were calibrated by inverse analysis of experimental results and the model was further validated through the prediction of the flexural response of unnotched and notched beams and a comparison of the results with experimental test data. A possible limitation of the methodology is the calibrated curve works specifically for the material tested and the conditions of the calibrated samples; therefore, it should be validated with other experiments from the literature.

One of the techniques that solves inverse analysis problems is automated finite element model updated by Genetic Algorithms (GA). A simple GA comprises three

operators, namely selection, crossover, and mutation. Initially, a population of individuals containing random values for the material properties is generated. The finite element model is then processed and the individuals are evaluated by an objective function. According to the adequacy to the experimental results, each individual receives a score. Next, individuals are selected in function of their fit, i.e., those with better scores are more likely to be chosen. Subsequently, crossover and mutation operators are applied. Finally, the model is processed again with the new individuals. Such a loop is repeated until the stopping criterion has been reached. Figure 12 shows the flowchart of the calibration procedure. The technique was adopted in the present study.

Figure 12 – Calibration model by Genetic Algorithms

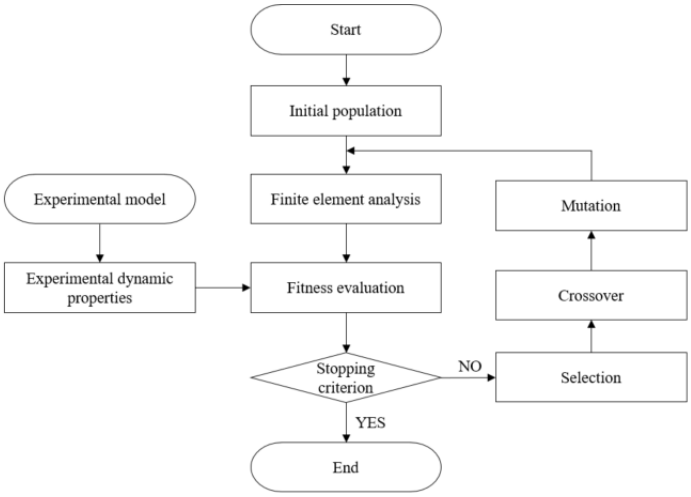

Source: the author.

2.3.5 Models based on homogenization theory

Models based on homogenization theory have also been developed. Yu et al. [54] designed multi-scale models for UHPFRC with different coarse aggregate contents and fiber volume fractions. The constitutive model of the material at the mesoscale was established using the Mori-Tanaka homogenization method and a progressive damage theory. According to the multi-scale modeling method, a local homogenization of macroscopic solids usually solves mechanical problems on a mesoscale. Both macroscale and mesoscale are connected by a representative volume element (RVE) that must be large enough to represent the potential inhomogeneous microstructure and small enough for a macroscopic structure. Numerical tests simulated by the authors showed compressive, tensile, and four-point bending strengths increase and then decrease with fiber content. On the other hand, the improving effect of coarse aggregate on UHPFRC properties was not so noticeable. Dutra, Maghous, and Campos Filho [16] investigated the strength properties of the fiber-reinforced concrete employing a micromechanics approach that combined the static approach of limit

analysis with the homogenization theory. The authors proposed a macroscopic strength criterion for fiber-reinforced concrete.

2.4 Final Remarks

This chapter provided an overview of factors that influence the mechanical behavior of fiber reinforced concrete, such as fiber pullout, fiber orientation and distribution, fiber content, fiber aspect ratio, and matrix strength. The computational simulation of a composite is a complex task and, although several methodologies have been developed, but there is still much to be explored in the experimental and numerical field.

THREE

EVALUATION OF THE FIBER EFFECT ON THE DYNAMIC PROPERTIES OF UHPFRC

This chapter addresses an investigation on the effect of fiber content and orientation on the dynamic properties of UHPFRC towards an evaluation of the anisotropic behavior of the composite in the elastic phase. Different concrete casting methods were used for the obtaining of different fiber distributions. Cylindrical, prismatic, and dogbone samples of UHPC and UHPFRC were produced. The natural frequencies of the samples were provided by an impact acoustic test. Moreover, a numerical model was developed in commercial software Abaqus® initially to assist the identification of vibration modes. It was then calibrated according to the experimental natural frequencies and the elastic constants of the material were determined.

3.1 Experimental program

The experimental program was developed in the São Carlos School of Engineering laboratories. This section presents the properties of the materials, the samples produced, the tests performed, and the numerical model that supported the experimental data analysis.

3.1.1 Materials properties

The following materials were used: Portland cement with high initial strength (CPV-ARI) (3.16 g/cm^3 specific mass), fine industrial sand (2.64g/cm^3 specific mass, 0.42 mm maximum diameter), quartz powder (2.72 g/cm^3 specific mass), silica fume (2.22 g/cm^3 specific mass), superplasticizer based on polycarboxylate (1.06 g/cm^3 specific mass), and water. In addition to straight and short steel fibers, $l_f = 13$ mm and $d_f = 0.2$ mm,

see fig. 13. Table 2 shows the UHPC composition. UHPC and UHPFRC with 1% and 2% fber content, respectively, were studied.

Figure 13 – Steel Fiber

Source: the author.

Table 2 – Materials (kg/m^3 of concrete)

Cement	Sand	Quartz powder	Silica fume	Water	Superplasticizer
757.2	833.0	378.6	189.3	156.0	68.2

Source: the author.

A mechanical mixer of 18-liter capacity, 60 Hz frequency, and 172 to 533 rpm speed was used. First, sand, 20% of water, and 25% of superplasticizer were mixed for 1 minute at low speed. Cement, quartz powder, silica fume, 20% of water, and 25% of superplasticizer were introduced and mixed for 4 minutes at medium speed. 40% of water and 50% of superplasticizer were then added and mixed for 5 minutes at maximum speed. The remaining water was added and mixed for 3 minutes at maximum speed. Regarding UHPFRC, fibers were added and mixed for another 3 minutes for homogenizing the mixture. Finally, the samples were demolded after 24 hours and submerged in water for thermal curing at 85^{o}C until the seventh day, as shown in fig. 14.

Figure 14 – Heat-curing samples

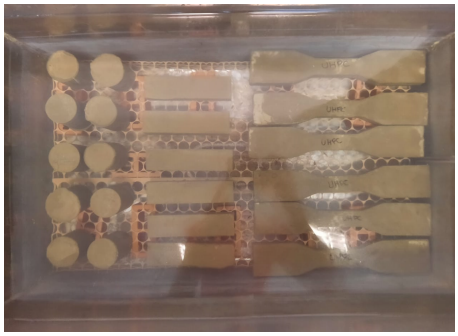

Source: the author.

3.1.2 Test specimens

Prisms were produced by three different methods. According to method 1 (M1), the concrete was cast longitudinally in a horizontal formwork, whereas in method 2 (M2), it was cast transversally. Finally, in method 3 (M3), the concrete was cast vertically in a vertical formwork. Method 1 aimed to align the fibers in the longitudinal direction of the formwork. A baker's bag with a 30 mm opening was used for the alignment. Figure 16 displays the procedure adopted. In samples M2 and M3, the concrete was poured in the usual way, with a change only in the direction of the formwork.

Figure 15 – Concrete casting method (a) M1 (b) M2 (c) M3 (prisms)

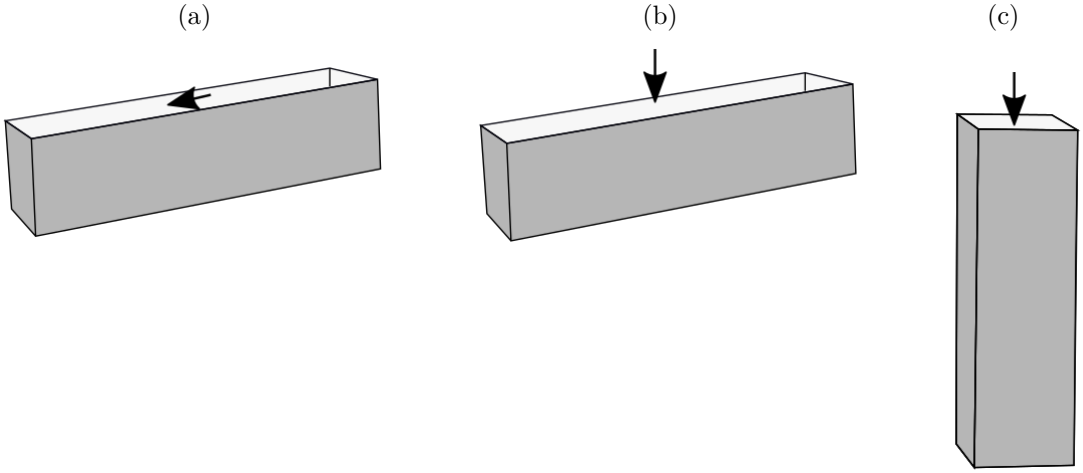

Source: the author.

Figure 16 – Method 1 (M1)

Source: the author.

The dogbone samples were produced by two methods. The concrete was cast in longitudinal (method 1- M1) and transverse (method 2 - M2) directions of the formwork, similarly to the procedure for the preparation of the prismatic specimens (see Figure 17). The cylindrical samples were produced according to the conventional methodology.

Figure 17 – Concrete casting method (a) M1 (b) M2 (dogbone)

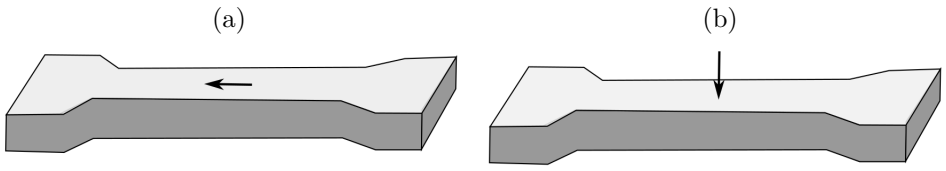

Source: the author.

Table 3 shows the number of samples which were named according to their geometry, fiber content, and casting method. P1%M1, for example, is a prismatic 40 x 40 x 160 mm^3 (P) sample with 1% of fiber content and the casting method 1 (M1). Letter C denotes the cylindrical sample 50 (diameter) x 100 mm^2 and D refers to the dogbone, with a 30 x 30 mm^2 center section.

Table 3 – Number of samples

Sample	Type	V_f (%)	Casting method	Amount
C0%	Cylindrical	0	Conventional	8
C1%	Cylindrical	1	Conventional	8
C2%	Cylindrical	2	Conventional	10
P0%	Prismatic	0	M2	6
P1%M1	Prismatic	1	M1	6
P1%M2	Prismatic	1	M2	6
P1%M3	Prismatic	1	M3	5
P2%M1	Prismatic	2	M1	6
P2%M2	Prismatic	2	M2	6
P2%M3	Prismatic	2	M3	5
D0%	Dogbone	0	M2	6
D1%M1	Dogbone	1	M1	4
D1%M2	Dogbone	1	M2	5
D2%M1	Dogbone	2	M1	5
D2%M2	Dogbone	2	M2	5

Source: the author.

3.1.3 Impact acoustic tests

The natural frequencies were obtained by the impact acoustic test. The lower scattering of the impact acoustics technique and the advantages of nondestructive tests (several repetitions of the test with the same sample, low cost, and fast execution) were determinant factors for the use of the technique in the investigation of UHPFRC anisotropy

[55]. As shown in fig. 18, the specimens were supported by steel wires connected to a rigid frame to simulate free-free boundary conditions. A specially designed hammer with a rubber handle and steel sphere head of 12.7 mm diameter applied the manual impact and a regular microphone captured the sound irradiated by the surface of the specimen. The microphone was connected to a standard sound card in the computer. Sonelastic® (ATCP) software enabled a precise extraction of the peaks associated with natural frequencies after the application of Fast Fourier transform (FFT). The position of impact and microphone varied according to the vibrational modes.

Figure 18 – Impact acoustic test configuration

Source: the author.

3.1.4 Numerical simulation

A numerical eigenfrequency analysis was performed with the finite-element method (FEM) for assisting and improving the data analysis of impact acoustic tests. The numerical model was developed by Abaqus® software. No constraints were applied for the eigenfrequency analysis, since this was a representative condition for acoustic experiments (free-free boundary condition). Coordinate system's X-, Y-, and Z-axes coincided with material directions 1, 2, and 3 (fig. 19) and the number of elements was based on the mesh convergence test. An 8-node linear brick (C3D8) element was employed. The vibration modes evaluated are shown in the figures below. Letter F refers to flexural vibration mode, L denotes longitudinal vibration mode, and T refers to torsional vibration mode.

Figure 19 – Finite element model (a) 34643 elements C3D8 (b) 33600 element (c) 41808 elements

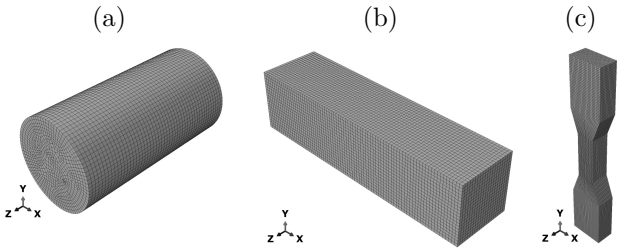

Source: the author.

Figure 20 – Vibration modes of cylinder specimens obtained by the numerical model

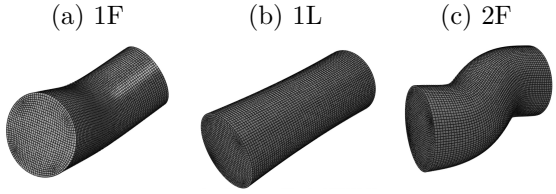

Source: the author.

Figure 21 – Vibration modes of prism specimens obtained by the numerical model

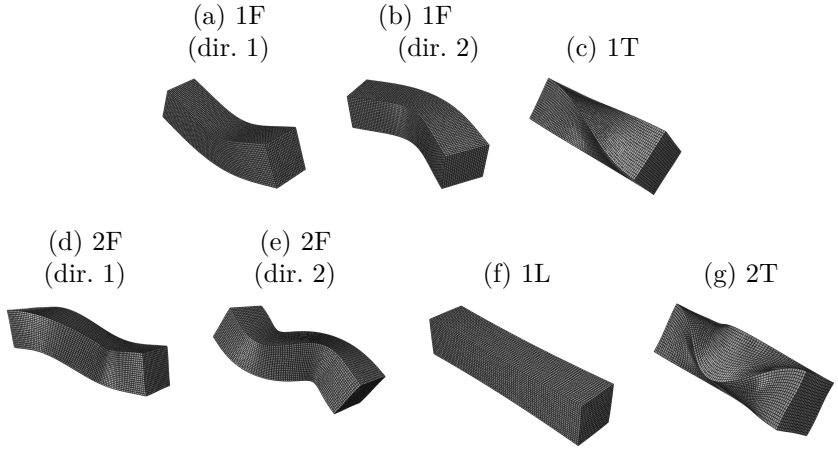

Source: the author.

Figure 22 – Vibration modes of dogbone specimens obtained by the numerical model

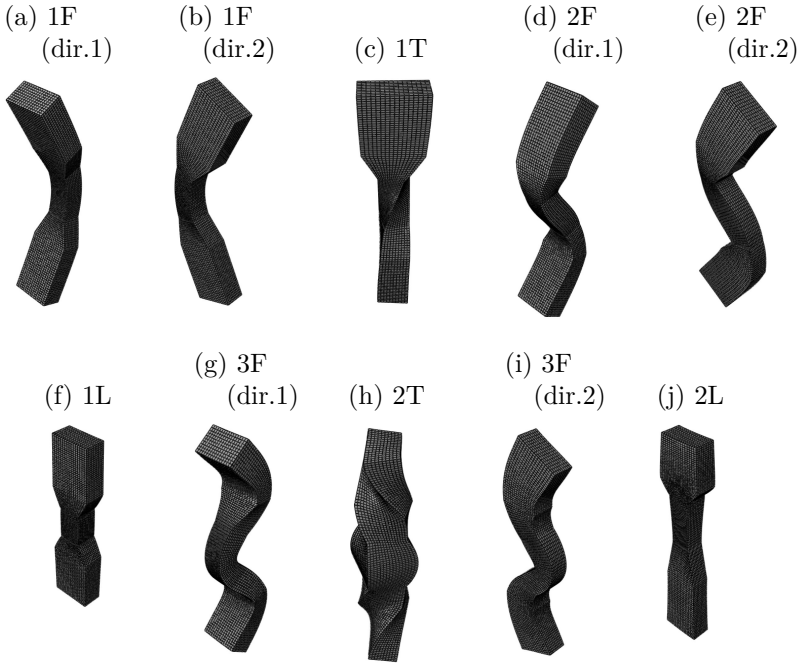

Source: the author.

After the obtaining of the experimental natural frequencies, the numerical model was calibrated by Genetic Algorithms (GA) implemented in Python and coupled to the finite element model. Each generation consisted of 50 individuals; the crossover rate was 0.90 and the mutation rate was 0.10. The elitism technique was adopted and preserved the three best individuals in the population. The inverse analysis problem was defined by eq. (3.1), where $\omega_{i,num}$ is the numerical frequency corresponding to mode i and $\omega_{i,exp}$ is the experimental frequency corresponding to mode i. The objective was to minimize the difference between experimental and numerical responses. The elastic constants of the material were calibrated according to the isotropic or orthotropic material. The isotropic material has two variables, namely modulus of elasticity and Poisson's ratio, whereas the orthotropic one comprises the following nine independent variables: longitudinal modulus of elasticity in the three directions, transverse modulus of elasticity in the three directions, and Poisson's ratio in the three directions.

$$g = \max_{i=1,\ldots,n} \left| \frac{\omega_{i,num} - \omega_{i,exp}}{\omega_{i,num}} \right| 100\% \tag{3.1}$$

3.1.5 Image analysis

Prismatic and dogbone samples were cut and submitted to an image analysis in ImageJ software [56]. Fiber orientation was quantified by the orientation coefficient, given by eq. (2.3). The image analysis, conducted after the tensile and bending tests presented in

chapter 6, evaluated the influence of the casting method on the fiber orientation, hence, on the dynamic properties of the material. The samples were cut in sections 1 cm away from the cracked section towards ensuring the integrity of the analyzed faces. The analysis was performed on a section to the right and a section to the left of the crack. The orientation coefficient considered was the average value of the two sections.

3.2 Results

This section presents and discusses the results, including the orientation coefficients obtained by image analysis, the natural frequencies provided by the acoustic impact test, and the calibration of the numerical model.

3.2.1 Image analysis

Figure 23 shows the steps of the image analysis performed in ImageJ software. First, the faces of the cuts were photographed and the photos were converted into a binary image, where the fibers were highlighted in white. The particle analysis was then performed. Next, fibers were approximated by ellipses and the program provided their major and minor axes. Finally, eq. (2.4) calculated the orientation coefficient. Note the fibers were homogeneously distributed in the cementitious matrix, showing the quality of the methodology of mixing and placing the concrete.

Figure 23 – Image analysis steps (dogbone with 1% fibers – casting method 1)

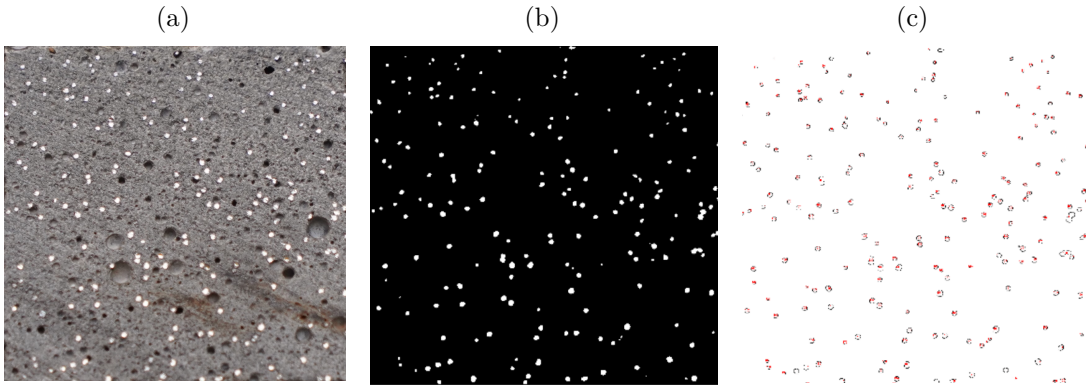

Source: the author.

Table 4 shows the orientation coefficients obtained. As expected, they were higher when the concrete was cast in the longitudinal direction of the formwork (M1). The smallest dispersions in the results are visualized due to a better control of the concrete casting process. On the other hand, the prisms produced with the vertical formworks (M3) showed the lowest orientation coefficients, since the fibers tended to align in the transverse direction of the sample.

Table 4 – Orientation coefficient

Sample	η_θ	Coefficient of variation
P1%M1	0.797	1.81%
P1%M2	0.746	3.64%
P1%M3	0.680	4.90%
P2%M1	0.810	2.13%
P2%M2	0.753	2.35%
P2%M3	0.699	3.66%
D1%M1	0.793	1.04%
D1%M2	0.730	6.56%
D2%M1	0.787	1.39%
D2%M2	0.739	4.65%

Source: the author.

3.2.2 Impact Acoustic Tests

Figure 24 displays the typical sound spectrum obtained with flexural excitation. The natural frequencies were acquired by plotting the amplitude versus frequency. The figure clearly shows the three peaks, which refer to the first, second, and third flexural modes.

Figure 24 – Results of the impact acoustic test (a) typical sound spectrum obtained with flexural excitation (b) natural frequencies

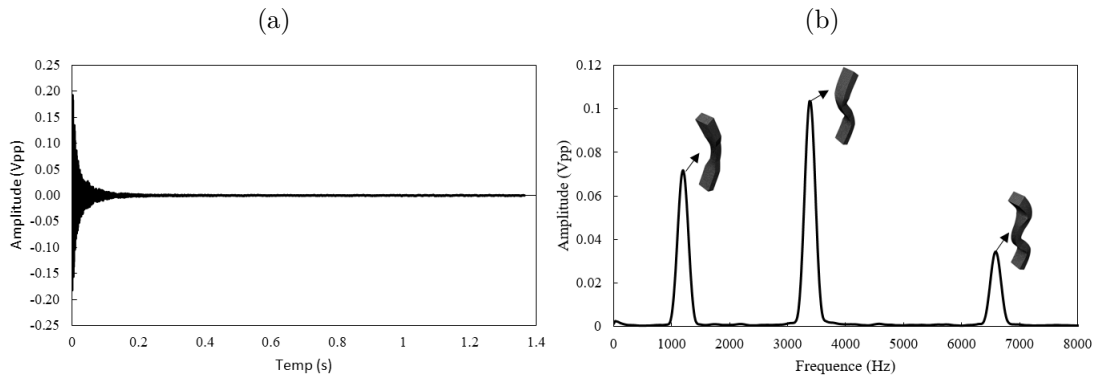

Source: the author.

The tables show a summary of the natural frequencies and densities obtained experimentally.

Table 5 – Experimental natural frequencies of cylinder specimens (Hz)

Sample	ρ (Kg/m^3)	1F	1L	2F
C0%	2211.88 (0.75%)	14463.66 (1.24%)	22919.99 (0.87%)	25079.46 (0.79%)
C1%	2288.82 (0.26%)	14386.27 (1.88%)	22833.18 (1.54%)	25166.38 (1.39%)
C2%	2389.45 (1.02%)	14442.76 (1.49%)	23008.77 (1.15%)	24955.19 (1.18%)

Source: the author.

Table 6 – Experimental natural frequencies of prism specimens (Hz)

Sample	ρ (kg/m^3)	1F (dir.1)	1F (dir. 2)	1T	2F (dir. 1)	2F (dir. 2)	1L	2T
P0%	2216.47	6295.47	6181.66	8511.25	14046.91	13882.735	14243.33	17050.59
	(0.48%)	(1.96%)	(0.84%)	(0.36%)	(1.29%)	(0.74%)	(0.49%)	(0.55%)
P1%M3	2249.06	5893.27	5824.48	8208.08	13405.75	13310.48	13668.53	16423.97
	(0.48%)	(2.75%)	(2.12%)	(1.55%)	(0.42%)	(0.26%)	(0.28%)	(1.60%)
P1%M2	2261.28	6140.29	6119.77	8422.26	13730.15	13790.80	14098.83	16831.43
	(0.58%)	(2.01%)	(0.62%)	(0.55%)	(1.45%)	(0.56%)	(0.50%)	(0.72%)
P1%M1	2240.90	6232.59	6163.44	8436.40	13891.21	13821.66	14217.29	16848.67
	(1.55%)	(2.20%)	(0.82%)	(0.54%)	(1.54%)	(0.60%)	(0.62%)	(0.59%)
P2%M3	2385.82	6030.67	6026.86	8389.89	13579.49	13589.51	13948.65	16737.88
	(0.69%)	(0.44%)	(0.84%)	(0.45%)	(0.27%)	(0.76%)	(0.38%)	(0.63%)
P2%M2	2328.41	6157.34	6198.62	8493.64	13815.98	13909.73	14256.47	16959.1
	(0.64%)	(2.24%)	(0.23%)	(0.15%)	(1.53%)	(0.29%)	(0.43%)	(0.13%)
P2%M1	2368.78	6184.32	6224.40	8513.08	13876.66	13977.23	14388.04	17034.50
	(1.04%)	(2.81%)	(0.60%)	(0.60%)	(1.82%)	(0.51%)	(0.48%)	(0.42%)

Source: the author.

Table 7 – Experimental natural frequencies of dogbone specimens (Hz)

Sample	ρ (kg/m^3)	1F (dir. 1)	1F (dir. 2)	1T	2F (dir. 1)	2F (dir. 2)	1L	3F (dir. 1)	2T	3F (dir. 2)	2 L
D0%	2094.10	1226.50	1220.19	2489.68	3457.90	4132.12	5770.95	6724.99	9068.74	9057.30	15266.82
	(1.07%)	(3.78%)	(1.23%)	(1.62%)	(3.36%)	(0.81%)	(0.38%)	(3.15%)	(0.6%1)	(0.56%)	(0.26%)
D1%M2	2211.48	1110.76	1108.73	2313.90	3172.18	3868.18	5513.48	6242.38	8818.28	8601.05	14866.43
	(1.19%)	(1.06%)	(1.52%)	(0.18%)	(1.09%)	(1.19%)	(0.57%)	(1.01%)	(1.88%)	(0.93%)	(0.33%)
D1%M1	2115.30	1201.41	1203.11	2440.67	3427.98	4083.71	5695.33	6700.60	9165.77	8962.48	15123.14
	(0.87%)	(5.38%)	(3.25%)	(2.58%)	(3.86%)	(3.48%)	(1.95%)	(2.33%)	(1.31%)	(1.61%)	(1.12%)
D2%M2	2304.91	1082.71	1155.88	2314.53	3089.38	3986.91	5650.16	6075.04	8743.34	8819.46	15099.40
	(1.75%)	(2.67%)	(4.56%)	(2.08%)	(2.22%)	(3.25%)	(2.03%)	(1.99%)	(1.04%)	(2.45%)	(1.25%)
D2%M1	2242.31	1205.05	1252.10	2468.71	3399.99	4222.52	5897.89	6621.39	9150.40	9220.16	15505.54
	(0.21%)	(1.92%)	(1.26%)	(1.11%)	(1.86%)	(0.94%)	(0.09%)	(1.50%)	(0.92%)	(0.51%)	(0.22%)

Source: the author.

A statistical analysis (t-test) with a 95% confidence level compared the densities of samples produced by different methods. The dogbone ones produced by method 1 showed a lower density than those cast by method 2. On the other hand, the prismatic samples with 2% of fiber content showed a statistically lower density when produced by method 2 compared to method 1. The casting method can influence the compaction of the concrete, hence, the density.

Table 8 – T-test for the evaluation of densities

Test	Sample 1	Sample 2	T-value	p-value	T_{crit}	Are means different?
1	P1%M1	P1%M2	-1.343	0.228	2.447	No
2	P1%M1	P1%M3	-0.544	0.606	2.446	No
3	P2%M1	P2%M2	3.440	0.006	2.228	Yes
4	P2%M1	P2%M3	-1.319	0.219	2.262	No
5	D1%M1	D1%M2	-6.480	3e-4	2.364	Yes
6	D2%M1	D2%M2	-3.454	0.026	2.776	Yes

Source: the author.

According to the tests in table 9, the natural frequencies of the samples can be statistically different when the casting method is changed. As an example, the natural frequencies of the prismatic samples produced by method 1 differ from those produced by method 3 and those of the dogbone samples cast by methods 1 and 2 were also significantly different. Such a behavior confirms the concrete casting process influences the dynamic properties of the composite.

Table 9 – T-test for the evaluation of the fiber effect on natural frequencies

Test	Mode	Sample 1	Sample 2	T-value	p-value	T_{crit}	Are means different?
1	1F (dir.1)	P1%M1	P1%M2	1.227	0.247	2.228	No
2	1F (dir. 2)	P1%M1	P1%M2	1.697	0.120	2.228	No
3	1T	P1%M1	P1%M2	0.536	0.603	2.228	No
4	2F (dir. 1)	P1%M1	P1%M2	1.350	0.206	2.228	No
5	2F (dir. 2)	P1%M1	P1%M2	0.666	0.520	2.228	No
6	1L	P1%M1	P1%M2	2.580	0.027	2.228	Yes
7	2T	P1%M1	P1%M2	0.270	0.792	2.228	No
8	1F (dir.1)	P1%M1	P1%M3	3.77	0.004	2.262	Yes
9	1F (dir. 2)	P1%M1	P1%M3	5.764	0.002	2.570	Yes
10	1T	P1%M1	P1%M3	3.824	0.012	2.570	Yes
11	2F (dir. 1)	P1%M1	P1%M3	5.358	0.002	2.446	Yes
12	2F (dir. 2)	P1%M1	P1%M3	12.799	4.44E-7	2.262	Yes
13	1L	P1%M1	P1%M3	12.899	4.15E-7	2.262	Yes
14	2T	P1%M1	P1%M3	3.408	0.019	2.570	Yes
15	1F (dir.1)	P2%M1	P2%M2	0.297	0.771	2.228	No
16	1F (dir. 2)	P2%M1	P2%M2	1.575	0.166	2.446	No
17	1T	P2%M1	P2%M2	0.905	0.400	2.446	No
18	2F (dir. 1)	P2%M1	P2%M2	0.451	0.661	2.228	No
19	2F (dir. 2)	P2%M1	P2%M2	2.026	0.07	2.228	No
20	1L	P2%M1	P2%M2	3.488	0.006	2.228	Yes
21	2T	P2%M1	P2%M2	2.458	0.049	2.446	Yes
22	1F (dir.1)	P2%M1	P2%M3	2.136	0.085	2.570	No
23	1F (dir. 2)	P2%M1	P2%M3	7.471	3.80E-5	2.262	Yes
24	1T	P2%M1	P2%M3	4.452	0.002	2.262	Yes
25	2F (dir. 1)	P2%M1	P2%M3	2.851	0.036	2.571	Yes
26	2F (dir. 2)	P2%M1	P2%M3	7.368	4.25E-5	2.262	Yes
27	1L	P2%M1	P2%M3	11.598	1.03E-6	2.262	Yes
28	2T	P2%M1	P2%M3	5.569	3.48E-4	2.262	Yes
29	1F (dir. 1)	D1%M1	D1%M2	3.073	0.037	2.776	Yes
30	1F (dir. 2)	D1%M1	D1%M2	4.454	0.003	2.365	Yes
31	1T	D1%M1	D1%M2	4.493	0.011	2.776	Yes
32	2F (dir. 1)	D1%M1	D1%M2	4.151	0.009	2.571	Yes
33	2F (dir. 2)	D1%M1	D1%M2	3.192	0.024	2.571	Yes
34	1L	D1%M1	D1%M2	3.490	0.017	2.571	Yes
35	3F (dir. 1)	D1%M1	D1%M2	5.467	0.001	2.365	Yes
36	2T	D1%M1	D1%M2	3.671	0.008	2.365	Yes
37	3F (dir. 2)	D1%M1	D1%M2	4.442	0.003	2.365	Yes
38	2 L	D1%M1	D1%M2	3.210	0.024	2.571	Yes
39	1F (dir. 1)	D2%M1	D2%M2	7.389	7.70E-5	2.306	Yes
40	1F (dir. 2)	D2%M1	D2%M2	3.911	0.011	2.571	Yes
41	1T	D2%M1	D2%M2	6.214	2.56E-4	2.306	Yes
42	2F (dir. 1)	D2%M1	D2%M2	7.452	7.25E-5	2.306	Yes
43	2F (dir. 2)	D2%M1	D2%M2	3.889	0.012	2.571	Yes
44	1L	D2%M1	D2%M2	4.818	0.009	2.776	Yes
45	3F (dir. 1)	D2%M1	D2%M2	7.793	5.27E-5	2.306	Yes
46	2T	D2%M1	D2%M2	7.360	7.92E-5	2.306	Yes
47	3F (dir. 2)	D2%M1	D2%M2	4.052	0.015	2.776	Yes
48	2 L	D2%M1	D2%M2	4.747	0.009	2.776	Yes

Source: the author.

A careful analysis of the results revealed the natural frequencies were higher in samples of highest orientation coefficient. Figure 25 compares the casting methodologies for the first seven vibration modes of the prismatic samples. The natural frequencies of samples produced by M1 were, on average, 4% and 2.5% higher than those from M3 with 1% and 2% fiber content, respectively.

Figure 25 – Frequency obtained by different methodologies (prismatic samples)

(a) $V_f = 1\%$ (b) $V_f = 2\%$

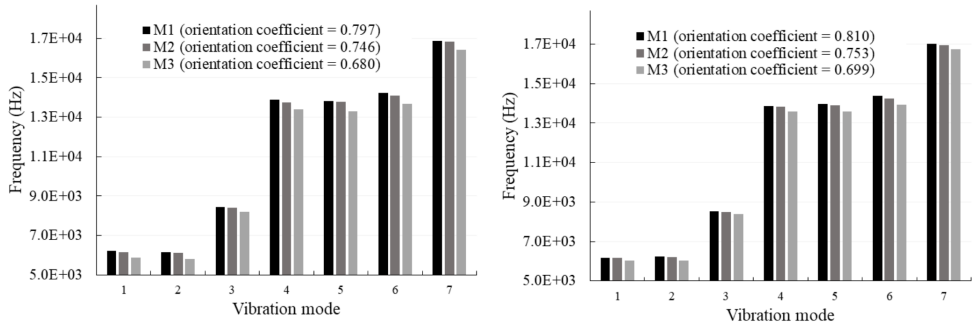

Source: the author.

Figure 26 depicts the first ten vibration modes of the dogbone samples. On average, the natural frequencies of samples produced by M1 were 5.6% and 6.8% higher than those from M3 with 1% and 2% fiber content, respectively. This trend was observed in all vibration modes, indicating a relationship between dynamic properties of the samples and fiber orientation.

Figure 26 – Frequency obtained by different methodologies (dogbone samples)

(a) $V_f = 1\%$ (b) $V_f = 2\%$

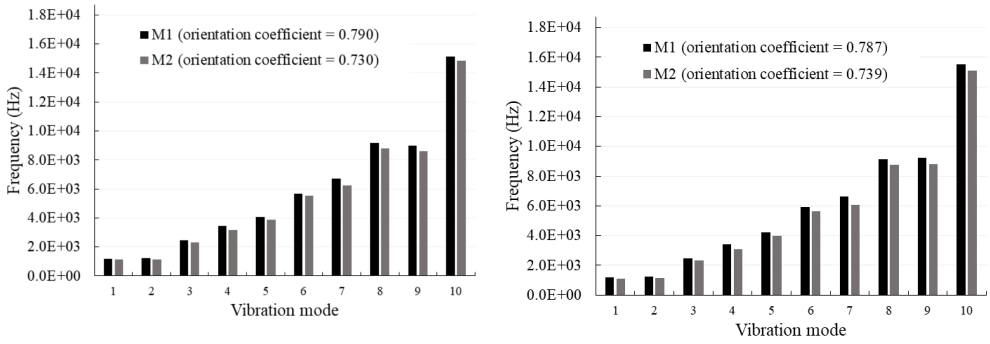

Source: the author.

The graphs below show the relationship between natural frequencies and fiber content in prismatic, dogbone, and cylindrical samples. No clear relationship is observed between volumetric fraction of fiber and natural frequencies. Since natural frequencies depend on stiffness (with a positive correlation) and mass (with a negative correlation) and the fibers increase both stiffness and mass, it seems such frequencies do not tend to increase or decrease with fiber content.

Figure 27 – Relationship between natural frequencies and fiber content (prisms)

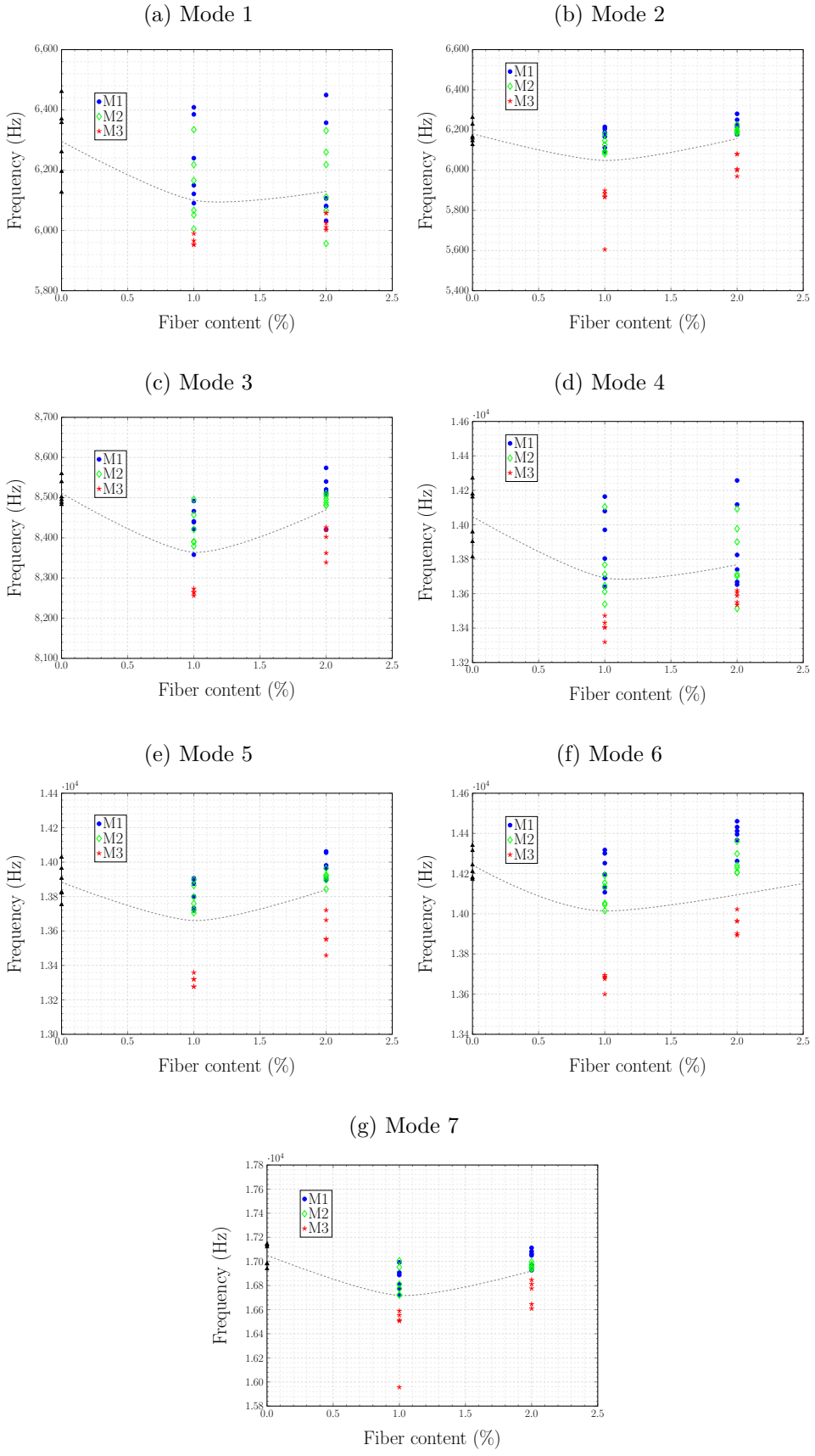

Source: the author.

Figure 28 – Relationship between natural frequencies and fiber content (dogbone)

(a) Mode 1

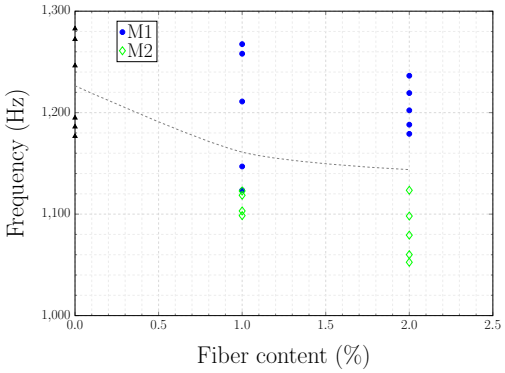

(b) Mode 2

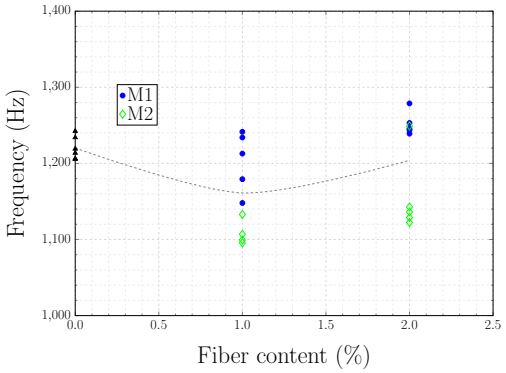

(c) Mode 3

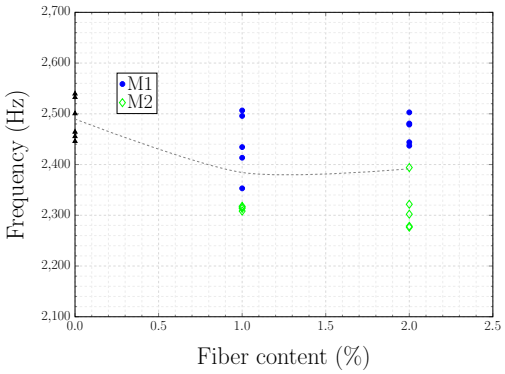

(d) Mode 4

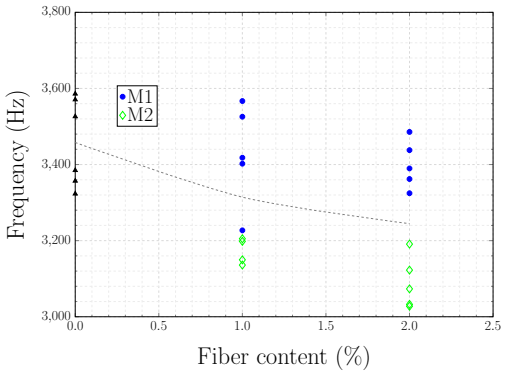

(e) Mode 5

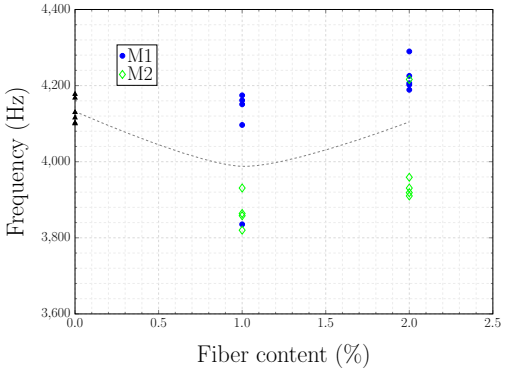

(f) Mode 6

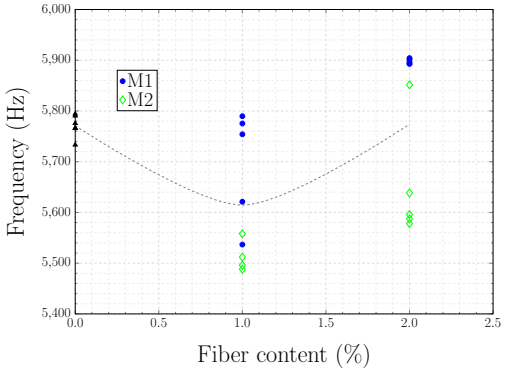

(g) Mode 7

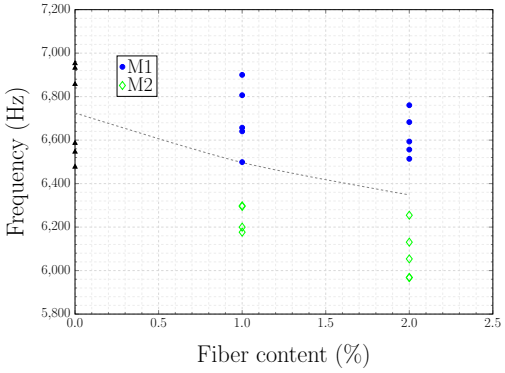

(h) Mode 8

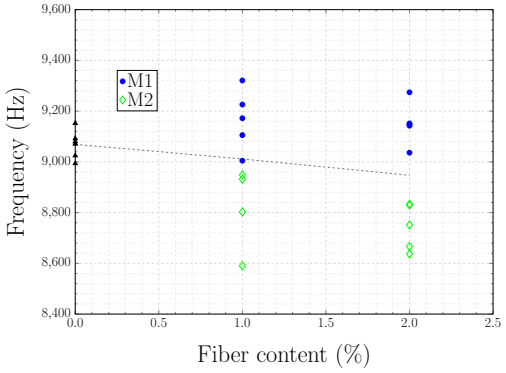

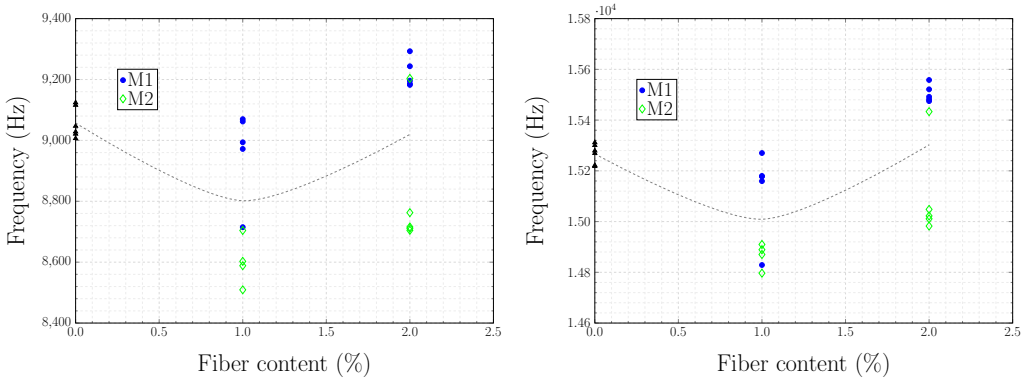

(i) Mode 9 (j) Mode 10

Source: the author.

Figure 29 – Relationship between natural frequencies and fiber content(cylindrical samples)

(a) Mode 1 (b) Mode 2

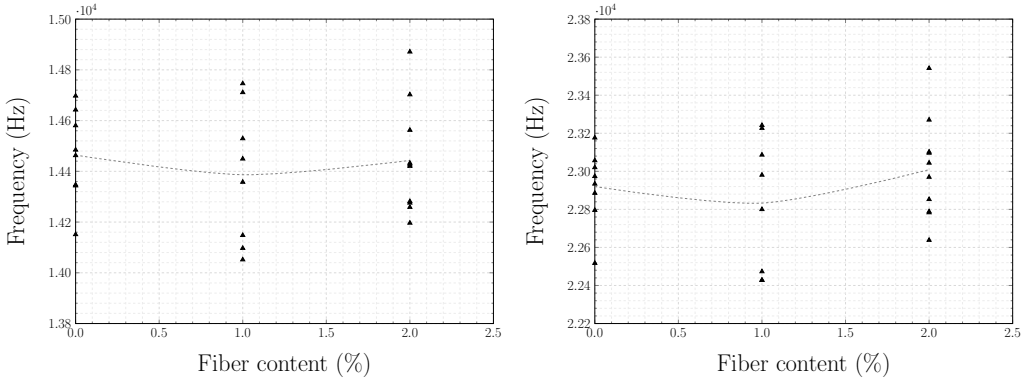

(c) Mode 3

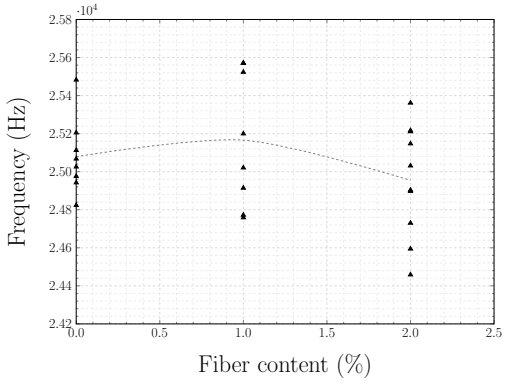

Source: the author.

As expected, due to the higher steel density than concrete, the density of the composite increased with fiber content, as shown in fig. 30.

Figure 30 – Relationship between density and fiber content

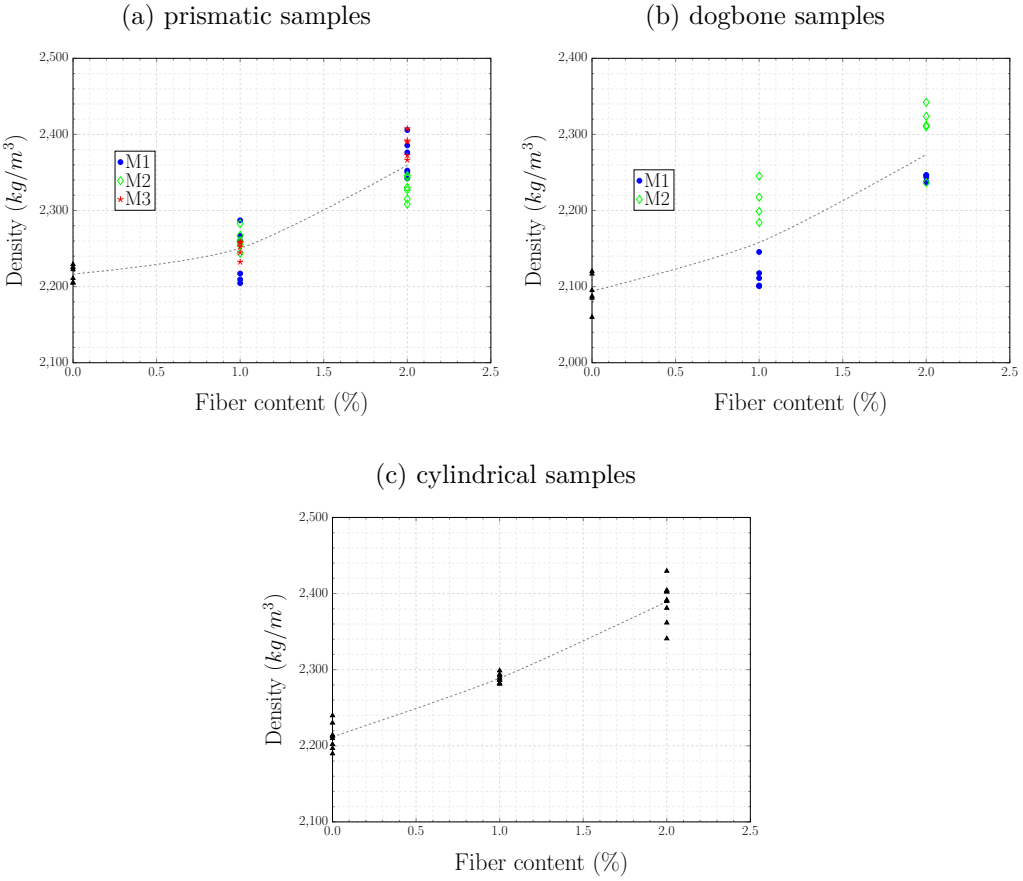

Source: the author.

3.2.3 Calibration of numerical models by genetic algorithms

Genetic algorithms calibrated the numerical models. The experimental density of the samples was considered in the numerical model, since fiber content influences mass, hence, natural frequencies. Each model was calibrated three times due to the stochastic character of the method. Figure 31 displays an example of the evolution of GAs with generations. The objective function, which is the error between experimental and numerical responses, is smaller when the orthotropic material is considered. The trend was observed in all samples, as shown in fig. 32. The results suggest the orthotropic material better represents the composite.

Figure 31 – GA evolution

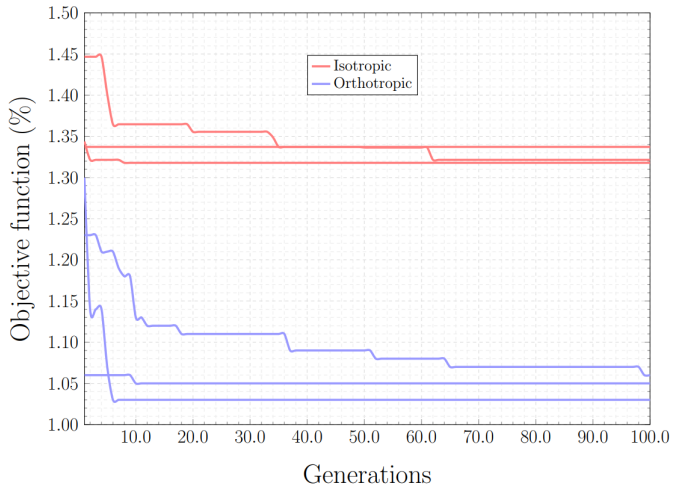

Source: the author.

Figure 32 – Objective function

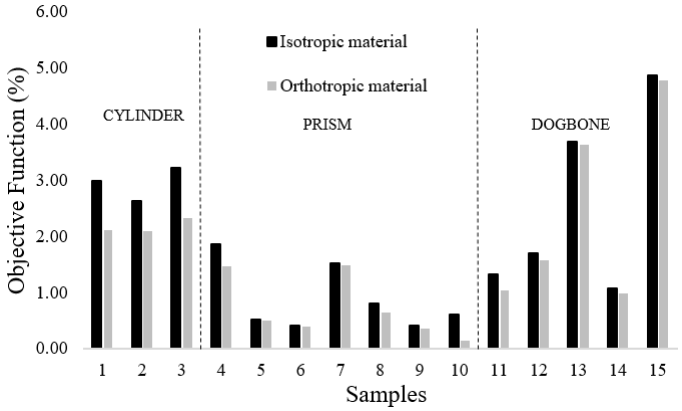

Source: the author.

Tables 10 and 11 show the elastic constants obtained by calibration. No clear trend of the influence of content and orientation of the fibers on the properties, especially when the orthotropic material was adopted, was observed. The accuracy of the elastic constants estimation is possibly not very high due to the number of variables in the problem. Besides, any minor discrepancies between numerical and experimental models may affect the values of the calibrated constants.

Table 10 – Calibrated elastic constants - orthotropic material

Sample	E_{11} (GPa)	E_{22} (GPa)	E_{33} (GPa)	ν_{12}	ν_{13}	ν_{23}	G_{12} (GPa)	G_{13} (GPa)	G_{23} (GPa)
C0%	49.10	49.10	44.50	0.180	0.180	0.180	17.20	17.25	16.90
C1%	50.10	50.70	45.20	0.217	0.182	0.180	20.00	18.05	17.90
C2%	50.20	51.50	47.70	0.207	0.195	0.187	18.30	18.10	19.25
P0%	45.60	40.80	48.50	0.210	0.214	0.212	17.80	20.60	18.50
P1%M1	46.10	47.60	50.20	0.180	0.181	0.217	18.75	19.80	20.15
P1%M2	45.90	42.40	42.70	0.182	0.180	0.183	19.50	19.40	18.05
P1%M3	42.40	42.30	42.60	0.183	0.180	0.180	18.15	17.95	18.10
P2%M1	49.80	43.90	50.00	0.185	0.182	0.181	19.80	21.70	18.40
P2%M2	48.30	43.90	51.30	0.185	0.186	0.210	20.10	20.55	20.95
P2%M3	49.20	52.50	50.00	0.195	0.219	0.217	20.90	21.25	21.60
D0%	40.70	47.50	44.10	0.188	0.215	0.202	18.35	20.45	20.45
D1%M1	50.30	46.90	51.30	0.203	0.217	0.217	19.05	21.40	20.25
D1%M2	50.80	43.60	46.40	0.180	0.207	0.180	19.05	19.95	19.35
D2%M1	52.10	51.30	44.00	0.180	0.189	0.181	21.80	18.30	18.70
D2%M2	52.10	46.00	49.60	0.181	0.187	0.181	18.10	18.75	18.20

Source: the author.

Table 11 – Calibrated elastic constants - isotropic material

Sample	$E(GPa)$	ν
C0%	43.00	0.215
C1%	44.60	0.217
C2%	46.40	0.219
P0%	45.60	0.185
P1%M1	46.10	0.192
P1%M2	45.90	0.183
P1%M3	42.40	0.180
P2%M1	49.70	0.204
P2%M2	48.30	0.187
P2%M3	49.20	0.180
D0%	47.40	0.205
D1%M1	47.10	0.200
D1%M2	43.70	0.186
D2%M1	51.20	0.219
D2%M2	45.90	0.180

Source: the author.

3.3 Conclusions

This chapter addressed an evaluation of the effect of fiber content and arrangement on the dynamic properties of UHPFRC. According to the results and discussions, the following conclusions have been drawn:

- Samples were produced by different concrete pouring procedures. M1 methodology generated a greater alignment of the fibers in the longitudinal direction of the sample, as evidenced by the image analysis. Therefore, the production of UHPFRC elements must follow a predefined methodology towards benefitting from the addition of fibers to the cement matrix.
- The sample production methodology also influeced compaction, hence, density of the composite. As an example, a statistically significant difference was observed between the densities of the dogbones produced by M1 and M2.
- The concrete placement methodology influenced the natural frequencies of the samples. As an example, the prisms and dogbones produced by M1 showed the highest natural frequency values in all vibration modes.
- No clear relationship was established between the volumetric fraction of fiber and natural frequencies. It seems natural frequencies do not tend to increase or decrease with fiber content, whereas fibers increase the composite stiffness and mass. Since a structure's natural frequency establishes a directly proportional relationship with stiffness and an inversely proportional on with mass, the addition of fibers generates a certain balance in the natural frequency.
- Finally, the numerical models were calibrated by genetic algorithms and considering the material with orthotropic or isotropic behavior. The orthotropic model showed a better fit between numerical and experimental results, suggesting the orthotropic material would be the most realistic in simulating the material. However, its application and determination of constants are more complex, which requires analyses of the impact of type of material adopted in the project.
- The accuracy of the elastic constants estimated by the calibration process is possibly not very high due to the number of calibrated variables and the inherent inaccuracies of the modeling. However, the procedure helps estimate the order of magnitude of constants, which were consistent with expectations.

The study presented in this chapter contributes to investigations on the correlation among production methodologies, fiber arrangement, and dynamic properties of the material.

FOUR

EVALUATION OF ELASTIC ANISOTROPIC RELATIONS FOR UHPFRC: NUMERICAL APPROACH

Ultra-High Performance Fiber-Reinforced Concrete (UHPFRC) relies on short fibers to provide toughness to a very brittle cementitious matrix. The influence of short fibers on the mechanical properties of UHPFRC has been extensively studied from the experimental point of view and less addressed from the theoretical/numerical one. This research aims to find a relationship among volumetric fraction, patterns of alignment, and anisotropic elastic constants of UHPFRC. The approach involves the use of three-dimensional finite element models and inclusion of fibers in simulated concrete specimens, considering several fiber arrangements and volumetric fractions. Expressions were obtained from several numerical simulations towards the prediction of anisotropic elastic properties. They were tested against a comprehensive set of experimental results from the literature, showing favorable results. The predicted elastic constants can be used in both design and homogeneous models for UHPFRC simulations.

4.1 Background

Ultra-High Performance Fiber-Reinforced Concrete (UHPFRC) is a cementitious composite material with superior mechanical properties and durability. Its dense matrix composed of cement, reactive and inert admixtures, fine aggregates, superplasticizers, and low water/binder ratio, in combination with a high volume fraction of steel fibers (2% per volume), provides ultra-high compressive strength (150 – 200 MPa), high tensile strength (7 – 11 MPa), and ductility [1].

Improvements in the mechanical properties of UHPFRC are significantly influenced by fiber distribution in the cementitious matrix. Short fibers of 13 mm length generally

adopted in UHPFRC can, in theory, be considered randomly distributed in all directions to exhibit isotropic behavior [57, 32]. However, the actual fiber distribution is affected by several factors, such as fiber volume fraction, formwork geometry, concrete fluidity and compaction, and placing method [57, 58, 9]. Considering all these factors, preferential fiber orientation along a given direction is more likely to occur, resulting in an anisotropic behavior [33, 23, 3]. The fiber distribution characteristics (e.g., fiber orientation and dispersion coefficients) must be quantified and considered in theoretical/numerical studies towards a better prediction of the mechanical properties of UHPFRC [23, 3, 59, 60].

Several numerical studies have considered UHPFRC a homogeneous material, thus assuming an idealized fiber distribution (i.e., random distribution) [61, 62, 2], and others have modeled it as a heterogeneous material composed of matrix and discrete fibers for representing the actual fiber distribution [12, 4]. In these models, the fiber distribution can be generated using the orientation coefficient, see eq. (2.4), which represents the average orientation of the fibers in the plane [4, 51, 63].

Numerical models with discretized fibers have a high computational cost. As an alternative, homogenization techniques have been adopted in studies of fiber-reinforced concretes [12, 64]. However, to the best of our knowledge, such studies are still incipient, and the literature reports no expressions that practically correlate volumetric fraction, patterns of alignment, and anisotropic elastic constants of UHPC. In this context, this study analyzes such correlations through a computational homogenization technique that enables the proposition of expressions and evaluation of the mechanical behavior of the composite as a function of phases properties, contents, and arrangements.

4.2 Methodology

Three-dimensional finite element models with the inclusion of fibers simulated the fiber reinforced concrete in Abaqus® finite element software [65]. Fiber orientation distributions with average angles of 0^{o} ($\eta_\theta = 1.0$), 15^{o} ($\eta_\theta = 0.966$), 30^{o} ($\eta_\theta = 0.866$), 45^{o} ($\eta_\theta = 0.707$), 60^{o} ($\eta_\theta = 0.500$), 75^{o} ($\eta_\theta = 0.259$), and 90^{o} ($\eta_\theta = 0$) were evaluated. Fibers randomly distributed in the matrix and fiber contents of 0.5%, 1.0%, 2.0%, and 3.0% were simulated. Such values are frequently used in practical applications of UHPFRC. Three models were simulated for each combination of fiber arrangement and volumetric fraction for assessing the variability in fiber dispersion, totaling 96 models.

UHPFRC is considered an orthotropic material in this research and the three main axes of orthotropy are defined as 1, 2, and 3. An orthotropic material is defined according to the elastic properties in the three directions, and a general one involves nine independent elastic constants [66]. Based on numerical simulations, expressions were formulated to predicting the elastic properties of the composite as a function of volumetric fraction and

fiber alignment patterns. They were tested against a set of experimental and numerical results from the literature.

4.2.1 Finite Element Model

Representative Volume Element (RVE) is an alternative to model heterogeneous structures using the Finite Element Method (FEM). It is defined as a volume of the structure that is large enough to be statistically representative of a composite, but is small enough to be considered a volume element [67].

In this research, RVE is composed of two phases, namely cementitious matrix and fibers. The cementitious matrix was modeled with type C3D8 elements, a solid three-dimensional element with eight nodes and three degrees of freedom of translation per node. The fibers were modeled with three-dimensional truss elements T3D2 embedded in the solid elements that simulated the cementitious matrix. Each of the two nodes of the T3D2 element has three degrees of translation freedom. The advantage of embedding such elements in solid elements is no degree of freedom is added to the model, since the fibers work as stiffeners, contributing to the stiffness of the elements in which they are embedded. Perfect adherence between the fibers and the cementitious matrix is considered.

The material under study is UHPC reinforced with straight steel fibers of 13 mm length and 0.2 mm diameter. The elastic properties of the cementitious matrix (E_m = 43.965 GPa and $\nu_m = 0.20$) and steel fibers (E_f = 200 GPa and $\nu_f = 0.30$) were adopted according to the data provided in Oliveira [4].

4.2.2 Fiber generation

The fibers were generated through a code implemented in Python. The steps of the algorithm are: (1) the geometry of RVE and fibers, volume fraction V_f and orientation coefficient η_θ are defined; (2) number of fibers n_f to be generated is calculated; (3) midpoints of the fibers (x_m, y_m, z_m) and the angles (α, β) are determined (see fig. 33); (4) end nodes of the fibers (x_j^i, y_j^i, z_j^i) are calculated; (5) positions of the fibers are checked to see if they are inside of the RVE; (6) and the coordinates of the fiber endpoints are saved in a .inp output file, which is imported into Abaqus®. Steps (3) to (5) are repeated until n_f fibers have been generated. Figure 34 displays a flowchart of the fiber generation methodology.

Figure 33 – Definition of fiber inclination angles α and β

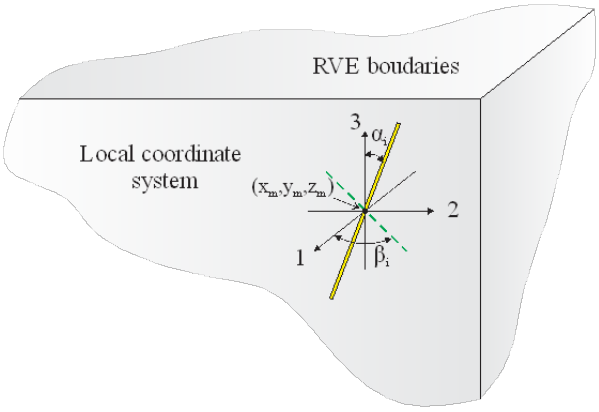

Source: the author.

Figure 34 – Fiber generation methodology

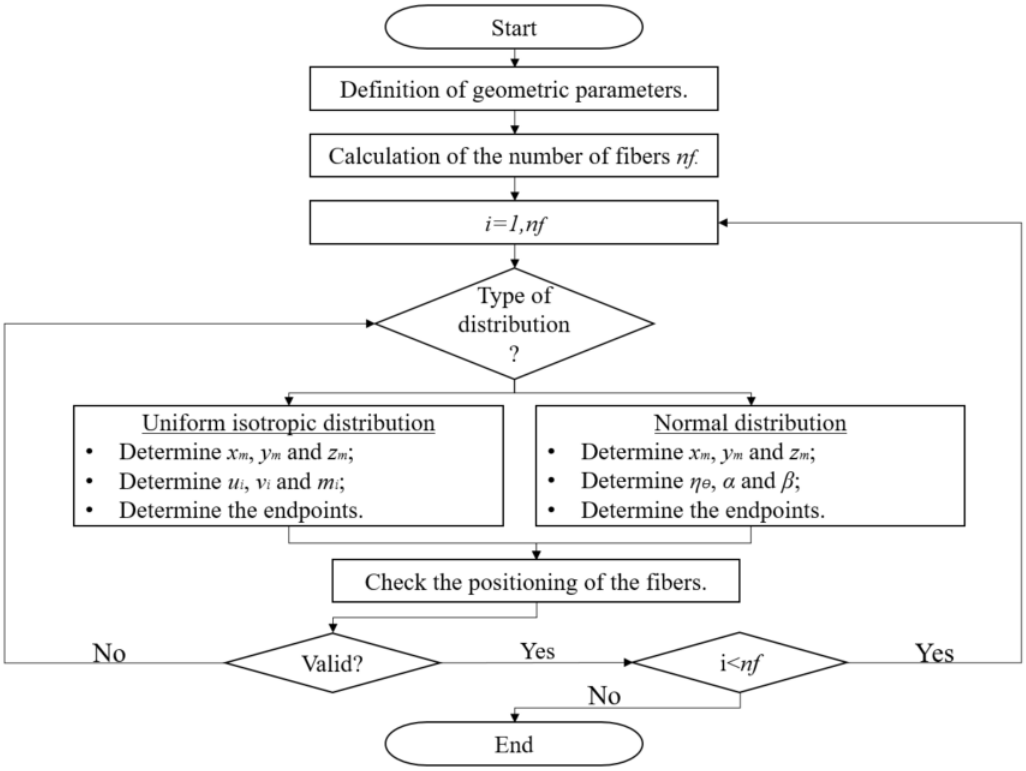

Source: the author.

The orientation coefficient was defined as the average of the cosines of the angle between the fibers and axis 3. As an example, $\eta_\theta = 0$ represents fibers contained on the 1-2 plane, $\eta_\theta = 1$ represents those perfectly aligned in direction 3, and orientation coefficient values between 0 and 1 represent intermediate situations (see fig. 35).

Figure 35 – Fiber orientation

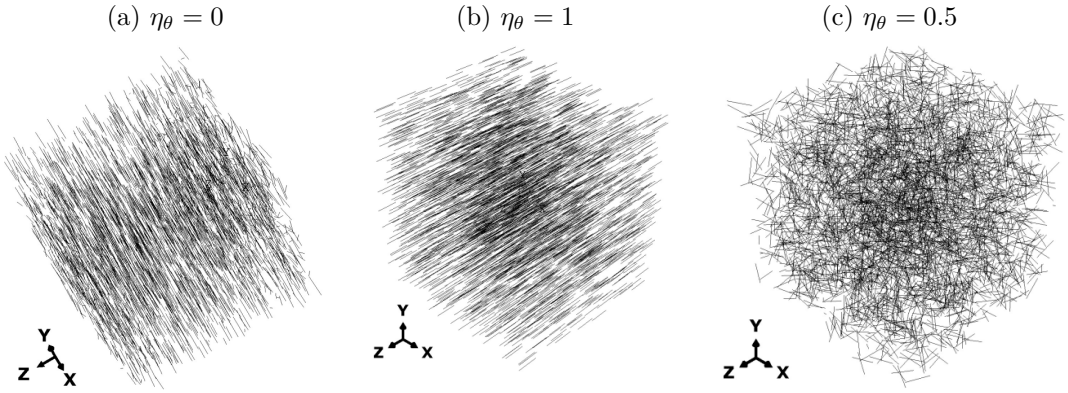

Source: the author.

As shown in fig. 33, the fiber orientation can be expressed by a pair of angles (α and β), where α is the inclination that the fiber makes with the principal axis (in this study, 3-axis) and β is the angle of the fiber projection on the 1–2 plane with 1-axis. α and β were obtained by

$$\alpha = z\sigma_\theta + \theta_m, \tag{4.1}$$

$$\beta \sim U([0, 2\pi]), \tag{4.2}$$

where θ_m and σ_θ are the average orientation angle of the fibers and the standard deviation of θ, respectively, and z is the reduced standard variable of the normal distribution.

Laranjeira [68] proved with experimental results that the average orientation angle and standard deviation are correlated by the orientation coefficient as follows: $\theta_m = \arccos(\eta_\theta)$, $\sigma_\theta = 90^o\eta_\theta(1 - \eta_\theta)$. So, for each orientation coefficient η_θ evaluated, θ_m and σ_θ were determined.

The coordinates of the midpoint of the fibers (x_m, y_m, z_m) are generated randomly within the defined volume domain. The coordinates of ends j of each fiber can be calculated as follows:

$$x_i^j = x_{i,m} \pm \frac{L_f}{2}\sin(\alpha)\cos(\beta), \tag{4.3}$$

$$y_i^j = y_{i,m} \pm \frac{L_f}{2}\sin(\alpha)\sin(\beta), \tag{4.4}$$

$$z_i^j = z_{i,m} \pm \frac{L_f}{2}\cos(\alpha). \tag{4.5}$$

Fibers randomly distributed were generated through a versor $\hat{n}_i = (u_i, v_i, m_i)$ with $u_i = \eta_x/||n_i||$, $v_i = \eta_y/||n_i||$ and $m_i = \eta_z/||n_i||$, where $||n_i||$ is the norm of vector $n_i = (\eta_x, \eta_y, \eta_z)$ and variables η_x , η_y and η_z vary randomly from -1 to 1. Therefore, the coordinates of the fiber nodes are computed as: $x_i^j = x_{i,m} \pm L_f/2 \cdot u_i$, $y_i^j = y_{i,m} \pm L_f/2 \cdot v_i$ and $z_i^j = z_{i,m} \pm L_f/2 \cdot m_i$.

4.2.3 Computational homogenization

Homogenization techniques replace a heterogeneous structure with a homogeneous one that globally exhibits the same behavior. In other words, the principle of homogenization is the determination of the effective properties of an equivalent homogeneous material that is mechanically analogous to an RVE. The technique enbales the obtaining of a material that indirectly considers both orientation and content of the phases.

An RVE is used by applying six independent loading cases and periodic boundary conditions. The average stress-average strain relation for a nonhomogeneous material is given by

$$\langle \sigma_{i,j} \rangle = C^H_{ijkl} \langle \varepsilon_{k,l} \rangle, \tag{4.6}$$

where C^H_{ijkl} is the homogenized stiffness matrix and $\langle \sigma_{i,j} \rangle$ and $\langle \varepsilon_{k,l} \rangle$ are volume averaged stress and strain tensors of the RVE, respectively. The average stress and strain fields are calculated as follows:

$$\langle \sigma_{ij} \rangle = \frac{1}{V} \left[\int_{V_m} \sigma^m_{ij} dV_m + \int_{V_f} \sigma^f_{ij} dV_f \right], \tag{4.7}$$

$$\langle \varepsilon_{ij} \rangle = \frac{1}{V} \left[\int_{V_m} \varepsilon^m_{ij} dV_m + \int_{V_f} \varepsilon^f_{ij} dV_f \right], \tag{4.8}$$

where V is the volume of the RVE and V_m and V_f are the volume of the matrix and fibers, respectively. Alternatively, the average stress and strain can be obtained by the displacements and reactions of the boundary conditions [69]:

$$\langle \sigma_{ij} \rangle = \frac{1}{2V} \int_s (t_i x_j + t_j x_i)\, ds, \tag{4.9}$$

$$\langle \varepsilon_{ij} \rangle = \frac{1}{2V} \int_s (u_i n_j + u_j n_i)\, ds, \tag{4.10}$$

where s is the surface of the RVE, t is the force in the contour, x is the position vector, u is the displacement, and n is the normal unit vector.

According to eq. (4.6), the components of the homogenized stiffness matrix can be obtained by applying six load cases of strain separately and calculating the corresponding volume averaged stress tensors. The following equations show the periodic boundary conditions associated with each loading case.

$$u_{x=0} = v_{y=0} = v_{y=l_y} = w_{z=0} = w_{z=lz} = 0, \;\; u_{x=l_x} = \varepsilon_{11} l_x, \tag{4.11}$$

$$u_{x=0} = u_{x=l_x} = v_{y=0} = w_{z=0} = w_{z=lz} = 0, \;\; v_{y=l_y} = \varepsilon_{22} l_y, \tag{4.12}$$

$$u_{x=0} = u_{x=l_x} = v_{y=0} = v_{l=l_y} = w_{z=0} = 0, \;\; w_{z=l_z} = \varepsilon_{33} l_z, \tag{4.13}$$

$$u_{y=0} = v_{x=l_x} = v_{x=0} = w_{x,y,z=0} = w_{x=l_x,y=l_y,z=l_z} = 0, \;\; u_{y=l_y} = \varepsilon_{12} l_y, \tag{4.14}$$

$$u_{z=0} = v_{x,y,z=0} = v_{x=l_x,y=l_y,z=l_z} = w_{x=l_x} = w_{x=0} = 0, \;\; u_{z=l_z} = \varepsilon_{13} l_z, \tag{4.15}$$

$$u_{x,y,z=0} = u_{x=l_x,y=l_y,z=l_z} = v_{z=0} = w_{y=l_y} = w_{y=0} = 0, \;\; v_{z=l_z} = \varepsilon_{23} l_z. \tag{4.16}$$

The homogeneous stiffness matrix is calculated by eq. (4.6) from the average stress, eq. (4.9), and strain, eq. (4.10). The inversion of the stiffness matrix determines flexibility matrix S_{ij}. Therefore, the engineering constants are calculated as

$$E_{11} = 1/S_{11}, \;\; E_{22} = 1/S_{22}, \;\; E_{33} = 1/S_{33}, \tag{4.17}$$

$$\nu_{12} = -S_{12}/S_{11}, \;\; \nu_{13} = -S_{13}/S_{11}, \;\; \nu_{23} = -S_{23}/S_{22}, \tag{4.18}$$

$$G_{12} = 1/S_{44}, \;\; G_{13} = 1/S_{55}, \;\; G_{23} = 1/S_{66}. \tag{4.19}$$

4.2.4 Effect of RVE size

The RVE size must be well defined so that the model indeed represents the material [70, 71]. For fiber reinforced concrete, cube sides between 5mm and 400 mm were already used [69, 72, 16]. Therefore, three sizes were evaluated for the length of the cube (l), namely 15 mm, 60 mm, and 120 mm. Figure 36 shows the fiber distribution in RVEs with 2% fiber content, generated randomly. Five samples were generated for each RVE size for the assessment of the fiber dispersion influence.

Figure 36 – Distribution of fibers in RVE (a) 15 mm (b) 60 mm (c) 120 mm

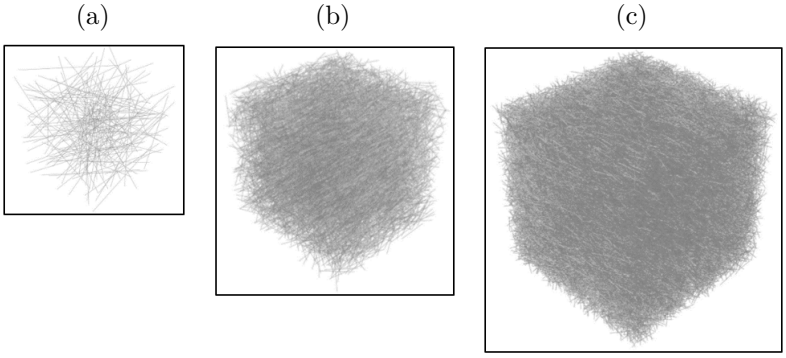

Source: the author.

4.2.5 Mesh sensitiveness

The influence of mesh discretization on homogenized properties was analyzed in RVE with edges divided into 1, 10, and 20 elements, resulting in 1, 1000, and 8000 elements per cube, as shown in fig. 37. Therefore, finite elements ranging from 0.75 mm to 15 mm (l = 15 mm), from 3 mm to 60 mm (l = 60 mm), and from 6 mm to 120 mm (l = 120 mm) were analyzed.

Figure 37 – Evaluated meshes (a) 1 element (b) 1000 elements (c) 8000 elements

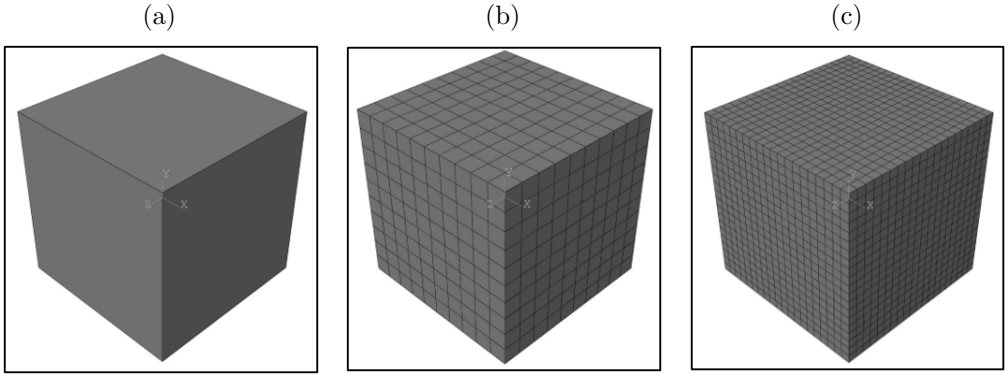

Source: the author.

4.3 Results and discussions

This section evaluates the mesh and size effect of RVE, introduces elastic constants obtained by the homogenization method, and proposes expressions for their prediction.

4.3.1 RVE size and mesh analysis

The results of the models with a mesh composed of 8000 finite elements showed the variation in the engineering constants was small as a function of the RVE size. However, the dispersion of the results was smaller for the RVE of 120 mm length, as illustrated in the following figure. Therefore, an RVE of 120 mm length was adopted for further analyses.

Figure 38 – RVE size effect

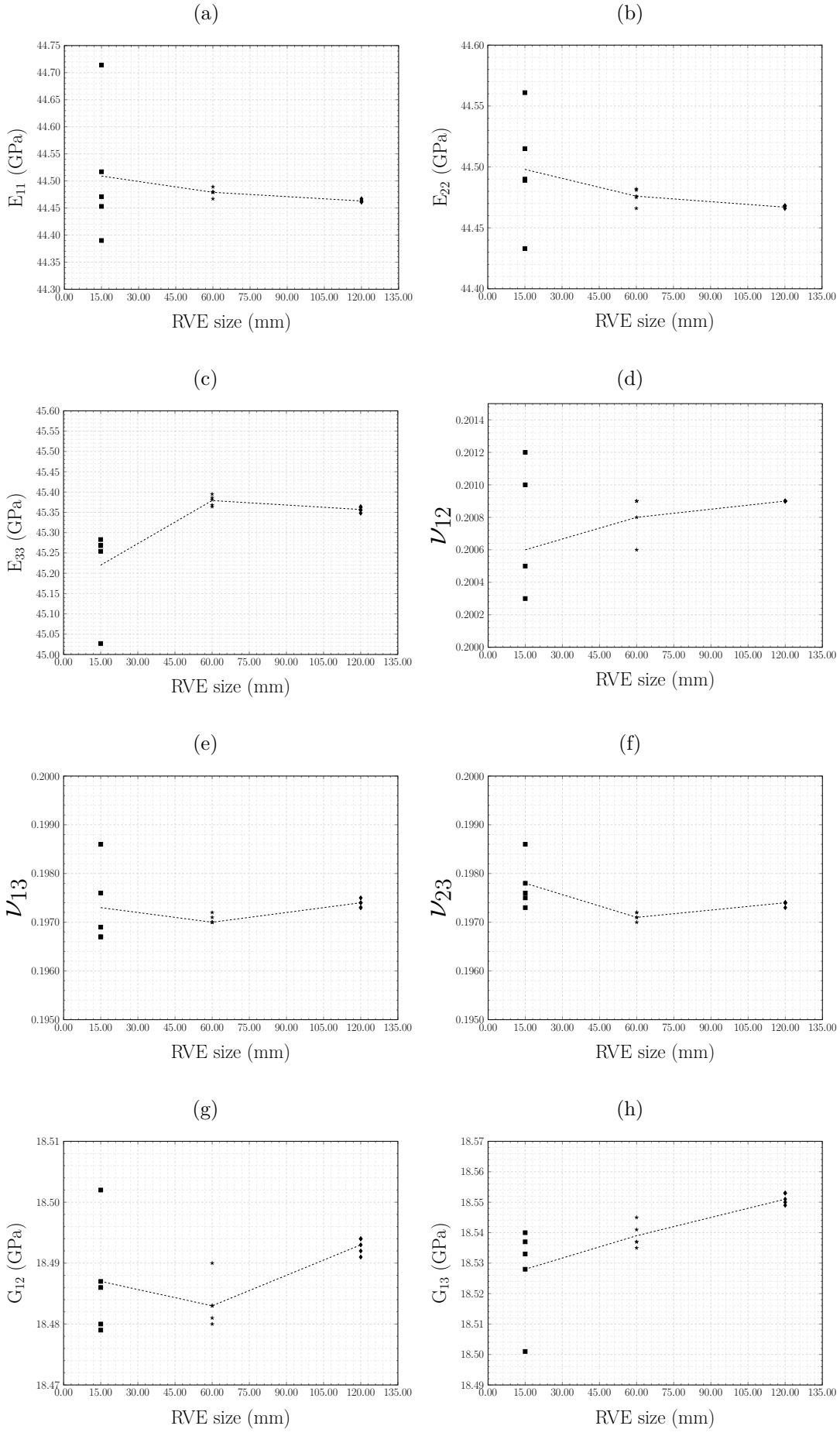

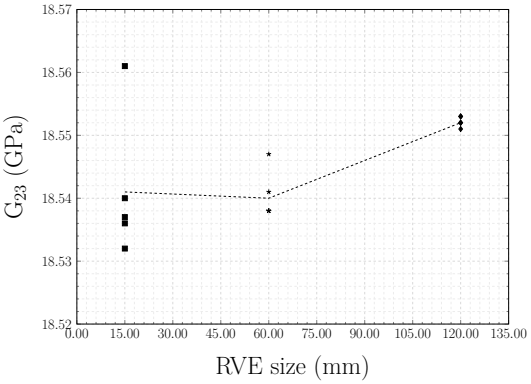

(i)

Source: the author.

The results of the models with an RVE of 120 mm showed the variation in the engineering constants was small as a function of the RVE mesh, as can be seen in the following figure. Due to the low computational cost in the simulation, the most refined mesh, with 8000 finite elements, was adopted.

Figure 39 – Mesh size effect

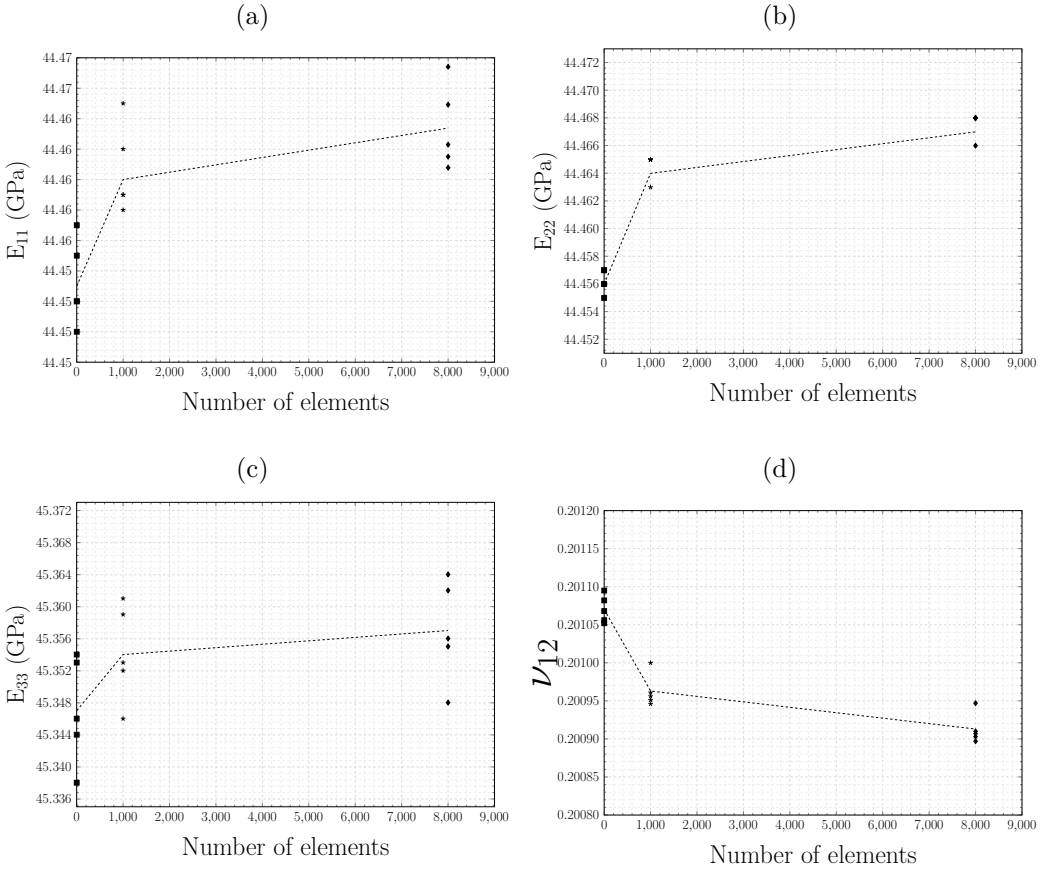

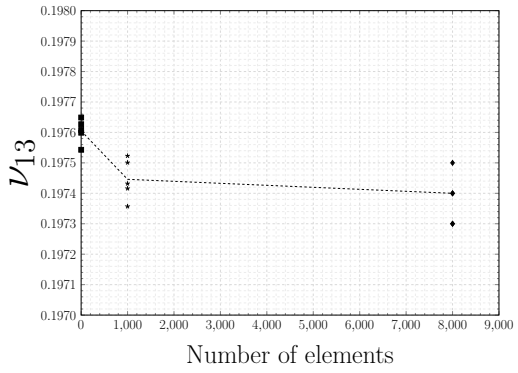

(e)

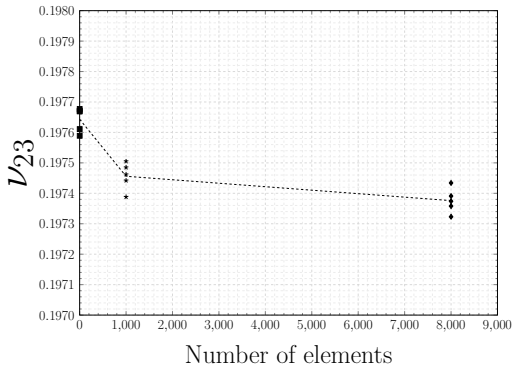

(f)

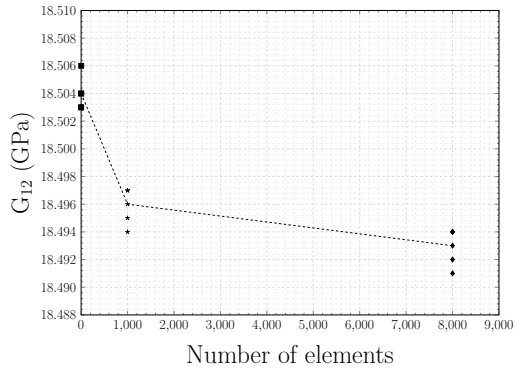

(g)

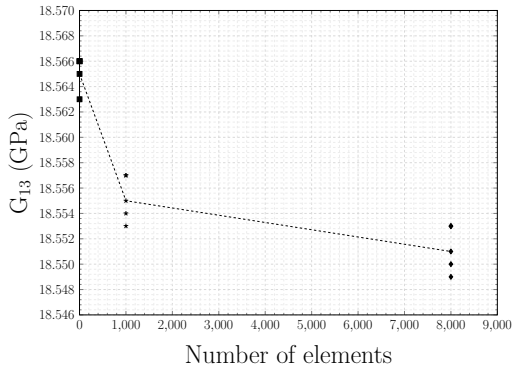

(h)

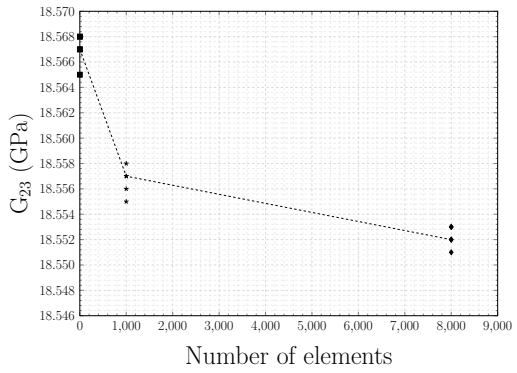

(i)

Source: the author.

4.3.2 Results from homogenization

Table 12 shows the results from homogenization. The nine elastic constants that define the stiffness matrix of the orthotropic material were determined for each case. Since angle β was obtained through a uniform distribution, the $E_{11} \approx E_{22}$, $\nu_{13} \approx \nu_{23}$, and $G_{13} \approx G_{23}$ relationships were observed, suggesting an isotropic behavior in the 1-2 plane. Coefficient μ was used in the evaluation of the anisotropy rate of the material; it measures the correlation between the stiffness matrix constants - the closer the μ to unity, the closer the material to isotropy [69, 70]. μ can be defined as

$$\mu = \frac{1}{G_{12}} \cdot \frac{E_{11}}{2(1+\nu_{12})}. \tag{4.20}$$

Values of μ ranging from 1.0050 to 0.9937 are obtained for volumetric fractions varying from 0% to 3%, confirming hypotheses that the material is isotropic on the 1-2 plane.

Elastic modulus E_{33} is maximum for fibers aligned with direction 3 ($\eta_\theta = 1$). Regarding fibers on the 1-2 plane ($\eta_\theta = 0$), E_{33} is minimum and the values of E_{11} and E_{22} are maximum. That behavior is illustrated in fig. 40 through the relationship between E_{33} and E_{11}. Note for $\eta_\theta = 0.5$, E_{33}/E_{11} ratio is close to one, which is one of the characteristics of an isotropic material. For η_θ between 0.5 and 1, the contribution of fibers in direction 3 is greater than in the other directions and for η_θ between 0 and 0.5, the contribution is greater in directions 1 and 2.

The results for random distribution and orientation and for $\eta_\theta = 0.5$ are quite close. Therefore, $\eta_\theta = 0.5$ can simulate fibers randomly distributed in the volume.

Figure 40 – E_{33}/E_{11} ratio as a function of η_θ

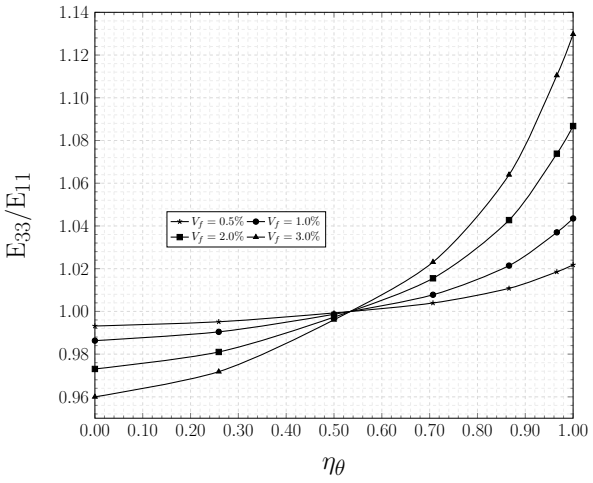

Source: the author.

The values of E_{11}, E_{22}, and E_{33} increase with the fiber content in all models, as shown in fig. 41. Regarding fiber orientation, E_{33} increases with the higher orientation coefficient, whereas E_{11} and E_{22} decrease with the orientation coefficient.

Figure 41 – Variation in elastic modulus with fiber content and orientation

(a)

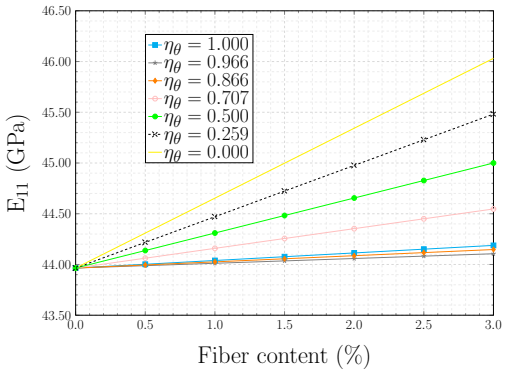

(b)

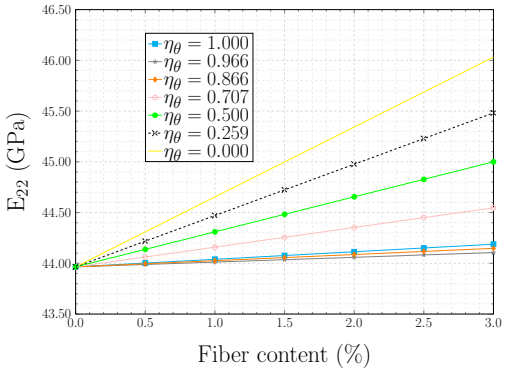

(c)

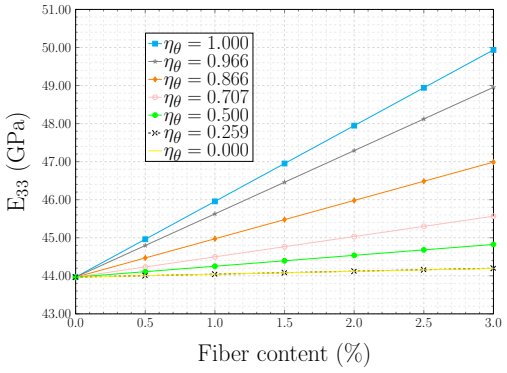

Source: the author.

In some cases, the values of ν_{12}, ν_{13} and ν_{23} increase and, in others, are reduced with the fiber volume, as shown in fig. 42. Hyer [73] explains fiber stiffness tends to contain the Poisson effect in the direction they are aligned, whereas in transversal directions, the Poisson effect is greater due to the influence of only the matrix and the diametrical direction of the fiber. ν_{13} and ν_{23} are reduced for fibers aligned with direction 3 ($\eta_\theta = 1$) with the presence of fibers, i.e., when a deformation is applied in either direction 1, or in direction 2, the deformation is restricted in direction 3 due to the stiffness of the fibers. On the other hand, ν_{12} increases with fiber content, since there is no contribution of fibers on plane 12.

Figure 42 – Variation in Poisson coefficient with fiber content and orientation

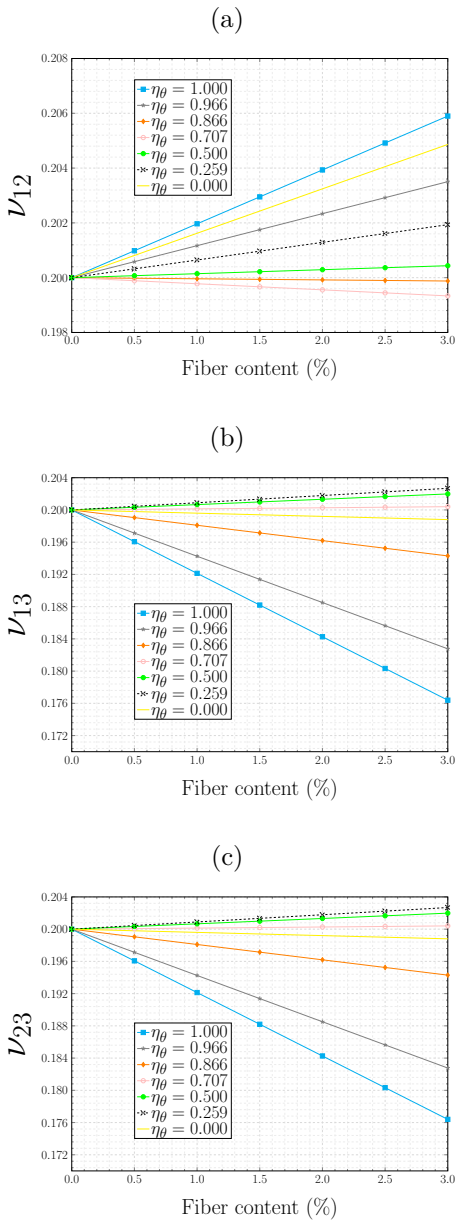

Source: the author.

Depending on the orientation coefficient, the values of G_{12}, G_{13}, and G_{23} either remain constant, or increase with fiber content, as shown in fig. 43. Transverse modulus of elasticity G_{12} is higher when the fibers are contained in the 1-2 plane; therefore, the orientation coefficient is zero. The contribution of fibers decreases when they begin to align with direction 3 preferentially. Transverse modulus of elasticity G_{13} and G_{23} are maximum when the fibers are on an inclined plane, with an average orientation angle around 30º to 45º, and are minimal when the fibers are contained in plane 1-2 ($\eta_\theta = 0$) or aligned in plane 3 ($\eta_\theta = 1$). The results are consistent with the expected behavior.

Figure 43 – Variation in transverse elastic modulus with fiber content and orientation

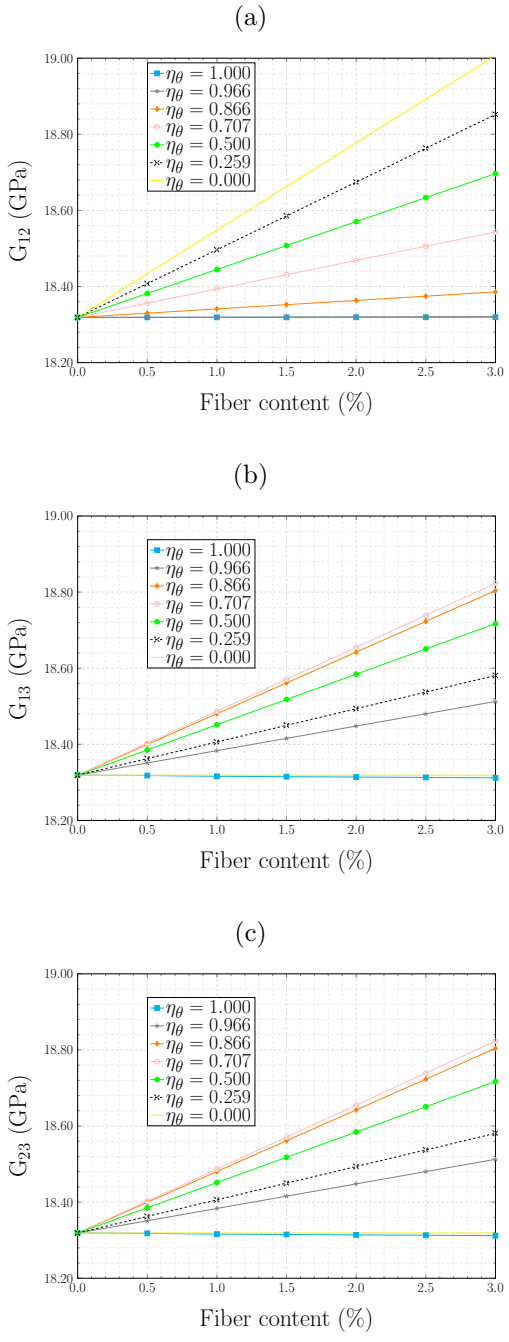

Source: the author.

Table 12 – Summary of the results of computational homogenization (GPa)

Model	E_{11}	E_{22}	E_{33}	ν_{12}	ν_{13}	ν_{23}	G_{12}	G_{13}	G_{23}
$\eta_\theta = 1.000$	44.004	44.004	44.963	0.201	0.196	0.196	18.319	18.319	18.319
0.5%	(1.5E-4)	(9.2E-5)	(2.9E-4)	(4.0E-6)	(1.6E-5)	(1.0E-5)	(0.0E+0)	(0.0E+0)	(0.0E+0)
$\eta_\theta = 1.000$	44.041	44.041	45.957	0.202	0.192	0.192	18.319	18.319	18.319
1.0%	(2.5E-4)	(7.9E-5)	(4.3E-4)	(6.8E-6)	(2.7E-5)	(8.7E-6)	(0.0E+0)	(0.0E+0)	(0.0E+0)
$\eta_\theta = 1.000$	44.111	44.111	47.938	0.204	0.184	0.184	18.319	18.319	18.319
2.0%	(8.0E-4)	(2.0E-4)	(6.6E-4)	(2.2E-5)	(8.8E-5)	(2.2E-5)	(0.0E+0)	(0.0E+0)	(0.0E+0)
$\eta_\theta = 1.000$	44.175	44.176	49.909	0.206	0.177	0.177	18.319	18.319	18.319
3.0%	(1.5E-4)	(2.7E-4)	(2.8E-4)	(4.0E-6)	(1.6E-5)	(3.0E-5)	(0.0E+0)	(0.0E+0)	(0.0E+0)
$\eta_\theta = 0.966$	43.992	43.992	44.807	0.201	0.197	0.197	18.319	18.350	18.350
0.5%	(1.4E-4)	(2.8E-4)	(2.1E-4)	(2.9E-6)	(1.3E-5)	(3.3E-5)	(4.0E-5)	(6.9E-5)	(1.6E-4)
$\eta_\theta = 0.966$	44.018	44.018	45.647	0.201	0.194	0.194	18.320	18.381	18.381
1.0%	(3.4E-4)	(3.7E-4)	(4.1E-4)	(7.5E-6)	(3.1E-5)	(4.3E-5)	(0.0E+0)	(8.7E-4)	(8.4E-4)
$\eta_\theta = 0.966$	44.067	44.067	47.321	0.203	0.188	0.188	18.321	18.444	18.443
2.0%	(4.8E-4)	(3.5E-4)	(7.9E-4)	(1.4E-5)	(5.2E-5)	(2.4E-5)	(4.0E-5)	(3.9E-4)	(8.7E-4)
$\eta_\theta = 0.966$	44.112	44.112	48.986	0.204	0.183	0.183	18.323	18.505	18.506
3.0%	(5.6E-4)	(3.2E-4)	(1.5E-3)	(1.4E-5)	(5.3E-5)	(5.5E-5)	(4.0E-5)	(7.3E-4)	(1.4E-3)
$\eta_\theta = 0.866$	43.994	43.994	44.469	0.200	0.199	0.199	18.330	18.401	18.400
0.5%	(3.7E-4)	(2.2E-4)	(6.1E-4)	(8.1E-6)	(1.6E-5)	(1.7E-5)	(1.8E-4)	(1.8E-4)	(5.3E-4)
$\eta_\theta = 0.866$	44.023	44.024	44.967	0.200	0.198	0.198	18.341	18.482	18.482
1.0%	(5.3E-4)	(5.5E-4)	(2.0E-3)	(1.3E-5)	(6.4E-5)	(5.7E-5)	(2.8E-4)	(8.9E-4)	(2.5E-4)
$\eta_\theta = 0.866$	44.081	44.081	45.965	0.200	0.196	0.196	18.363	18.648	18.646
2.0%	(2.3E-4)	(3.6E-4)	(4.7E-4)	(5.9E-6)	(2.9E-5)	(1.1E-5)	(1.6E-4)	(9.6E-4)	(4.4E-4)
$\eta_\theta = 0.866$	44.138	44.138	46.961	0.200	0.195	0.194	18.385	18.811	18.808
3.0%	(5.8E-4)	(1.4E-3)	(6.9E-3)	(1.7E-5)	(3.9E-5)	(1.5E-4)	(8.0E-5)	(9.7E-4)	(4.1E-3)
$\eta_\theta = 0.707$	44.063	44.063	44.236	0.200	0.200	0.200	18.357	18.402	18.402
0.5%	(4.1E-4)	(3.6E-4)	(7.1E-4)	(9.7E-6)	(1.3E-5)	(7.4E-6)	(4.6E-4)	(1.0E-3)	(2.5E-4)
$\eta_\theta = 0.707$	44.160	44.157	44.503	0.200	0.200	0.200	18.394	18.487	18.488
1.0%	(4.4E-4)	(2.0E-3)	(2.3E-3)	(2.4E-5)	(2.8E-5)	(4.3E-5)	(8.3E-4)	(9.4E-4)	(1.3E-3)
$\eta_\theta = 0.707$	44.354	44.352	45.042	0.200	0.200	0.200	18.469	18.654	18.653
2.0%	(1.9E-3)	(4.2E-3)	(2.3E-3)	(9.7E-6)	(1.3E-4)	(6.6E-5)	(4.9E-4)	(3.7E-3)	(1.2E-3)
$\eta_\theta = 0.707$	44.550	44.546	45.579	0.199	0.200	0.200	18.544	18.820	18.819
3.0%	(1.8E-3)	(1.3E-3)	(4.0E-3)	(4.1E-5)	(4.0E-5)	(4.5E-5)	(1.1E-3)	(2.4E-4)	(6.3E-4)
$\eta_\theta = 0.500$	44.139	44.139	44.107	0.200	0.200	0.200	18.382	18.385	18.386
0.5%	(2.8E-3)	(1.4E-3)	(1.6E-3)	(2.5E-5)	(3.9E-5)	(9.6E-6)	(8.7E-4)	(5.6E-4)	(4.6E-4)
$\eta_\theta = 0.500$	44.309	44.311	44.249	0.200	0.201	0.201	18.446	18.452	18.452
1.0%	(1.7E-3)	(4.0E-3)	(2.7E-3)	(4.2E-5)	(2.7E-5)	(5.0E-5)	(2.6E-4)	(9.6E-4)	(9.8E-4)
$\eta_\theta = 0.500$	44.653	44.656	44.533	0.200	0.201	0.201	18.571	18.586	18.586
2.0%	(1.4E-3)	(3.8E-3)	(2.4E-3)	(3.9E-5)	(9.8E-5)	(7.7E-5)	(1.0E-3)	(3.1E-3)	(2.2E-3)
$\eta_\theta = 0.500$	44.998	45.000	44.821	0.200	0.202	0.202	18.696	18.719	18.718
3.0%	(7.4E-4)	(2.7E-3)	(2.2E-3)	(7.8E-6)	(2.2E-5)	(3.1E-5)	(1.1E-3)	(1.3E-3)	(2.1E-3)
$\eta_\theta = 0.259$	44.219	44.218	44.004	0.200	0.200	0.200	18.408	18.362	18.362
0.5%	(7.3E-4)	(2.2E-3)	(1.7E-4)	(4.8E-5)	(2.5E-5)	(7.5E-6)	(1.3E-3)	(8.6E-4)	(2.4E-4)
$\eta_\theta = 0.259$	44.470	44.468	44.044	0.201	0.201	0.201	18.498	18.406	18.406
1.0%	(2.3E-3)	(2.6E-3)	(7.5E-4)	(2.9E-5)	(1.8E-5)	(7.4E-6)	(1.4E-3)	(8.7E-4)	(6.8E-4)
$\eta_\theta = 0.259$	44.976	44.974	44.122	0.201	0.202	0.202	18.674	18.494	18.493
2.0%	(5.2E-3)	(3.7E-3)	(2.5E-4)	(3.0E-5)	(8.4E-6)	(3.7E-5)	(5.7E-4)	(4.8E-4)	(1.4E-3)
$\eta_\theta = 0.259$	45.482	45.479	44.199	0.202	0.203	0.203	18.853	18.581	18.581
3.0%	(2.5E-3)	(1.5E-3)	(1.1E-3)	(6.5E-5)	(2.5E-5)	(4.6E-5)	(1.1E-3)	(2.2E-4)	(1.1E-3)
$\eta_\theta = 0.000$	44.307	44.312	44.005	0.201	0.200	0.200	18.434	18.319	18.319
0.5%	(2.3E-3)	(3.3E-3)	(1.6E-4)	(3.6E-5)	(9.0E-6)	(1.2E-5)	(1.1E-3)	(0.0E+0)	(0.0E+0)
$\eta_\theta = 0.000$	44.654	44.655	44.043	0.202	0.200	0.200	18.550	18.319	18.319
1.0%	(2.1E-3)	(7.6E-4)	(4.1E-4)	(2.4E-5)	(5.9E-6)	(1.5E-5)	(7.1E-4)	(0.0E+0)	(0.0E+0)
$\eta_\theta = 0.000$	45.340	45.348	44.119	0.203	0.199	0.199	18.779	18.319	18.319
2.0%	(3.9E-3)	(9.7E-4)	(2.2E-4)	(4.4E-5)	(1.1E-5)	(9.7E-6)	(5.2E-4)	(0.0E+0)	(0.0E+0)
$\eta_\theta = 0.000$	46.033	46.034	44.192	0.205	0.199	0.199	19.006	18.319	18.319
3.0%	(1.8E-3)	(5.3E-3)	(1.5E-4)	(6.1E-5)	(1.5E-5)	(2.4E-5)	(1.5E-3)	(0.0E+0)	(0.0E+0)
Random	44.111	44.109	44.108	0.200	0.200	0.200	18.391	18.391	18.390
0.5%	(1.9E-3)	(1.1E-3)	(7.1E-4)	(2.6E-5)	(2.0E-5)	(3.1E-5)	(4.9E-4)	(7.0E-4)	(5.7E-4)
Random	44.253	44.253	44.256	0.201	0.201	0.201	18.461	18.462	18.463
1.0%	(2.2E-3)	(1.3E-3)	(2.7E-3)	(1.9E-5)	(5.7E-5)	(1.9E-6)	(1.3E-3)	(1.6E-3)	(3.3E-4)
Random	44.544	44.545	44.542	0.201	0.201	0.201	18.604	18.603	18.606
2.0%	(2.3E-3)	(1.5E-3)	(2.0E-3)	(6.5E-5)	(3.7E-5)	(1.7E-5)	(1.7E-3)	(1.2E-3)	(3.0E-4)
Random	44.835	44.833	44.831	0.202	0.202	0.202	18.747	18.747	18.746
3.0%	(6.7E-3)	(6.4E-3)	(5.1E-3)	(7.4E-5)	(5.6E-5)	(3.4E-5)	(1.5E-3)	(1.6E-3)	(2.0E-3)

Source: the author.

4.3.3 Expressions for estimating the UHPFRC elastic properties

According to numerical tests, expressions have been proposed to correlate matrix properties (E_m, ν_m and G_m), fiber properties (E_f, ν_f and G_f), volumetric fraction (V_f), and fiber arrangement (η_θ) with composite properties E_{11}, E_{22}, E_{33}, ν_{12}, ν_{13}, ν_{23}, G_{12}, G_{13}, and G_{23}. Since $E_{11} \cong E_{22}$, $\nu_{13} \cong \nu_{23}$, and $G_{13} \cong G_{23}$, six expressions were necessary for a complete characterization of the material. They were obtained by regression in Excel spreadsheets. The fibers were generated through the orientation coefficient defined as the average of the cosines of the angle between the fibers and axis 3. Therefore, if the reference axis is different, only the rotation of the stiffness matrix is necessary.

$$E_{11} = E_m + V_f \cdot (0.3444E_f - 0.154\eta_\theta - 616.38\eta_\theta^2 + 1849.80\eta_\theta^3 - 2271.20\eta_\theta^4 + 976.49\eta_\theta^5), \quad (4.21)$$

$$E_{33} = E_m + V_f \cdot (0.0381E_f - 84.417\eta_\theta + 366.34\eta_\theta^2 + 45.059\eta_\theta^3 - 951.98\eta_\theta^4 + 816.43\eta_\theta^5), \quad (4.22)$$

$$\nu_{12} = \nu_m + V_f \cdot (0.5404\nu_f - 0.1182\eta_\theta - 2.9109\eta_\theta^2 + 10.734\eta_\theta^3 - 14.809\eta_\theta^4 + 7.1386\eta_\theta^5), \quad (4.23)$$

$$\nu_{13} = \nu_m + V_f \cdot (-0.1333\nu_f + 0.7077\eta_\theta + 0.6916\eta_\theta^2 - 9.6712\eta_\theta^3 + 17.703\eta_\theta^4 - 10.178\eta_\theta^5), \quad (4.24)$$

$$G_{12} = G_m + V_f \cdot (0.2983G_f + 3.9923\eta_\theta - 197.49\eta_\theta^2 + 558.35\eta_\theta^3 - 660.91\eta_\theta^4 + 273.13\eta_\theta^5), \quad (4.25)$$

$$G_{13} = G_m + V_f \cdot (6.2902\eta_\theta - 294.8\eta_\theta^2 - 1051.9\eta_\theta^3 + 1422.8\eta_\theta^4 - 672.22\eta_\theta^5). \quad (4.26)$$

Three expressions are sufficient for defining the composite stiffness matrix for fibers randomly distributed, since $E_{11} \cong E_{22} \cong E_{33}$, $\nu_{12} \cong \nu_{13} \cong \nu_{23}$, and $G_{12} \cong G_{13} \cong G_{23}$. Therefore, simplified expressions can be used:

$$E_{11} = E_m + 0.14E_fV_f \quad (4.27)$$

$$\nu_{12} = \nu_m + 0.21\nu_fV_f \quad (4.28)$$

$$G_{12} = G_m + 0.19G_fV_f \quad (4.29)$$

Figure 44 shows the E_{33} variation with volumetric fraction and fiber arrangement. The expressions represent the numerical results well ($R^2 \approx 1$). A similar behavior was observed for the other constants. It is also noted that the curve obtained for randomly generated fibers coincides with that obtained for $\eta_\theta = 0.5$.

Figure 44 – Variation in E_{33} with fiber content and orientation

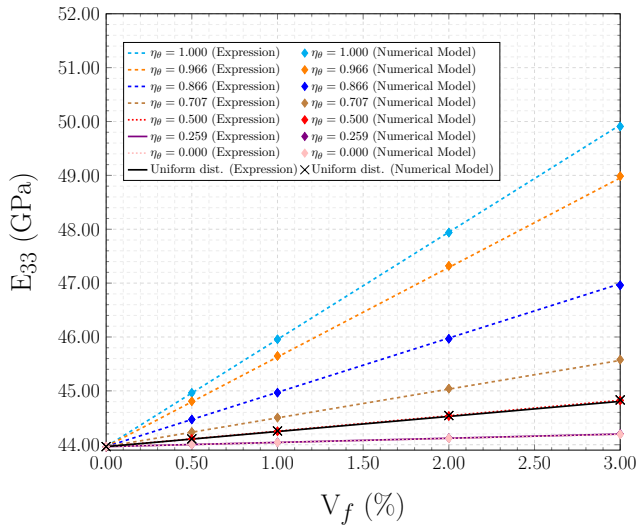

Source: the author.

4.3.4 Modification in the rule mixture

Alternatively, the rule of mixtures enables the determining the upper and lower limits elastic modulus of a composite by Voigt and Reuss models, respectively [73]:

$$E = E_f V_f + E_m(1 - V_f), \tag{4.30}$$

$$\frac{1}{E} = \frac{V_f}{E_f} + \frac{(1 - V_f)}{E_m}. \tag{4.31}$$

Hyer [74] proposed the application of those models for determining the elastic modulus of a composite with fibers perfectly aligned in one direction. As an example, assuming fibers are oriented in direction 3, E_{33} and E_{11} are determined, respectively, by Voigt and Reuss models. Figure 45 shows the results of E_{33} and E_{11} obtained by the classic models and in the expressions of the present research. The results were close; however, the theoretical limits imposed by the classical models were violated. The explanations for such behavior are: (1) the classic models do not consider the arrangement of phases and, consequently, do not take into account the orthotropic behavior of the material; (2) the classic models do not consider the Poisson's ratios of the matrix and fibers are different; and (3) according to Mobasher [66], the elastic module perpendicular to the fibers is much lower than the value normalized by the rule of mixtures because the fiber dominates the longitudinal elastic module and the matrix dominates the transversal elastic module. Therefore, using the "rule of mixtures" to determine the elastic constants of the material is an approximation, since it considers only the volume of the phases and not their arrangement.

Figure 45 – Elastic modulus obtained by classic models and in this research

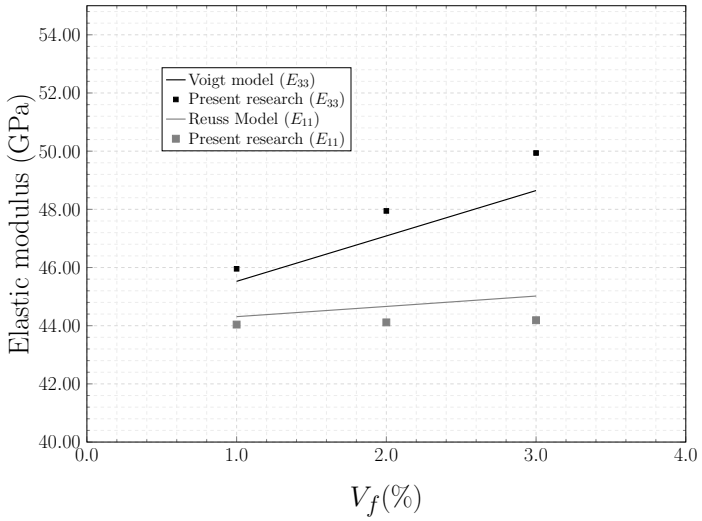

Source: the author.

A modification in the rule of mixtures based on Cox [75] accounts for the fiber orientation through efficiency factor η_1.

$$E = \eta_1 \cdot E_f \cdot V_f + E_m \cdot (1 - V_f) \tag{4.32}$$

Figure 46 presents the resulted E_{33} from homogenization against fiber content V_f for all investigated orientation coefficients η_θ using the modified rule of the mixtures.

Figure 46 – Calibration of the modified rule of the mixtures

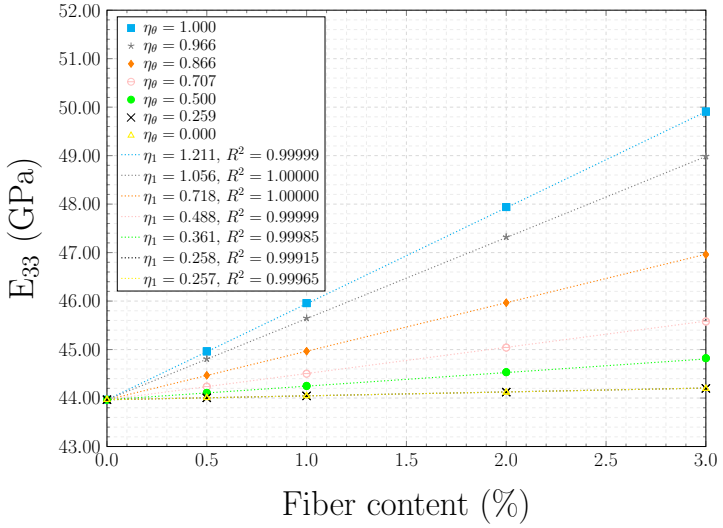

Source: the author.

The increase E_{33} was linear with fiber content as suggested by Cox [75] and the efficiency increases with preferable orientation resulting in higher modulus of elasticity,

even for low fiber contents, but more significantly when the V_f was the highest (3%). Fitting the linear functions to eq. (4.32) determines efficient factor η_1. The results are plotted against orientation coefficient η_θ in fig. 47.

Figure 47 – Efficiency factor (η_1) versus orientation coefficient (η_θ)

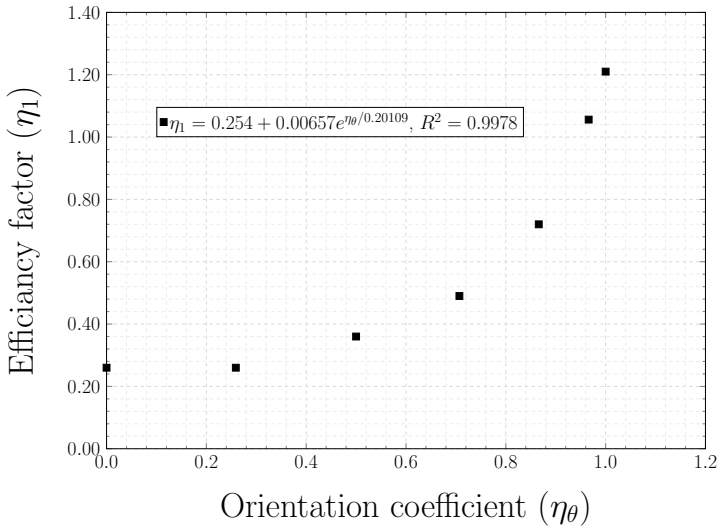

Source: the author.

It can be seen in figure that after passing η_θ of 0.25 the increase in fiber efficiency became exponential, and, when $\eta_\theta = 1$, the efficiency exceeded the value of one ($\eta_1 = 1.21$), i.e., the fiber contribution to modulus of elasticity was 20% higher than that predicted by the rule of mixtures.

4.4 Validation

The expressions proposed in item 4.3.3 were validated with numerical and experimental results from the literature.

4.4.1 Experimental/numerical study by Qsymah et al. (2017)

Qsymah et al. [69] developed a two-scale analytical-numerical homogenization approach to predict effective elastic properties of UHPFRC. The authors determined the sample orientation coefficient using a micro X-ray computed tomography image (see fig. 48) and the results indicated the fibers were preferably aligned along 1-axis with a 0.68 orientation coefficient. After a homogenization step of the mortar, $E_m = 57.3GPa$ and $\nu_m = 0.207$ were adopted. In the second step, the matrix-fiber composite was homogenized and the fiber volume fraction was 3.75%. The results obtained by Qsymah et al. [69] and those from the present research are listed in table 13.

Figure 48 – Segmented 3D μXCT image of steel fibers

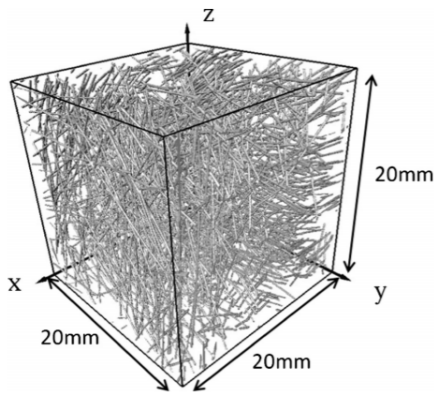

Source: Qsymah et al. [69].

Table 13 – Results by Qsymah et al. [69] and expressions of the present study ($\eta_\theta = 0.68$)

Authors	E_{11}	E_{22}	E_{33}	ν_{12}	ν_{13}	ν_{23}	G_{12}	G_{13}	G_{23}
[69]	58.97GPa	58.10GPa	57.72GPa	0.210	0.209	0.208	24.29GPa	24.10GPa	24.04GPa
Present	59.14GPa	58.12GPa	58.12GPa	0.208	0.208	0.206	24.35GPa	24.35GPa	24.05GPa
Difference	0.29%	0.03%	0.69%	0.95%	0.48%	0.96%	0.25%	1.04%	0.04%

Source: the author.

Qsymah et al. [69] also obtained values of elastic modulus considering fibers aligned along direction 1 ($\eta_\theta = 1$) and a 10% volumetric fraction. The average values of the engineering constants obtained by the computational homogenization in [69] were compared with those obtained by the expressions proposed in this research (see table 14).

Table 14 – Results from Qsymah et al. [69] and expressions of the present study ($\eta_\theta = 1$)

Authors	E_{11}	E_{22}	E_{33}
[69]	75.77GPa	56.57GPa	56.56GPa
Present	77.21GPa	58.04GPa	58.04GPa
Difference	1.90%	2.60%	2.62%

Source: the author.

4.4.2 Experimental uniaxial compression test

The elastic module can be obtained through the stress-strain curve resulting from the uniaxial compression test. Values from [2, 4, 76, 77, 78, 79, 80, 81, 82, 83, 84, 85, 86, 87] were compared with those obtained by eq. (4.22) considering the orientation limits ($\eta_\theta = 0$ and $\eta_\theta = 1$). In general, the experimental values were within the range calculated by eq. (4.22). Figure 49 shows fibers aligned with the loading direction ($\eta_\theta = 1$) overestimate the elastic module. In contrast, those in the plane perpendicular to loading direction $\eta_\theta = 0$ underestimate the elastic module. For a more accurate analysis, the orientation of the fibers can be obtained experimentally, as discussed in the previous item.

Figure 49 – Relationship between predicted and experimental values of elastic modulus

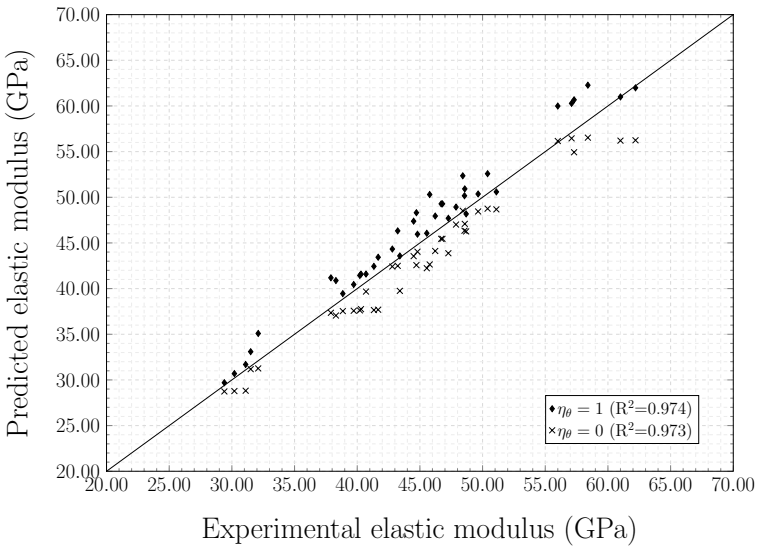

Source: the author.

4.4.3 Prediction of the elastic modulus of prisms tested in the previous chapter

Equation 4.22 estimated the elastic modulus of UHPFRC prisms presented in the previous chapter. The input data are elastic modulus of the matrix, obtained by an impact acoustic test, orientation coefficient, obtained by image analysis, fiber content, determined in the dosage of the material, and fiber elastic module, provided by the manufacturer.

Table 15 shows the elastic modulus values predicted by the expression and experimentally obtained by the impact acoustic test. Reuss and Voigt models checked whether they were within the maximum and minimum limits suggested by the rule of mixtures, which was confirmed. The most significant difference between the results was 5.7%. The experimental results were superior to those estimated in the samples with 2% of fiber content. In the experimental sample, other factors, such as concrete exudation, may interfere with the modulus of elasticity. However, in general, the estimates were reasonable, confirming the potential of the expression in predicting the elastic modulus.

Table 15 – Prediction of the elastic modulus of the prisms tested in the previous chapter

Sample	V_f (%)	η_θ	$E_{exp.}$ (GPa)	$E_{pred.}$ (GPa)	Error (%)	E_{Voigt} (GPa)	E_{Reuss} (GPa)
P0%	0	-	45.48	45.48	0	45.48	45.48
P1%M1	1	0.797	45.55	46.22	1.48	47.03	45.83
P1%M2	1	0.746	46.01	46.09	0.17	47.03	45.83
P1%M3	1	0.680	46.19	45.97	0.48	47.03	45.83
P2%M1	2	0.810	48.78	47.05	3.55	48.57	46.19
P2%M2	2	0.753	48.16	46.73	2.97	48.57	46.19
P2%M3	2	0.699	49.32	46.52	5.68	48.57	46.19

Source: the author.

4.4.4 Simulation of compression test

A compression test simulated on a cylindrical sample of 50 mm diameter and 100 mm length with discrete fibers evaluated the elastic modulus for further validation. The mesh was comprised of 5 mm C3D8R elements and a fiber content of 2% was considered. A 0.3 *mm* displacement was applied to one side of the cylinder, whereas a boundary condition was applied on the other side, restricting its displacement. Figure 50 displays the stress-strain curve for different orientation coefficients evaluated. Note the elastic modulus is reduced as the value of η_θ is reduced. The results were obtained after applying a 0.3 mm displacement. The stress value was calculated from the support reaction force.

Figure 50 – Stress-strain curve as a function of orientation coefficient

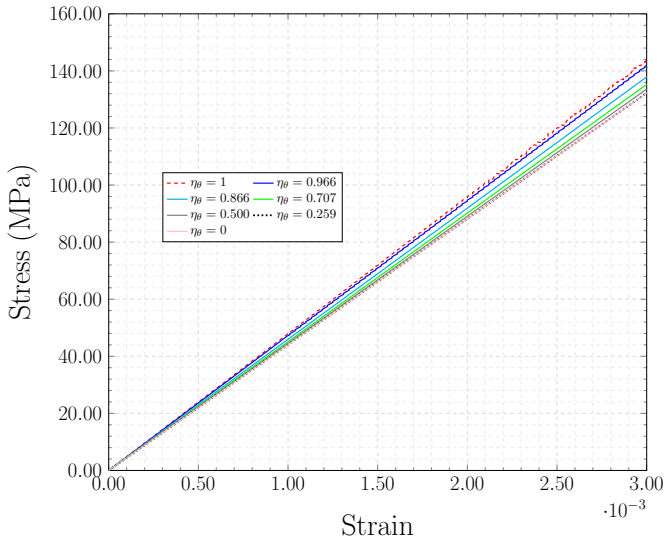

Source: the author.

Figure 51 shows the stress in the concrete and fibers for some of the evaluated orientation coefficients. As expected, fibers are activated and contribute more substantially to the stiffness in the loading direction when aligned with that direction. The values of

elastic modulus obtained by the stress-strain curve were compared with those provided by eq. (4.22) (see fig. 52). The results showed a good agreement.

Figure 51 – Stress in concrete and fibers

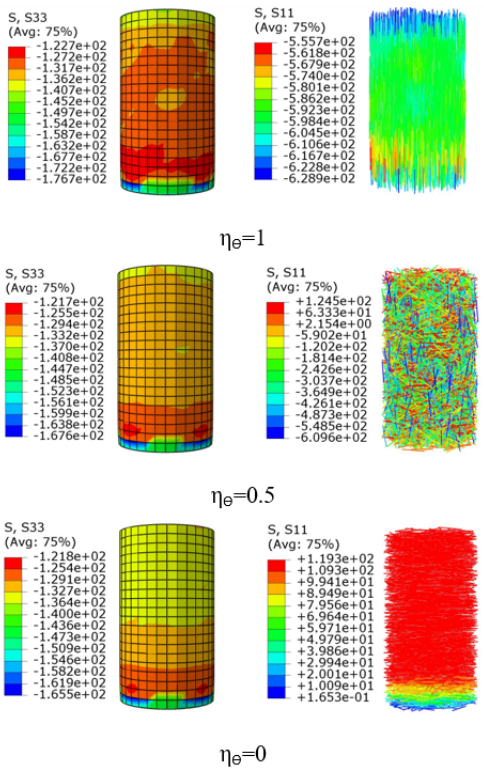

Source: the author.

Figure 52 – Elastic modulus obtained by the numerical compression test and eq. (4.22).

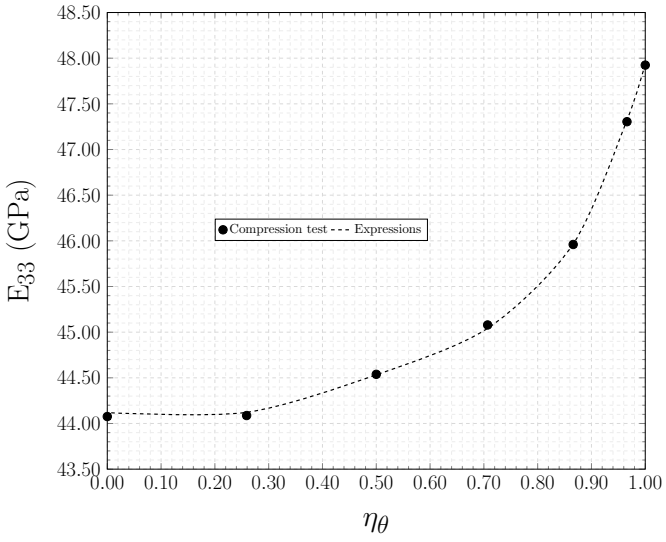

Source: the author.

4.5 Conclusions

This chapter provided expressions for determining the effective elastic properties of UHPFRC as a function of phase properties, volume fractions, and fiber arrangements. According to the results and discussions, the following conclusions have been drawn:

- The influence of RVE size and mesh on the value of the effective properties was analyzed, revealing a small one on the results.
- Expressions for determining the effective properties of UHPFRC have been proposed. The expressions were validated with experimental and numerical results from the literature.
- An evaluation of the existence of isotropy plans in the material revealed the adoption of isotropic material for fibers distributed in volume and transversal isotropic for fibers distributed on the 1-2 plane and aligned with a direction is an adequate consideration.
- The application of the classical Voigt and Reuss models for determining the elastic modulus of the composite was evaluated. Although the results were close to those from the expressions developed in this study, the limits were violated, since classical models do not consider the geometric arrangement of the phases, represented in this research by the orientation coefficient.

The results and discussions have advanced the understanding of the correlation between fiber content and orientation and the elastic constants that define the mechanical behavior of the material.

FIVE

MICROMECHANICS-BASED CONSTITUTIVE MODELING FOR UHPFRC

This chapter presents a micromechanical-based model for UHPFRC tensile behavior involving fiber pullout, fiber content and orientation in the composite, and group effect. The group effect was considered in the constitutive model through parameters ξ and $\bar{\beta}$ capable of considering the reduction of the bond strength and the change in the shape of the composite post-cracking curve due to the iteration between the fibers. The fiber spacing decreases as the fiber content increases, and the interaction between them cannot be neglected. If the group effect is not considered, the material response is overestimated. ξ and $\bar{\beta}$, dependent on fiber content and orientation, were calibrated by the finite element model updating using Genetic Algorithms (GA). Heterogeneous models developed compared the results. Several numerical simulations enabled the obtaining of a constitutive model representing the UHPFRC tensile behavior and provided guidelines for the material simulation. The numerical results showed excellent agreement with the experimental ones from the literature and a parametric analysis revealed interfacial parameters and fiber content and orientation significantly influence the UHPFRC response.

5.1 Background

In general, fibers allow the composite to resist tensile stress after cracking, increasing toughness since they resist and mitigate crack propagation [37, 49, 5]. As the fiber efficiency depends on their orientation and the prediction of material behavior is necessary for design, several researchers have studied the composite uniaxial tensile response analytically. Li, Stang, Krenchel [88] proposed a theoretical model based on micromechanics that captures the essential characteristics of stress-crack opening relationships for concretes reinforced with two types of fibers, namely steel and polypropylene. Li [49] introduced slip-hardening parameter $\bar{\beta}$ in the model applied in a study on ECC with PVA (Polyvinyl Alcohol Fiber)

fibers randomly distributed. The author highlighted the importance of an integrated approach that associates material microstructure and deformation mechanisms with structure performance. Lei et al. [89] analyzed Li's model application in concrete reinforced with Polyethylene (PE) fibers and reported $\bar{\beta}$ increased by increasing fiber inclination angle for UHS-UHDCC (ultra-high strength and ultra-high ductility cementitious composites). Abrishambaf, Pimentel, and Nunes [10] adopted the model proposed by Li, Stang, Krenchel [88] to predict the uniaxial tensile behavior of UHPFRC with steel fibers.

In the experimental field, Duque and Graybeal [3] discussed the fiber orientation effect on the UHPFRC tensile response. According to the authors, the results suggest a strong influence on both post-cracking strength and first cracking stress by fiber distribution during casting. The samples inclined 90 degrees with the flow direction (F90) and 45 degrees with the flow direction (F45) presented a reduction in average first cracking stress and the average multi-cracking stress over 50% and 40%, respectively, in relation to the samples aligned to the flow direction (F0). The study indicated a need for more research towards a better understanding and quantification of the impact preferential fiber alignments may exert on a material's mechanical behavior. Bastien-Masse, Denarié, and Brühwiler [31] evaluated the relation of UHPFRC behavior with the geometry and fabrication method of the specimens. Different casting methods and types of specimens were used and the authors concluded tensile response depends strongly on fiber orientation and varies in fucntion of specimen geometry and casting. Kang and Kim [5] studied fiber orientation in the UHPFRC tensile behavior and concluded such a factor was significant in maximum cracking strength and post-cracking range. The average maximum tensile stress was 16.05 MPa for PL (placement parallel to the tensile direction) specimens and 11.80 MPa for TL (placing concrete transversely to the tensile direction) specimens. French standard [90] has already shown fiber orientation must be considere in the design of UHPFRC structures and has introduced an orientation factor K, determined by inverse analysis from a bending test in determining the composite tensile behavior. The concern of these researches regarding the fiber orientation shows the importance of considering this parameter in UHPFRC structures.

A numerical simulation that effectively considers fiber orientation is fundamental for the design of UHPFRC structures. According to Bentur and Mindess [37], the distribution of fibers is rarely completely uniform and their orientation is not ideally random, which will give rise to anisotropic behavior. The material model can consider such anisotropy through either a heterogeneous model (two-phase model), or a homogeneous one (single-phase model). The disadvantage of heterogeneous models is the high computational cost, which hampers their application in real projects. On the other hand, few studies have focused on the development and application of homogeneous constitutive models accounting for fiber orientation that reasonably represent UHPFRC. According to Kang and Kim [5], a systematic approach from an individual fiber interfacial behavior to a composite or

structural performance has been rarely adopted. Such an integrated approach enables the optimal structural use of particular composite classes like UHPFRC.

Another phenomenon not deeply explored and that should be included in the constitutive model is group effect. As the fibers content increases, the spacing between them decreases. If the group effect is neglected, the material response is overestimated. Some recent studies have discussed the influence of group effect on the average bond strength [35, 21, 49, 34, 91]. Huo et al. [35] evaluated it in steel fiber reinforced concrete (SFRC) and reported the SFRC strength increases almost linearly with the fiber volume fraction when the fiber content is small. However, the rate of strength increase reduces at a highest fiber content, i.e., multiple fibers provide less strength than the linear superposition of the single fiber pullout strength. Zhou and Qiao [21] studied the UHPFRC tensile behavior and pointed out the fiber reinforcement efficiency decreases with the fiber volumetric fraction due to the group effect, thus highlighting the importance of complementary studies for the development of more accurate models. Li [49] claimed in practice, interfacial parameter τ decreases as the fiber content increases. By applying the model to PVA-ECC, Li adopted $\tau = 1.91MPa$ for 0.5% of fiber content and $\tau = 1.31MPa$ for 2% of fiber content, which is a 31% reduction. Kim and Yoo [34] and Yoo, Kim, and Park [91] performed a fiber pullout test with a single fiber and multiple fibers. The average bond strengths were approximately 30% lower for specimens with multiple aligned fibers with 1%, 2%, and 7% of fiber content than those with a single aligned fiber, and the average bond strength of bundled fiber specimens decreased 52%, indicating the group effect is still being uncovering for UHPFRC.

This study proposes a micromechanics-based constitutive model for UHPFRC tensile behavior. According to the statistical theory, micromechanical properties are coupled with macroscopic tensile properties, determining the stress-crack opening curves. The group effect was included in the model through the introduction of parameter ξ, which varies from 0 to 1 and weights the bond strength. Interfacial parameter $\bar{\beta}$ from Li's model varied with the fiber content for PVA-ECC [49]. Therefore, in the presente study, ξ and $\bar{\beta}$ were calibrated according to experimental results from the literature and by the finite element model updating using Genetic Algorithms (GA). The homogeneous model was validated through a comparison of the uniaxial tensile test with experimental results from the literature and those from heterogeneous modeling.

5.2 Constitutive models

This section presents the constitutive model used in the numerical models developed in this research.

5.2.1 Tensile behavior

UHPC has high compressive and tensile strengths with very brittle failure in the absence of fibers. The addition of such reinforcement produces a significant gain in ductility and energy absorption capacity [92, 84, 2], leading to a strain hardening behavior. According to Thai, Nguyen, and Nguyen [93], fibers retain macro cracking formation speed, redistributing tensile stresses and typically forming multiple cracks that improve ductility and toughness. The improved properties contribute to structure performance, providing safety, increasing service life, and lowering maintenance costs. Therefore, the study of the UHPFRC tensile behavior and the development of a reliable tensile model that considers the effects of fibers are fundamental for supporting a further design of structural design standards [92, 15].

Redistribution capacity depends on fiber surface roughness, fiber length, matrix composition, and fiber distribution and orientation [93, 23, 2]. Figure 53 illustrates typical tensile stress-crack opening diagrams. A post-cracking behavior can be either hardening, or softening, depending on the amount and orientation of fibers and interface properties [84].

Figure 53 – Typical tensile stress - crack opening curve

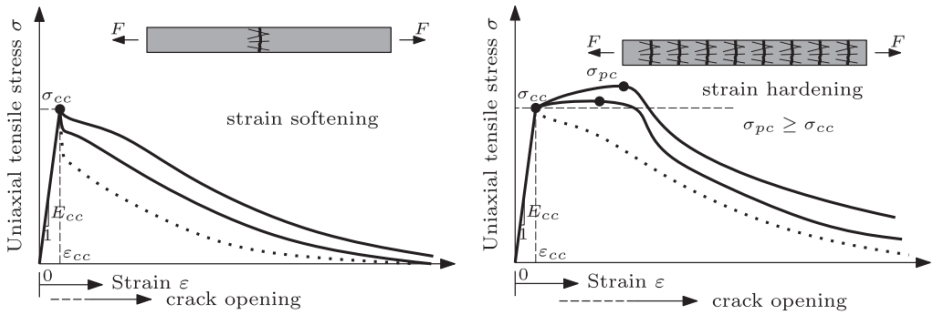

Source: Wille, El-Tawil and Naaman [84].

5.2.2 Homogeneous (one-phase) material model

Most UHPFRC finite element models simulate a cement matrix and steel fibers as a one-phase material, which considers fibers randomly distributed in the matrix. Moreover, stress-crack opening or stress-strain models are, in most cases, empirical or semi-empirical, with no phenomenological base. The composite is represented by an isotropic model

[62, 94, 2]. However, the mechanical properties of UHPFRC are strongly influenced by fiber orientation relative to tensile loading. The actual fiber orientation is influenced by several factors, such as fiber characteristics, fresh-state flowability, pouring method, and mould shape [95]. The consideration of preferential orientation of steel fibers in the tensile load direction may result in an overestimation of post-cracking mechanical properties compared to specimens with an equal amount of fibers, but a random fiber orientation [13]. Therefore, a realistic fiber orientation must be considered when composites like UHPFRC are modeled.

In this study, the stress-crack opening curve was obtained according to micromechanical models and used as an input in the Concrete Damaged Plasticity (CDP) model available in Abaqus finite element software. CDP, which is based on the model proposed by Lubliner et al. [96] and Lee and Fenves [97], couples the plasticity theory to damage mechanics, considering the irreversible processes due to damage and plasticity.

5.2.2.1 Micromechanical models

According to the proposal of Li, Stang, and Krenchel [88], the tensile stress-crack opening response, $\sigma_u(w)$, is determined as the summation of the contributions of the matrix, $\sigma_{mt}(w)$, fiber pre-stress, $\sigma_{pre}(w)$, and fiber debonding and pullout (fiber bridging), $\sigma_f(w)$, as shown in eq. (5.1). Figure 54 displays the contribution of each term of eq. (5.1). After cracking, the contribution of fibers becomes highly significant, leading to a hardening behavior. During cracking, the tensile stress drops suddenly in the matrix, while the stress increases in fibers due to bridging.

$$\sigma_u(w) = \sigma_{mt}(w) + \sigma_{pre}(w) + \sigma_f(w) \tag{5.1}$$

Figure 54 – Tensile response

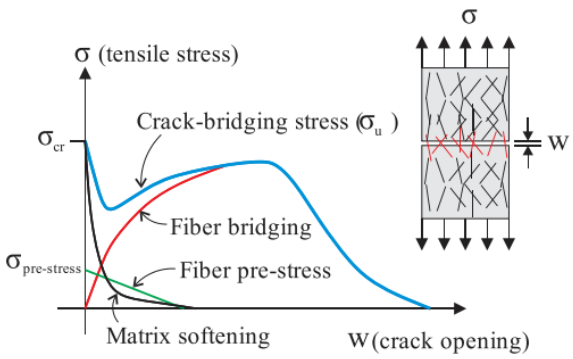

Source: the author.

5.2.2.2 Matrix softening and fiber pre-stress

The contribution of the matrix and fiber pre-stress were adopted, according to Abrishambaf, Pimentel, and Nunes [10] and the following exponential law was adopted for the softening regime of the matrix:

$$\sigma_{mt}/f_{mt} = \exp(-f_{mt}w/G_{Fm}), \tag{5.2}$$

where G_{Fm} is matrix fracture energy and f_{mt} is matrix cracking strength. The fiber pre-stress is obtained by

$$\sigma_{pre}/f_{mt} = \gamma(w_{deb} - w)/w_{deb} \geq 0. \tag{5.3}$$

γ varies between 0.05 and 0.17 for UHPFRC with fiber volume fractions between 0.02 and 0.04, 40 to 55 GPa matrix modulus of elasticity (E_m), and 200 to 210 GPa steel fibers modulus of elasticity (E_f). $w_{deb} = (\tau l_f^2)/(E_f d_f)$ is the crack whose value marks the onset of the pullout stage, where τ is interfacial bond strength, l_f is fiber length, and d_f is fiber diameter.

5.2.2.3 Fiber debonding and pullout

The model must consider the contribution of all fibers that cross the cracking plane. Therefore, the total fiber bridging stress can be approximated by [88]:

$$\sigma_f(w) = \frac{V_f}{A_f} \int_{\theta_0}^{\theta_1} \int_{z=0}^{(L_f/2)\cos(\theta)} P(w, l_e) g(\theta) p(\theta) p(z) dz d\theta, \tag{5.4}$$

where $P(w, l_e)$ is a function for the load carried by a single fiber of normal alignment to the crack plane and embedment length l_e, $p(\theta)$ captures randomness in the fiber inclination, $p(z)$ considers randomness in the fiber centroidal location to the crack face, and z is the distance between the fiber centroid and the crack plane (z varies between 0 and $l_f/2$, resulting in $p(z) = 2/l_f$), see fig. 55. The integration limits between θ_0 and θ_1 reflect the fiber inclination angle range. Inclined fiber bridging force $P(\theta)$ is correlated to the straight pullout $P(w, l_e)$ via term $g(\theta)$, i.e., $P(\theta) = P(w, le)g(\theta)$.

Figure 55 – Inclined fibers, showing centroidal distance z and inclination angle θ. Fibers with $z \geq (l_f/2)\cos\theta$ will not be counted as bridging fibers

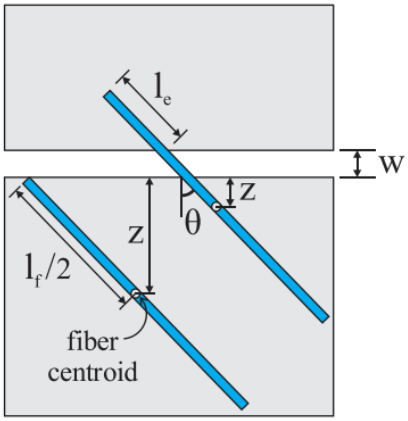

Source: adapted from Li [49].

Single fiber straight pullout model $P(w, l_e)$

Li [49] proposed a theoretical equation for aligned single fiber pullout load $P(w, l_e)$. The analytical expression adapted for UHPFRC is shown in eqs. 5.5 and 5.6. The first expression refers to the fiber tensile load in the debonding stage. When fiber exit point displacement u reaches the value u_0, the load reaches its peak. After the peak, the fiber pullout is initiated and represented by the second expression.

$$P(u) = \pi\sqrt{\frac{E_f d_f^3(1+\eta)\xi\tau u}{2}}, \quad u \leq u_0 \tag{5.5}$$

where $u_0 = \dfrac{2\xi\tau l_e^2}{E_f d_f(1+\eta)}$.

$$P(u) = \pi d_f \xi\tau(l_e - (u-u_0))\left(1 + \bar{\beta}\frac{u-u_0}{d_f}\right), \quad u > u_0 \tag{5.6}$$

where $\eta = (V_f E_f)/[(1-Vf)E_m]$, $\tau = P/(\pi d_f l_e)$, and $\bar{\beta}$ is an interfacial parameter. Parameter ξ was introduced so that the group effect could be considered. It is due to the fiber spacing decreases as the fiber content increases, and the interaction between them cannot be neglected. If the group effect is ignored in the constitutive model, the fibers contribution is overestimated for high fiber contents [35]. The group effect reduces fiber-matrix bond strength τ, therefore, ξ varies between 0 and 1 to account for this reduction.

Average bond strength τ

Fiber-matrix average bond strength τ was obtained through the pullout test developed by Abrishambaf, Pimentel, and Nunes [10]. The value adopted was 5.11 MPa, representing the bond strength with embedded length $l_e = l_f/4$ and 0^o inclination angle. A

uniformly distributed embedded length in the 0 and $l_f/2$ range is usually assumed, leading to $p(l_e) = 2/l_f$, with $l_f/4$ mean value [10, 4, 51].

Function $g(\theta)$

The tests conducted by Abrishambaf, Pimentel, and Nunes [10] were used for calibrating function $g(\theta)$, eq. (5.7), which usually characterizes phenomena such as snubbing effect (coefficient f) and spalling (coefficient k) of the matrix. Figure 56 shows the fit between experimental results and equation for $f = 2$ and $k = 2$.

$$g(\theta) = e^{f\theta}\cos(\theta)^k \tag{5.7}$$

Figure 56 – Function $g(\theta)$ defined according to experimental results of Abrishambaf, Pimentel, and Nunes [10]

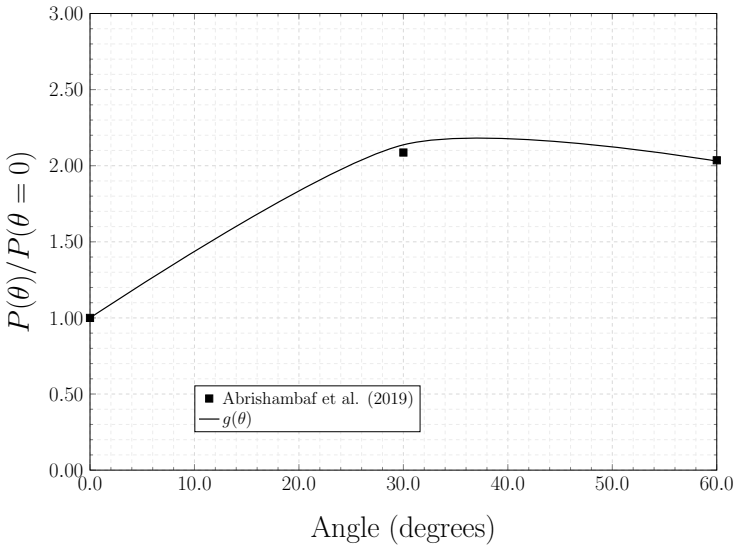

Source: the author.

Function $p(\theta)$

The fiber orientation distribution adopted was based on the normal distribution function and the function presented in eq. (5.8) was considerd, as in Fu and Lauke [98]. p and q must be calibrated in funtion of mean angle (θ_{mean}) and standard deviation (σ_θ) from the fiber orientation distribution obtained from experimental samples.

$$p(\theta) = \frac{(\sin\theta)^{2p-1}(\cos\theta)^{2q-1}}{\int_0^{\pi/2}(\sin\theta)^{2p-1}(\cos\theta)^{2q-1}d\theta} \tag{5.8}$$

Fiber bridging stress-crack opening curve

The integral of eq. (5.4) was solved and, neglecting higher-order terms, the following expressions were obtained for the calculation of the fiber bridging stress between crack faces:

$$\sigma_f(\bar{w}) = \frac{V_f l_f \xi \tau}{2d_f}\left[4\left(\frac{\bar{w}}{\bar{w}^*}\right)^{1/2} - 2\left(\frac{\bar{w}}{\bar{w}^*}\right)\right]\int_0^{\pi/2} p(\theta)g(\theta)cos(\theta)d\theta, \bar{w} \leq \bar{w}^* \tag{5.9}$$

$$\sigma_f(\bar{w}) = \frac{V_f l_f \xi \tau}{2d_f}\left[2(1-\bar{w})^2 + \frac{\bar{\beta} L_f}{d_f}(1-\bar{w})(\bar{w}-\bar{w}^2)\right]\int_0^{\pi/2} p(\theta)g(\theta)cos(\theta)d\theta, \bar{w} \geq \bar{w}^* \tag{5.10}$$

where $\bar{w}^* = \dfrac{2\xi\tau l_f}{E_f d_f(1+\eta)}$ and $\bar{w} = \dfrac{w}{l_f/2}$.

Table 16 shows some results of $\int_0^{\pi/2} p(\theta)g(\theta)cos(\theta)d\theta$, which represents the fiber efficiency in delaying cracks propagation. Note the integral values are greater around $\theta_{mean} = 30^o$, which is in agreement with Huo et al. [35].

Table 16 – Results of $\int_0^{\pi/2} p(\theta)g(\theta)cos(\theta)d\theta$

η_θ	θ_{mean}	$\int_0^{\pi/2} p(\theta)g(\theta)cos(\theta)d\theta$
1	0^o	1.00
0.966	15^o	1.52
0.866	30^o	1.73
0.707	45^o	1.38
0.500	60^o	0.94
0.259	75^o	0.48
0	90^o	0

Source: the author.

Genetic Algorithms

ξ and $\bar{\beta}$ were calibrated automatically by a Genetic Algorithm (GA) code implemented in the finite element model script. The objective function determines the purpose of the problem which, in this study, is defined by eq. (5.11), i.e., by calibrating variables ξ and $\bar{\beta}$, the objective is to approximate experimental and numerical stresses referring to the first crack ($\sigma_{cracking}$) and the last point of the test ($\sigma_{residual}$). Therefore, the objective function represents an error between numerical and experimental models. The mutation occurred at a much lower rate (0.1 probability) in comprison to crossover (0.9 probability) for preventing the process from becoming random. Finally, the finite element models were

simulated with the new population. The loop is repeated until the stopping criterion has been reached, i.e., maximum number of 100 generations. Each generation consisted of 25 individuals and the elitism technique preserved the three best individuals in the population.

$$min[(\sigma_{cracking,num} - \sigma_{cracking,exp})^2 + (\sigma_{residual,num} - \sigma_{residual,exp})^2] \tag{5.11}$$

The material was defined by CDP constitutive model and the model proposed by Chi et al. [99] was considered for compression behavior. The plasticity parameters of CDP were adopted according to Krahl, Carrazedo, and El Debs [2] and the micromechanical model based on Li [49], eq. (5.9) and eq. (5.10) was adopted for the stress-crack opening tensile curve.

5.2.3 Heterogeneous (two-phase) material model

Fiber-reinforced concrete can be considered a two-phase material composed of a matrix and discrete steel fibers [4, 63, 51, 100, 13]. The interfacial behavior is accounted for in the fiber constitutive model, employing an equivalent stress-strain law based on the fiber pullout behavior.

Fibers are generated through a Python script and incorporated in the solid model developed in Abaqus (see chapter 4) so that the truss-element fibers are embedded (constrained) in a three-dimensional mesh of solid finite elements, representing a cement matrix. CDP represents a brittle matrix behavior. The fibers must be modeled as truss elements constrained to the matrix as embedment reinforcements, i.e., as partially incorporated elements, so that the stresses are constant along their length. The load versus slip curves obtained in the pullout tests are converted to an equivalent stress-strain behavior through equations eqs. 5.12 and 5.13 [100].

$$\sigma_f = \frac{F}{A_f}, \tag{5.12}$$

$$\varepsilon_f = \frac{s}{l_f}, \tag{5.13}$$

where σ_f and ε_f are equivalent normal stress and strain of the fiber, respectively, F and s are coordinates of the load and slip curve of the single fiber pullout, respectively, and A_f and l_f are the area of the fiber cross-section and its total length, respectively.

The general fiber orientation in cracked sections significantly influences the single pullout response [24, 10, 63, 27]. Therefore, the equivalent stress-strain law varies according to fiber inclination angle with the cracking plane. Considering a curve for each angle would

lead to a very time-consuming model. For simplification without representativeness loss, the inclination angle can be divided into intervals, where the pullout behavior is defined. In this study, the fibers were divided into the following intervals: [0º, 15º[, [15º, 30º[, [30º, 45º[, [45º, 60º[, [60º, 75º[, and [75º, 90º[. Lee, Kang, and Kim [27] analytical model was adopted for describing the pullout of steel fibers in the UHPFRC matrix, with the same parameters used in [4].

CDP defined the matrix constitutive model. Carreira and Chu [101] proposed the curve used in compression, and Hordijk [102] proposed the one used in tension. The values of tensile and compressive strengths of the matrix were obtained experimentally by Oliveira [4].

5.3 Finite element modeling of UHPFRC

The numerical models for tensile tests were developed in commercial finite element software Abaqus [65]. Solid finite elements C3D8R were employed, an 8-node linear brick, with reduced integration and hourglass control. Figure 57 illustrates the model that simulated the dogbone shaped tensile test performed by Oliveira [4]. The other models were elaborated in a similar way, adjusting the sample dimensions. On the right side of the sample, displacements in x, y and z directions were restricted in the contact area with the steel grips, whereas a displacement in the z direction was imposed on the left, and x and y directions were restricted.

Figure 57 – Finite element model

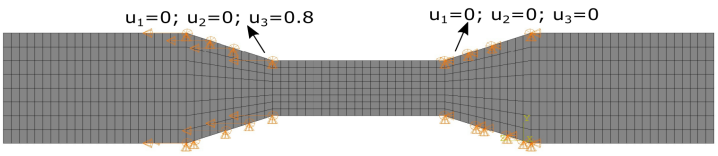

Source: the author.

Simulations were performed for three different mesh discretizations, as depicted in fig. 58. Figure 59 shows the stress-strain response for the different meshes evaluated by the one-phase model. As can be seen, the coarse mesh provided a different response, whereas the refined and median meshes showed similar ones. Therefore, the analysis continued with the median mesh due to the lower computational cost compared to the refined mesh.

Figure 58 – Evaluated meshes (a) refined (b) median(c) coarse

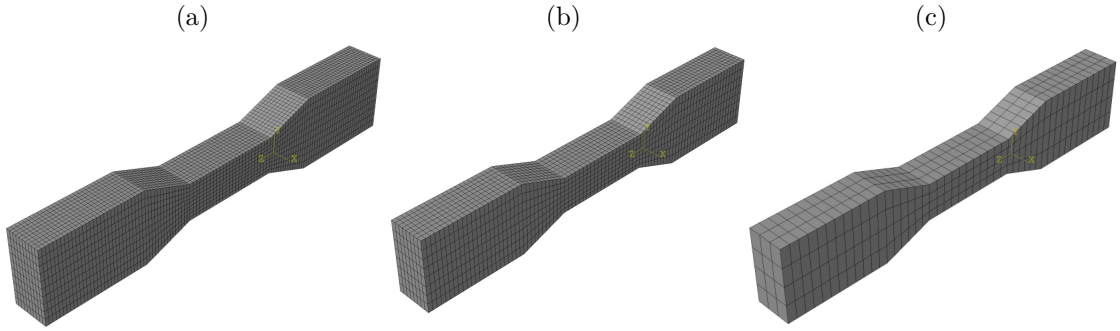

Source: the author.

Figure 59 – Mesh convergence test

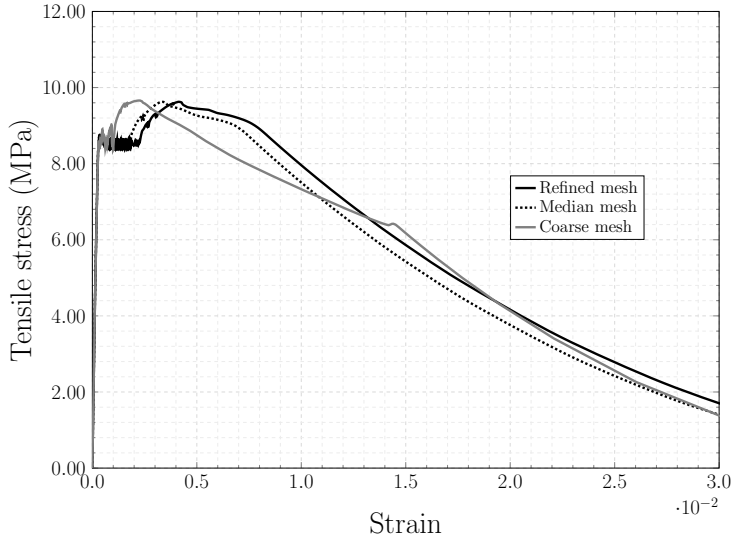

Source: the author.

5.4 Model validation

The constitutive model based on micromechanics for UHPFRC was validated against test results from the literature. Tensile tests were performed by Oliveira [4], Duque and Graybeal [3], Bastien-Masse, Denarié, and Brühwiler [31], and Shen and Brühwiler [38].

5.4.1 Homogeneous (one-phase) material model

Parameters adopted and discussion about group effect

The following parameters were adopted for all simulations: $E_f = 200GPa$, $f_{mt} = 7.4MPa$ (except for Shen and Brühwiler [38] who used 7.0 MPa), $\tau = 5.11MPa$, $G_{Fm} = 0.01N/mm$, and $\gamma = 0.17$. The other parameters are summarized in Table 17. The parameters ξ and $\bar{\beta}$ were automatically calibrated by GA according to experimental results.

Figure 60 shows the evolution of GA.

Table 17 – Experimental fiber orientation factors and related parameters

References	$V_f(\%)$	$l_f(mm)$	$d_f(mm)$	η_θ	ξ	$\bar{\beta}$
[4]	1.0	13.0	0.20	0.90	1.00	-0.07
[4]	2.0	13.0	0.20	0.90	0.85	-0.12
[3]	2.0	12.7	0.20	0.65	0.69	-0.02
[3]	2.0	12.7	0.20	0.74	0.81	-0.04
[3]	2.0	12.7	0.20	0.85	1.00	-0.08
[31]	3.0	13.0	0.16	0.72	0.42	-0.04
[31]	3.0	13.0	0.16	0.82	0.52	-0.06
[38]	3.0	13.0	0.175	0.76	0.55	-0.09

Source: the author.

Figure 60 – Evolution of GA

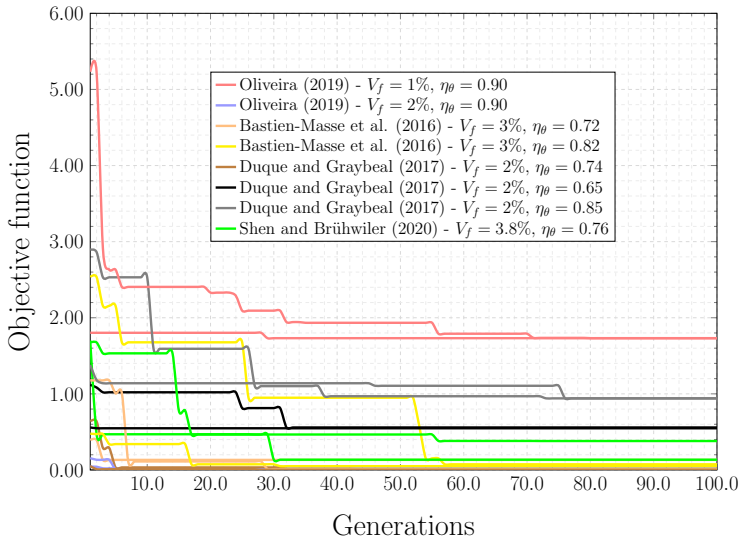

Source: the author.

The ξ parameter showed a downward trend with increasing fiber content (see Figure 61(a)). Fibers tend to carry a smaller load, i.e., the group effect is more pronounced as the fiber content increases due to a reduction in the spacing between them, which increases iteration. The experimental results of Bastien-Masse, Denarié, and Brühwiler [31] and Duque and Graybeal [3] promoted an assessement of the orientation coefficient effect on ξ for 3% and 2% of fiber volume fraction, respectively (Figure 61(b)). In both cases, a smaller orientation coefficient (more fibers inclined with the loading direction) resulted in a more significant group effect, i.e., a smaller ξ value, since inclined fibers cause

stress concentrations and spalling in the matrix at crack faces (end of fiber channel) [103], increasing interaction with neighbor fibers.

Figure 61 – Effect of fiber content and orientation coefficient on parameter ξ

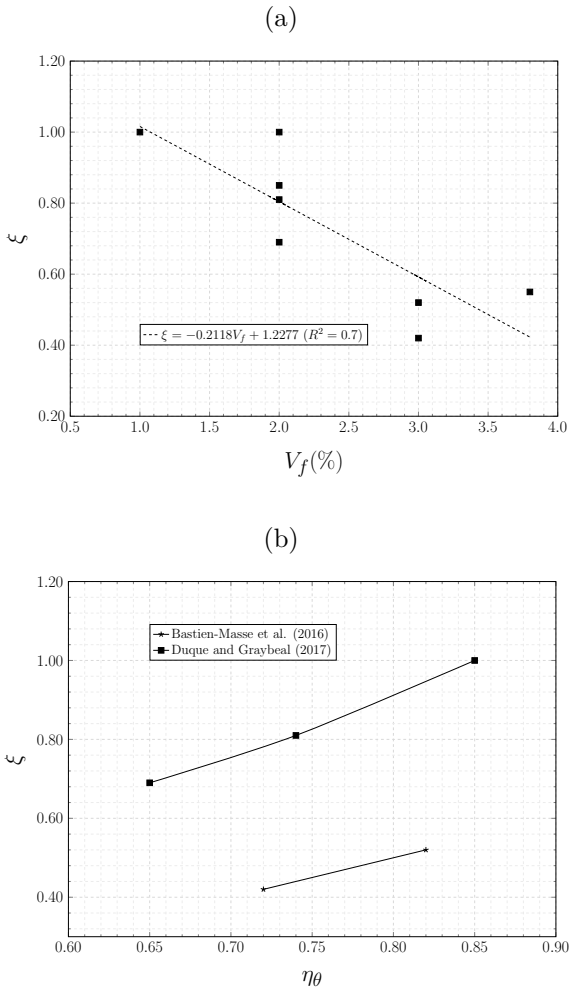

Source: the author.

Friction, which depends on normal stresses and friction coefficient, is the main resisting mechanism on UHPFRC fiber-matrix interaction. An analysis performed revealed ξ reduces the friction transferring capacity. Therefore, factors that influence that property must be considered. Shrinkage is the main phenomenon for the appearance of normal stress in rigid inclusions in concrete, as steel fibers, which is increased even more by the presence of silica fume [104]. It causes matrix contraction and the closing movement of fiber holes, promoting incompatible strains between fiber and matrix. As the fiber prevents this movement, radial confining stress arises [105], as illustrated in fig. 62.

Figure 62 – Concrete shrinkage

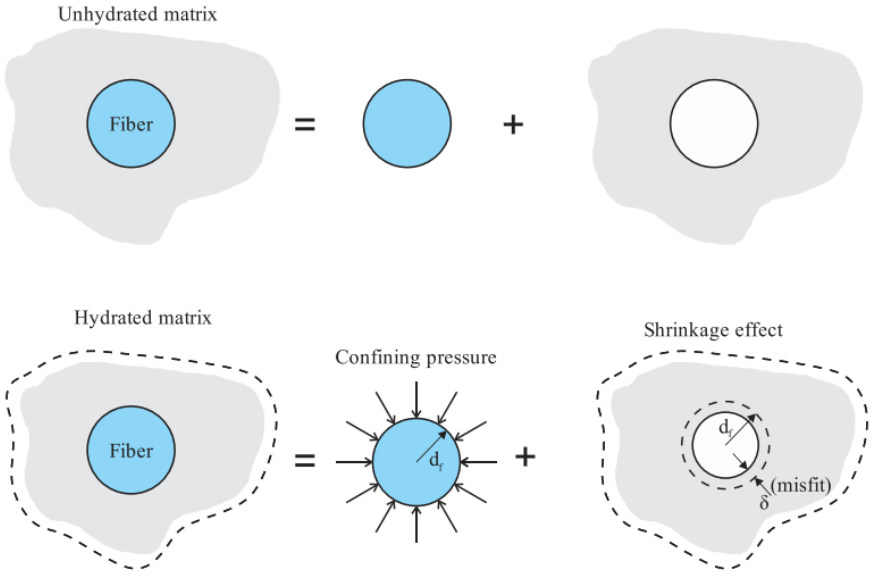

Source: the author.

Friction coefficient depends on the fiber surface roughness, which can be coated with copper [24] or nano-silica (SiO2) [106, 107], or make scratches with sandpaper [108]. The matrix surrounding fibers are dense in UHPFRC [109], mainly due to fillers and silica fume, which also influence friction.

Matrix cracking is likely to be intensified by stress states overlapping with increasing fiber content. Early shrinkage cracking probably propagates more intensely due to the group effect. Interaction between neighbor fibers significantly intensifies such stress concentrations [110], probably promoting early debonding prior to matrix cracking [111]. Such a behavior also influences ξ and is not simulated in pullout tests. Therefore, when the crack path crosses the fiber, its ends are already debonded, influencing all pullout performance. Since the stress is zero on the crack faces, it may imply a reduction in the normal stress and frictional shear stress [37].

The $\bar{\beta}$ parameter governs friction behavior during pullout, i.e., the shape of the curve after bond adhesion loss (post-debonding) (see fig. 63). Initially, it showed an increase with the fiber content increase and then a reduction, as shown in fig. 64. The result suggests the addition of the fiber volume fraction improves the post-debonding behavior up to approximately 2% of fiber content, after which fiber efficiency is reduced due to a greater interaction between them, i.e., multiple fibers provide less strength than the linear superposition of the single fiber strength. $\bar{\beta}$ is increased with the fiber inclination, which is in agreement with Lei et al. [89]. Friction increases are due to force inclination in relation to fiber because of the snubbing effect [103]. This inclination makes a component of the pullout force act towards the interface and generates more friction stress at the interface, justifying the $\bar{\beta}$ increase with the fiber inclination in the range analyzed. More

results are necessary towards more assertive conclusions.

Figure 63 – $\bar{\beta}$ parameter

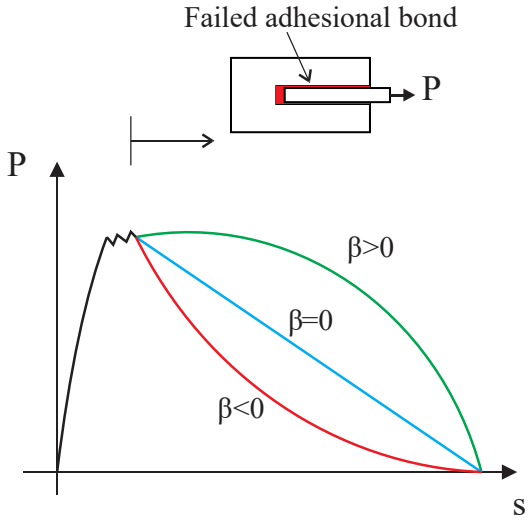

Source: the author.

Figure 64 – Effect of fiber content and orientation coefficient on parameter $\bar{\beta}$

(a)

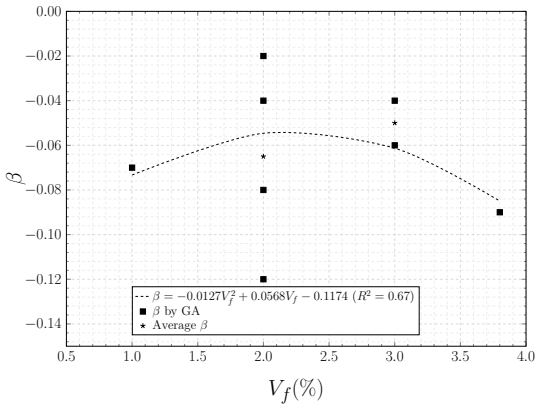

(b)

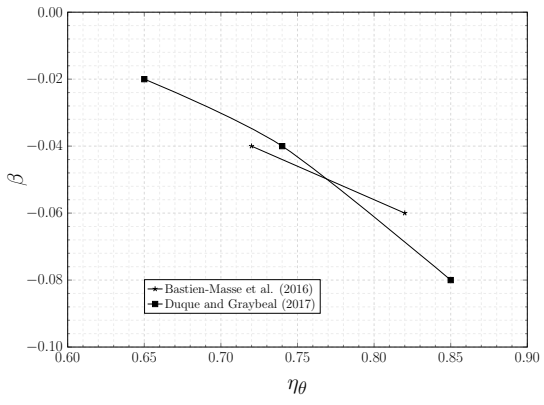

Source: the author.

Other factors influence the composite response. Depending on the type of concrete, fiber type, and matrix density, the increase in fiber content above a specific value can impair matrix density, resulting in more porosity and entrapped air due to the worst compaction. For UHPFRC, Yoo, Lee, and Yoon [112] found that increasing fiber content until 2% resulted in the best pullout performance. However, further increases presented deleterious effects evidencing the presented arguments. Another effect, still not deeply studied, that can occur in the composite with larger fiber content is the bundling effect, which occurs when the fibers remain grouped (in contact) after mixing. Kim and Yoo [34] observed a reduction in pullout load of 52% for fibers tested in this way. In addition, there is a reduction in the friction stress as the fiber-matrix contact area is reduced. The number of fiber bundles is tough to quantify, but it influences the $\bar{\beta}$ and ξ parameters for sure.

Fibers with a higher Poisson coefficient than that of the matrix tend to contract more than the matrix in any pullout test. However, in combination with all other effects, it can exert a higher influence on the composite behavior.

The present GA analysis allowed account for all such phenomena from inverse analysis which usually will not appear in single fiber pullout tests and are very difficult to quantify individually in the composite behavior.

Numerical tensile test results

Figure 65 shows the numerical and experimental results of the experimental campaigns. Those called FEM (GA) were obtained through the calibrating of the model by GA, whereas FEM (average) were acquired by average parameters ($\xi = 0.84$ and $\bar{\beta} = -0.07$ for 2%, and $\xi = 0.50$ and $\bar{\beta} = -0.06$ for 3% and 3.8% of fiber content). In general, the model predicted the material behavior well for different fiber contents and orientations. The UHPFRC tensile response can exhibit either a strain-hardening behavior, or a strain-softening one. For the first case, multiple cracking occurs and the load capacity increases until maximum stress. Strain localization then occurs and reflects the fiber pullout concentration in a macro crack, consequently, dropping stress, as shown in fig. 65(a). In the second case, localization occurs at the crack onset, due to a low redistribution capacity of the composite (see fig. 65(b)). Redistribution depends on fiber surface roughness and length, matrix composition, fiber distribution, and orientation [93, 23, 113]. Interestingly, the strain-hardening behavior started to be exhibited in samples with 2% of fiber content, but depending on the fiber orientation. From 1% of fiber content, the behavior was strain-softening even with a high orientation coefficient. Those results confirm both fiber content and orientation define the post-peak behavior of the material, as discussed in [3, 10, 84]. The constitutive model predicted these two possible types of UHPFRC tensile response.

Figure 65 – Simulation of UHPFRC tensile behavior

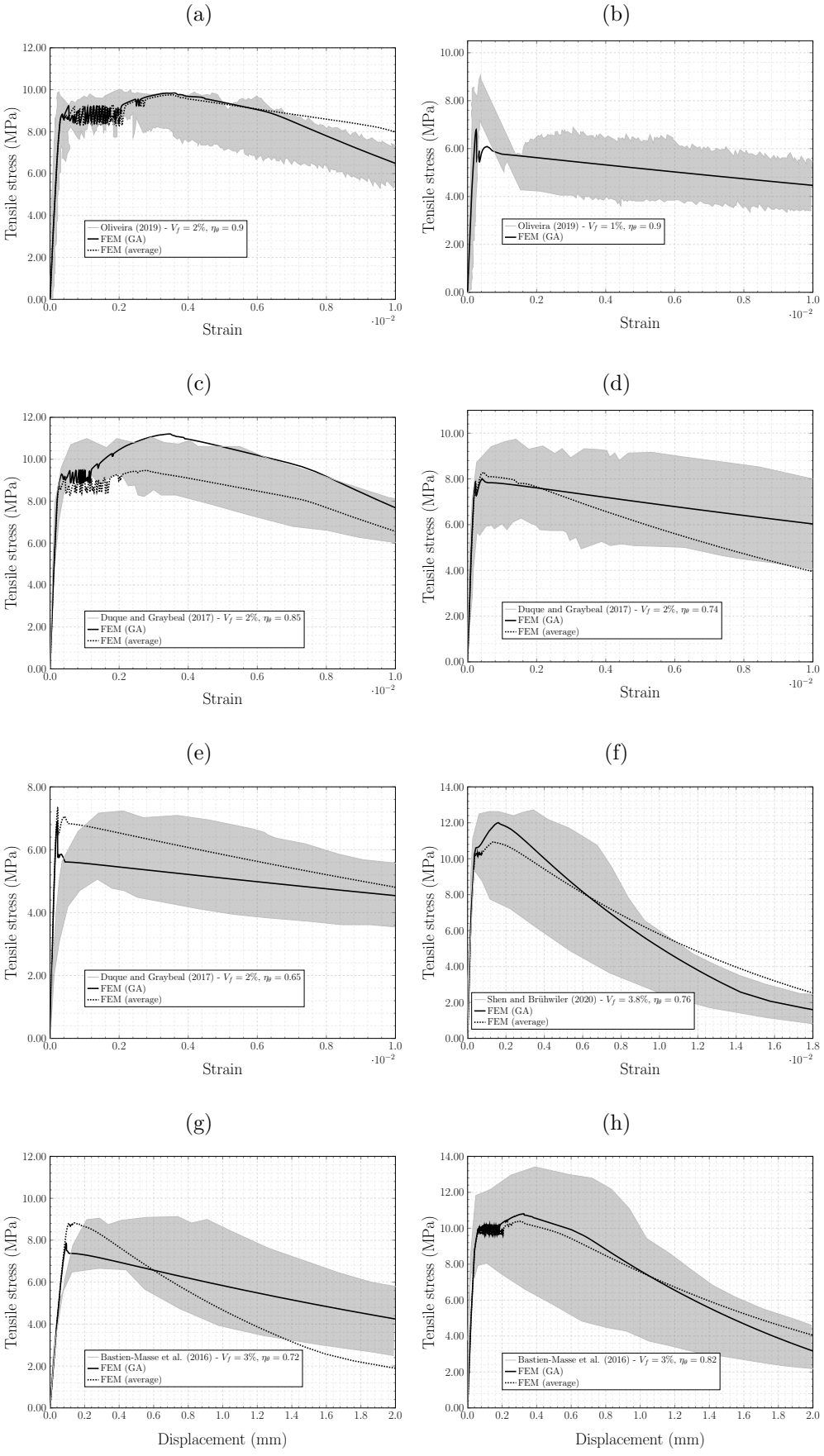

Source: the author.

5.4.2 Homogeneous versus heterogeneous material model

The tensile tests performed by Oliveira [4] were also simulated using heterogeneous modeling. Figure 66 depicts the distribution of fibers for samples with 1% and 2% of fiber content. Three numerical models were simulated with the same orientation coefficient (η_θ) for each concrete, since fiber dispersion is random and can vary slightly.

Figure 66 – Distribution of fibers in the numerical model (a) 1% (b) 2% of fiber content

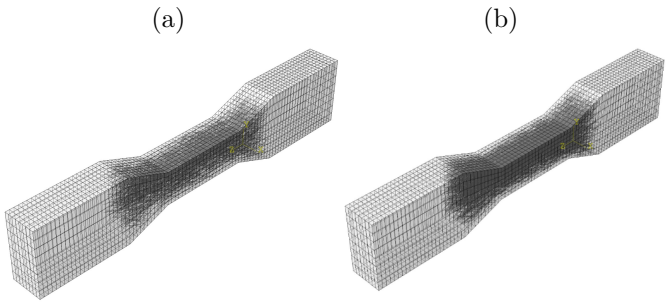

Source: the author.

A 15% reduction in the bond strength was adopted for composites with 2% of fiber content so that the group effect could be considered (consistent with it was adopted in the one-phase model). Figure 67 shows the experimental and numerical results for UHPFRC with 1% and 2% of fiber content. The results were similar to those from the one-phase modeling; however, the processing time was significantly longer for the two-phase model. Therefore, one-phase modeling has proved as accurate as two-phase modeling and more computationally efficient.

Figure 67 – Comparison between two-phase and one-phase modeling

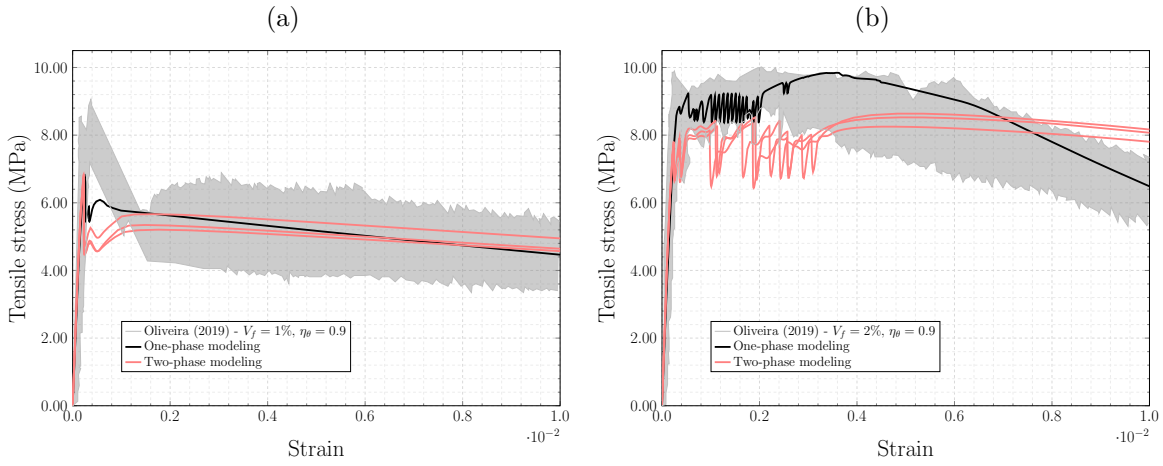

Source: the author.

An advantage of heterogeneous modeling is the possibility of evaluating each phase separately. As an example, fig. 68 shows the fiber bridging behavior is more activated after the concrete cracks. After the first crack, the fiber stress increases, since the concrete

capacity is reduced and fiber carries more stress through the bridge effect. Figure 68(a) displays the strain-softening behavior. After the beginning of the cracking, there is the concentration of the crack in a region. In contrast, Figure 68(b) illustrates the strain-hardening behavior. The material has a redistribution capacity when it forms multiple cracks after crack initiation.

Figure 68 – Fiber stress (a) UHPFRC with 1% fiber (b) UHPFRC with 2% fiber

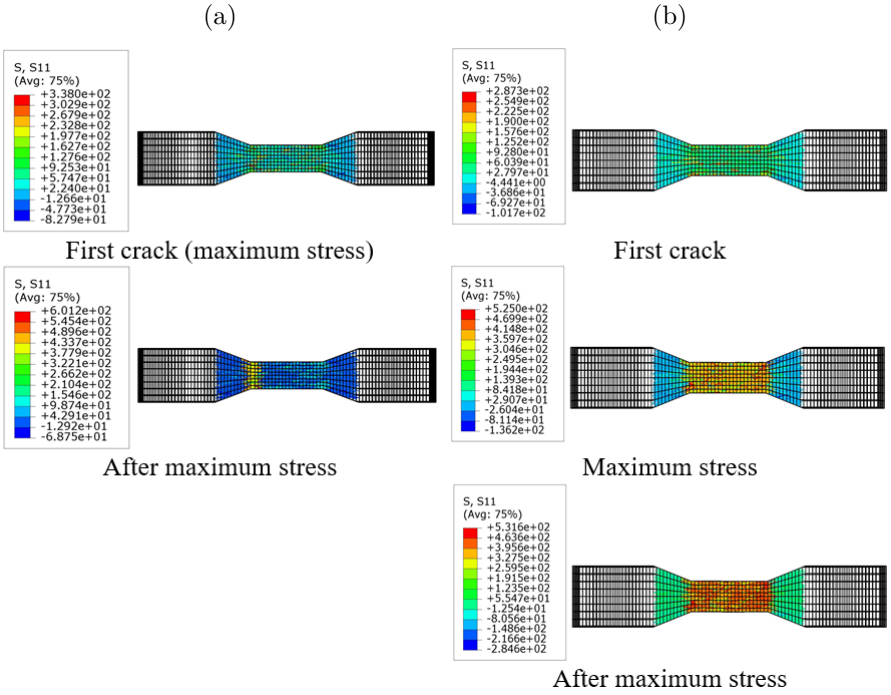

Source: the author.

5.5 Parametric analysis

The tensile behavior of UHPFRC is highly dependent on fiber and matrix properties, fiber content and orientation, and interfacial parameters. The homogeneous model shown in fig. 57 was used in the parametric analysis.

5.5.1 Effect of orientation coefficient

The orientation coefficient effect on the tensile response of UHPFRC with 2% of fiber content is exemplified in fig. 69. The evaluated orientation coefficients were $\eta_\theta = 1$ ($\theta_{mean} = 0^o$), $\eta_\theta = 0.966$ ($\theta_{mean} = 15^o$), $\eta_\theta = 0.866$ ($\theta_{mean} = 30^o$), $\eta_\theta = 0.707$ ($\theta_{mean} = 45^o$), $\eta_\theta = 0.500$ ($\theta_{mean} = 60^o$), $\eta_\theta = 0.259$ ($\theta_{mean} = 75^o$), and $\eta_\theta = 0$ ($\theta_{mean} = 90^o$). Interestingly, the maximum stress occurs for $\eta_\theta = 0.866$ ($\theta_{mean} = 30^o$), which is in agreement with the findings of other [35, 114]. The behavior is due to the fiber snubbing effect under the inclined fiber pullout [103, 114, 27]. Inclined fibers have a component of friction occurring

at the end of fiber channel due to the load deviation, which increases the required load to sliding out the fiber. Moreover, steel fibers have bending stiffness, which is another component of energy dissipation for the inclined pullout. The maximum fiber efficiency is achieved when the fiber is inclined at around 30º, as discussed in [27, 24, 35]. Therefore, a fiber orientation distribution with those characteristics optimizes the composite fiber efficiency. Among the orientation coefficients evaluated, the best results are between $\eta_\theta = 0.707$ and $\eta_\theta = 0.966$. Most of the experimental results evaluated in this study were within that range. Moreover, the fibers contribution is nil for $\eta_\theta = 0$. The stress relative to the first crack was 8.72 MPa for $\eta_\theta = 0.866$, and 4.93 MPa for $\eta_\theta = 0$ and the maximum stress was 9.65 MPa for $\eta_\theta = 0.866$, as presented strain-hardening behavior. Therefore, fiber orientation is a fundamental factor for composite tensile response and optimization and its correct adoption in a numerical model is essential for predicting the composite behavior.

Figure 69 – Effect of orientation coefficient

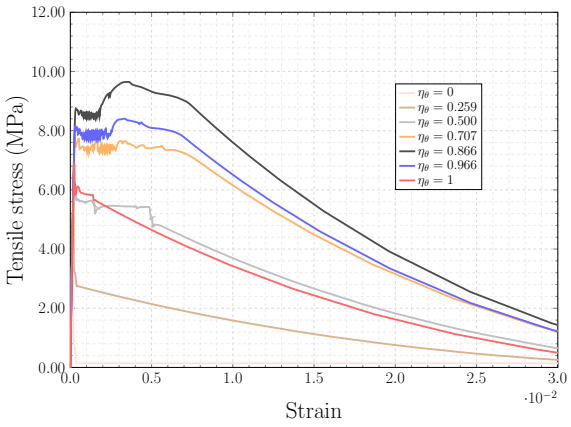

Source: the author.

5.5.2 Effect of fiber content and average bond strength

Figure 70(a) shows the fiber content increase improves composite strength when proper mixing techniques are applied. On the other hand, a worst compaction is deleterious, as claimed by Yoo, Lee, and Yoon [112] for UHPC with fiber content above 2%. The improvement is not proportional to the fiber content due to the group effect, which reduces the fiber efficiency [35, 34, 21]. Such a phenomenon can be represented in a simulation by reducing the average bond strength, which can be also attributed to the early debond due to stress concentrations at the fiber ends [111]. The effect of average bond strength on the UHPFRC tensile response is shown in fig. 70(b). This interfacial parameter exerts a slight influence on the stress relative to the first crack, but a considerable one on the post-peak, since friction is the main stress transfer mechanism between fiber and matrix during fiber pullout. Therefore, the average bond strength definition is fundamental for

the model to predict the composite response correctly. During validation, it was the most critical parameter for the calibration of the numerical model.

Figure 70 – Effect of (a) fiber content (b) average bond stress

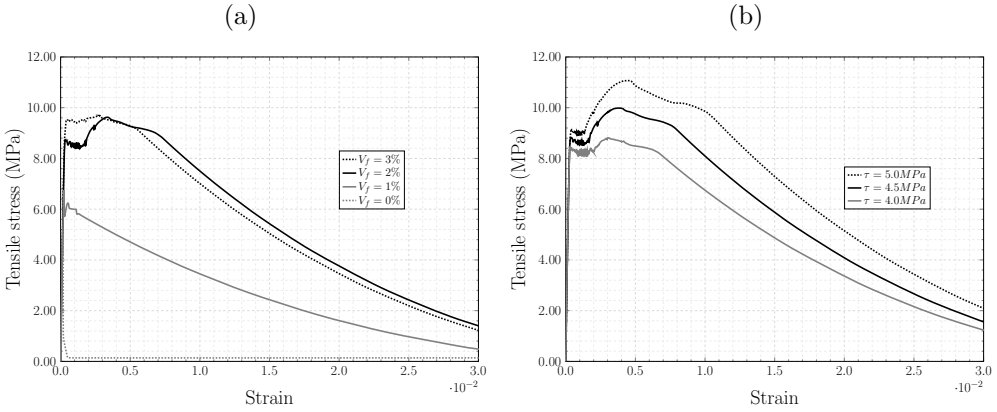

Source: the author.

5.5.3 Effect of $\bar{\beta}$ coefficient

Figure 71 dipslays three situations, $\bar{\beta} = 0$, $\bar{\beta} = -0.07$, and $\bar{\beta} = 0.07$, reminding such a parameter governs the post-peak branch of the pullout curve. In the experimental tests simulated, $\bar{\beta}$ ranged from -0.02 to -0.12. According to Bentur and Mindess [37], the pullout of fibers in the composite is much more complex than that in the pullout test, because the propagation of a crack in the matrix tends to deviate parallel to the fiber axis, since it reaches the fiber neighborhood. The weakest zone is not located exactly in the interface. Such a negative value for $\bar{\beta}$, which represents a more sudden drop in load, is believed to be due to matrix micro-cracking surrounding fibers that negatively affects the fiber-matrix interaction. Consequently, the stress of the composite also follows the trend.

Figure 71 – Effect of the $\bar{\beta}$ coefficient

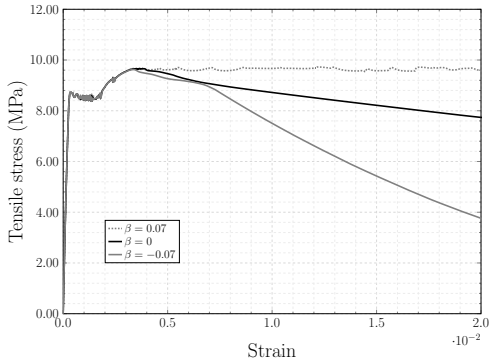

Source: the author.

5.6 Conclusions

This chapter proposed a micromechanics-based constitutive model for the prediction of the UHPFRC tensile behavior. Essential factors such as fiber content and orientation, interfacial parameters, and group effect, as well as micromechanical phenomena (e.g., matrix spalling and fiber snubbing) are considered. In what follows are the conclusions reached and some recommendations:

- The composite strength improves with fiber content, but not linearly for fiber contents above 2%. As the fiber content increases, the spacing between the fibers decreases and the interaction between them influences negatively the composite behavior. The phenomenon is known as the group effect and was considered through the introduction of parameter ξ in Li model. ξ ranges between 0 and 1 and reduces average bond strength τ. $\bar{\beta}$ controls the shape of the curve after cracking. Both ξ and $\bar{\beta}$ were calibrated according to experimental results and the following average values were obtained: $\xi = 1.00$ and $\bar{\beta} = -0.07$ for 1% of fiber content, $\xi = 0.84$ and $\bar{\beta} = -0.07$ for 2% of fiber content, and $\xi = 0.50$ and $\bar{\beta} = -0.06$ for 3% and 3.8% of fiber content. However, the results showed the orientation coefficient also influences those parameters, since ξ reduced and $\bar{\beta}$ increased with a reduction in the such a coefficient.

- The contribution of fibers to the composite response is maximum when its inclination with the normal direction to the cracking plane is around 30^{o} due to the fiber snubbing effect. The minimal contribution of fibers is made when they are perpendicular to the loading direction. The maximum stress varied between 4.93 MPa ($\eta_\theta = 0$) and 9.65 MPa ($\eta_\theta = 0.866$) for UHPFRC with 2% of fiber content, confirming the importance of the orientation coefficient in the tensile behavior of UHPFRC.

- The results of the proposed homogeneous model were very close to those from the heterogeneous model, validating the approach. Homogeneous modeling offers advantages such as simplicity in simulation and low computational cost over the heterogeneous one.

- This chapter proposed a UHPFRC modeling methodology and provided all parameters, functions, and guidelines for its application. The stress-crack opening curve used in the finite element model was presented in a simplified way. The suggestion of fiber orientation distribution function $p(\theta)$ is based on normal distribution. The proposed $g(\theta)$ function considers matrix spalling and fiber snubbing effects and is based on experimental results. In general, the model accurately predicted the tensile behavior of UHPFRC.

SIX

INVESTIGATION OF THE MECHANICAL BEHAVIOR OF UHPFRC: EXPERIMENTAL APPROACH

The UHPC and UHPFRC samples presented in chapter 3 were subjected to tensile, compression, and bending tests for evaluations of the effect of orientation and fiber content on the mechanical behavior of the composite. Cylindrical samples were subjected to a compression test, whereas dogbone ones were submitted to a tensile test. A bending test was applied to prismatic samples. The group effect was evaluated by multi-fiber pullout test.

6.1 Compression test

Cylindrical samples of 50x100 mm were tested under displacement control in a universal testing machine of 1500 kN maximum load capacity and 0.005 mm/s displacement rate. The linear branch of the stress-strain curve was obtained by two clip-gage. And the nonlinear one was measured by two displacement transducers (LVDT) with a 100 mm measuring base positioned between the plates of the test machine.

Figure 72 – Compression test setup

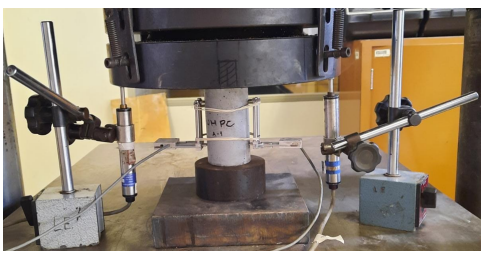

Source: the author.

The modulus of elasticity was calculated according to ASTM C469/C469M-14 [115], by

$$E_c = \frac{0.4f_c - f_1}{\varepsilon_2 - 0.00005} \tag{6.1}$$

where E_c is modulus of elasticity, f_c is compression strength, f_1 is compression stress corresponding to 0.00005 mm/mm longitudinal strain, and ε_2 is strain corresponding to $0.4f_c$ stress.

The initial slope of the stress-strain curves obtained by the clip-gage and LVDT is different, since LVDT records the accommodations between the machine and the specimen at the beginning of the test. Equation 6.2 corrects this effect:

$$\varepsilon_1 = \varepsilon_{1,LVDT} - \frac{E_{clip} - E_{LVDT}}{E_{clip} \cdot E_{LVDT}} \cdot \sigma_1 \tag{6.2}$$

where ε_1 is the corrected longitudinal strain, $\varepsilon_{1,LVDT}$ is the average longitudinal strain obtained by LVDTs, σ_1 is the compression stress corresponding to strain $\varepsilon_{1,LVDT}$, and E_{clip} and E_{LVDT} are the modules of elasticity obtained by the clip gage and LVDT, respectively.

Figure 73 displays the average curves obtained in the compression test. UHPC samples showed 116.51 MPa average compressive strength and 41.23 GPa elastic modulus. UHPFRC-1 (1% of fiber content) showed 142.68 MPa average strength and 43.53 GPa modulus of elasticity and UHPFRC-2 (2% of fiber content) showed 163.41 MPa average strength and 47.30 GPa modulus of elasticity. The strength gain was approximately 22.5% and 40% with the addition of 1% and 2% fiber, respectively and the modulus of elasticity increased approximately 5.6% and 14.7% with those additions.

Figure 73 – Experimental compression stress-strain curve

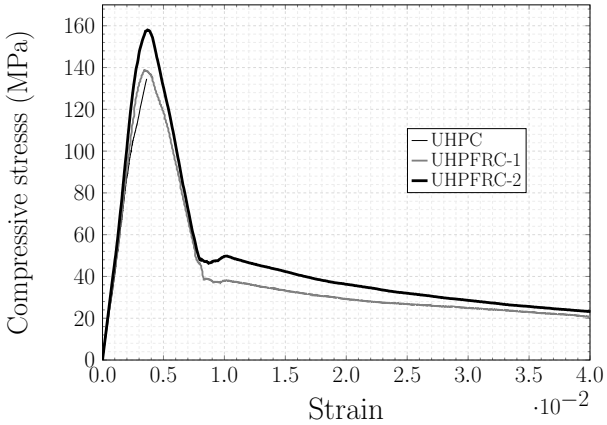

Source: the author.

Figure 74 depicts the specimens after the test. As expected, the UHPC rupture is brittle, whereas in UHPFRC, the fibers form bridges between the cracks, delaying their propagation

Figure 74 – Specimens after compression test

UHPC | UHPFRC – 1% | UHPFRC – 2%

Source: the author.

6.2 Tensile test

Dogbone-shaped samples were tested by a universal servo-hydraulic machine of 1500 kN maximum capacity and 0.005 mm/s displacement. The stress-strain curve was obtained by two LVDTs positioned in the central region of the sample with an 80 mm measurement base. Figure 75 shows the configuration of the test.

Figure 75 – Tensile test setup

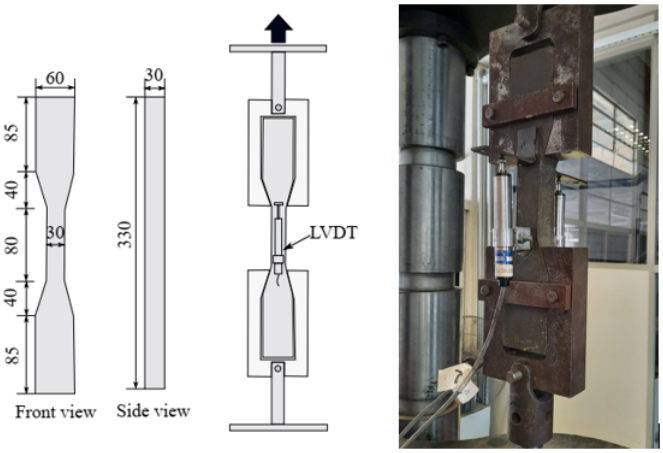

Source: the author.

Figure 76 depicts the average curves resulting from the tensile test, where the influence of fiber content and orientation on the tensile response of the composite can be observed. Note UHPFRC-1 with a 0.73 orientation coefficient exhibited a strain-softening behavior. In contrast, UHPFRC-1 with a 0.793 orientation coefficient displayed a strain-hardening behavior, confirming the importance of fiber orientation for both material optimization and design of UHPFRC structural elements.

Figure 76 – Experimental tensile stress-strain curve

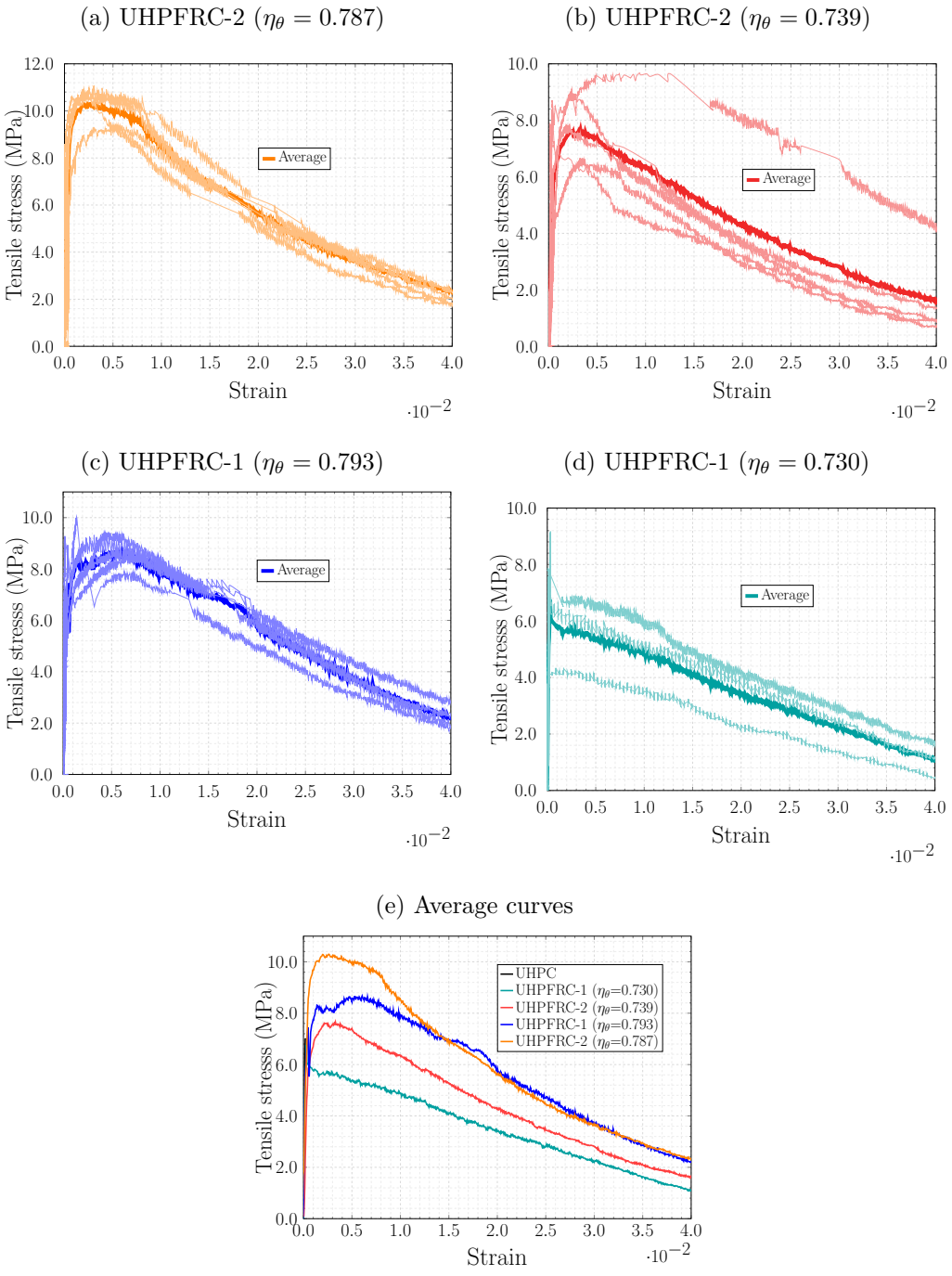

Source: the author.

Table 18 summarizes the results. The addition of 1% of fibers increased the composite tensile strength by 19% and 36% for orientation coefficients of 0.730 and 0.793, respectively, and the addition of 2% improved the tensile strength by 20% and 54% for orientation coefficients of 0.739 and 0.787, respectively.

Table 18 – UHPFRC tensile strength

V_f (%)	η_θ	f_t (MPa)
0	-	6.86
1	0.730	8.16
1	0.793	9.33
2	0.739	8.24
2	0.787	10.58

Source: the author.

Figure 77 depicts the failure mode of the samples. UHPC showed brittle rupture, UHPFRC-1 displayed a localized crack, typical of the strain-softening behavior, and UHPFRC-2 developed multiple cracks, a typical pattern of strain-hardening behavior.

Figure 77 – Cracking pattern - tensile test

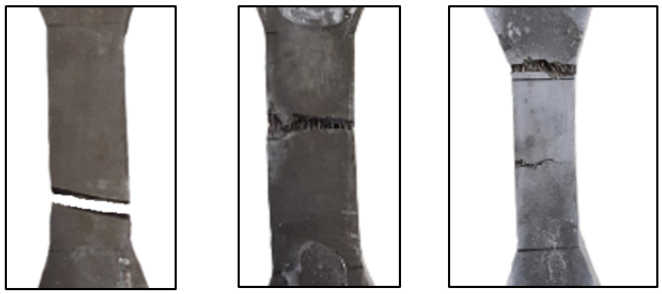

Source: the author.

6.3 Three-point bending test

Prismatic specimens measuring 40x40x160 mm^3 with a 7 mm notch in the middle of the span were tested. Prisms are generally recommended to rotate 90º from the casting direction for reducing surface roughness during force application. However, since this study aims at evaluating the orientation of the fibers, the authors chose not to rotate the sample. The test was controlled by crack opening displacement at 0.0001 mm/s initial rate and a clip-gage was attached to the notch for the obtaining of the force-crack opening curve. Two LVDTs in the central region of the specimen acquired the force-vertical displacement curve. Figure 78 shows the bending test.

Figure 78 – Bending test setup

Source: the author.

Figures 79 and 80 , respectively, depict the cracked region of some samples and the response of the composite under the three-point bending test. The influence of fiber content and orientation is evident. As an example, a sample with 1% of fibers and 0.746 orientation coefficient displays a behavior similar that of a sample with 2% of fibers and 0.699 orientation coefficient, showing fiber orientation is an important factor in material optimization. The orientation of fibers in the principal tensile stress direction significantly improves the behavior of the composite even with a low fiber content.

Figure 79 – Fibers crossing the crack faces

UHPFRC-2 (0.699) UHPFRC-2 (0.753) UHPFRC-2 (0.810)

Source: the author.

Figure 80 – Experimental load-crack opening curve – bending test

(a) UHPFRC 2 - $\eta_\theta = 0.810$

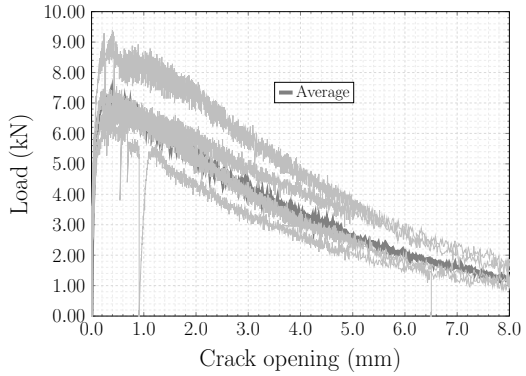

(b) UHPFRC 2 - $\eta_\theta = 0.753$

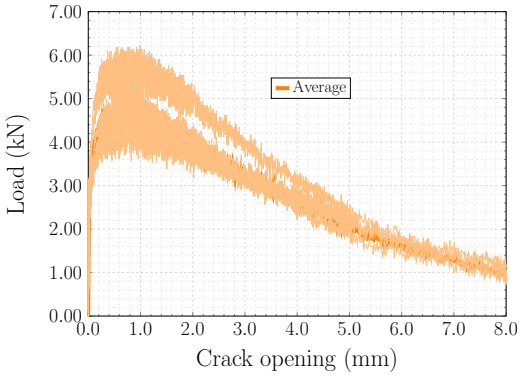

(c) UHPFRC 2 - $\eta_\theta = 0.699$

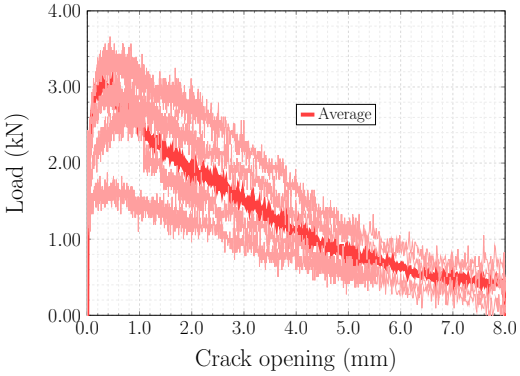

(d) UHPFRC 1 - $\eta_\theta = 0.797$

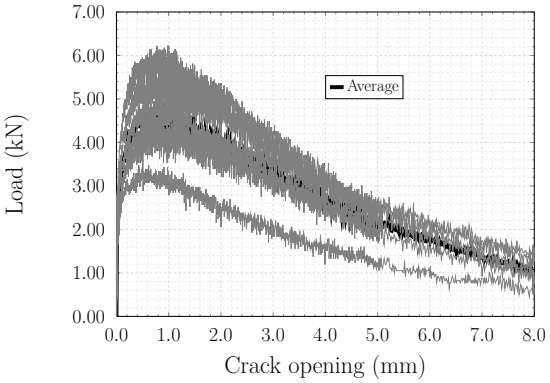

(e) UHPFRC 1 - $\eta_\theta = 0.746$

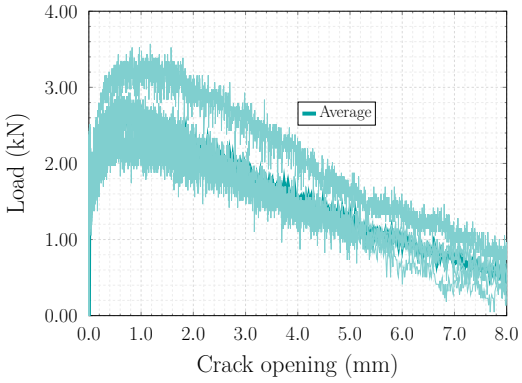

(f) UHPFRC 1 - $\eta_\theta = 0.680$

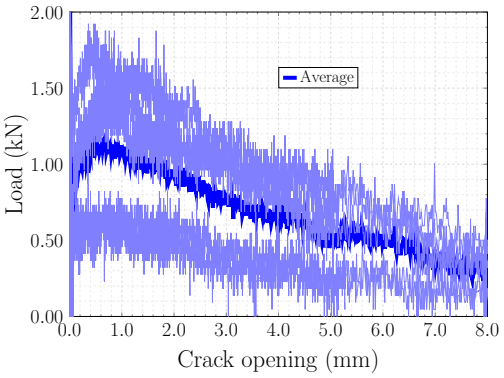

(g) Average curves

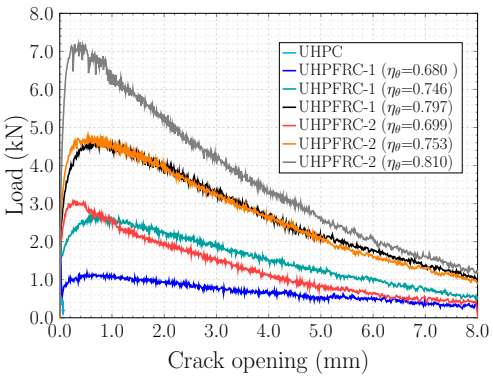

Source: the author.

The bending stresses were calculated by eq. (6.3), according to RILEM TC 162-TDF [116].

$$\sigma = \frac{3FL}{2b(h-a_0)^2}, \tag{6.3}$$

where σ is bending stress, F is applied force, L is span length, b is prism width, h is prism height, and a_0 is notch height.

The fracture energy was quantified by eq. (6.4), as proposed by RILEM 50 FMC [117].

$$G_f = \frac{W_0 + m_0 g \delta_0}{b(h-a_0)}, \tag{6.4}$$

where G_f is fracture energy, W_0 is area under the force-vertical displacement curve at midspan, m_0 is mass of the prism between the supports, g is acceleration due to gravity, δ_0 is ultimate displacement, b is width of the prism, h is height of the prism, and a_0 is height of the notch. Table 19 summarizes the results.

Table 19 – Flexural strength of UHPFRC

V_f (%)	η_θ	Flexural strength (MPa)	G_f (N/mm)
0	-	10.76	0.04
1	0.680	11.39	3.37
1	0.746	14.05	7.31
1	0.797	23.91	12.84
2	0.699	16.82	5.78
2	0.753	24.61	12.61
2	0.810	36.73	19.36

Source: the author.

6.4 Pullout test

The steel fibers were fixed in styrofoam positioned at the bottom of the 30 x 30 x 3 cm^3 formwork, as shown in fig. 81, and immersed in the matrix with 3.25mm embedding length, corresponding to $l_f/4$ (expected value for embedding length). The immersed length of the fiber was measured by a digital caliper (fig. 81). Next, the fibers were fixed to the styrofoam with a mold with predetermined spacings between them and the group effect was evaluated by pulling a group of four fibers with spacing (s) of 2.5 mm, 1.8 mm, 1.2 mm, 1 mm, 0.8 mm, and 0 mm. The matrix without fibers and the matrix with 1% of

fiber content were then evaluated - ten samples per spacing were tested. Figure 81 shows the plates after molding.

Figure 81 – Details of the fibers fixed in the styrofoam plate and anchored into the concrete plate

Source: the author.

The fiber pullout test was performed by a portable apparatus developed by Krahl et al.[24], as illustrated in fig. 82. The displacement was applied through a set of ball screws and a stepper motor, which enables the progress of the machine crosshead with an above 0.001 mm resolution and 0.01 mm maximum error. The grip clamps the fiber close to the matrix surface and a hinge connects the grip to the load cell. Data were acquired at 4 Hz frequency and with the use of a 500 N load cell. The test machine was approximately 300 mm high, weighting 3 kg. It rests on three points on the concrete surface for testing, which provides stability for the pullout load application. In the current study, the fibers were pulled at 0.005 mm/s speed.

Figure 82 – Portable machine [24]

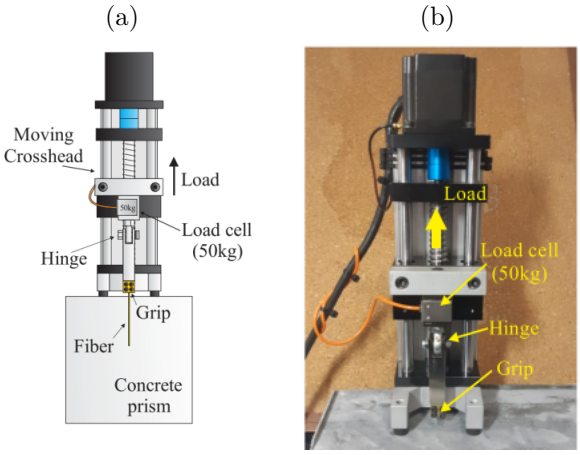

Source: Krahl et al. [24].

Figure 83 shows the concrete plate with the fibers immersed in the matrix with 3.25 mm length and fibers clamped at the grip after pullout.

Figure 83 – Pullout test

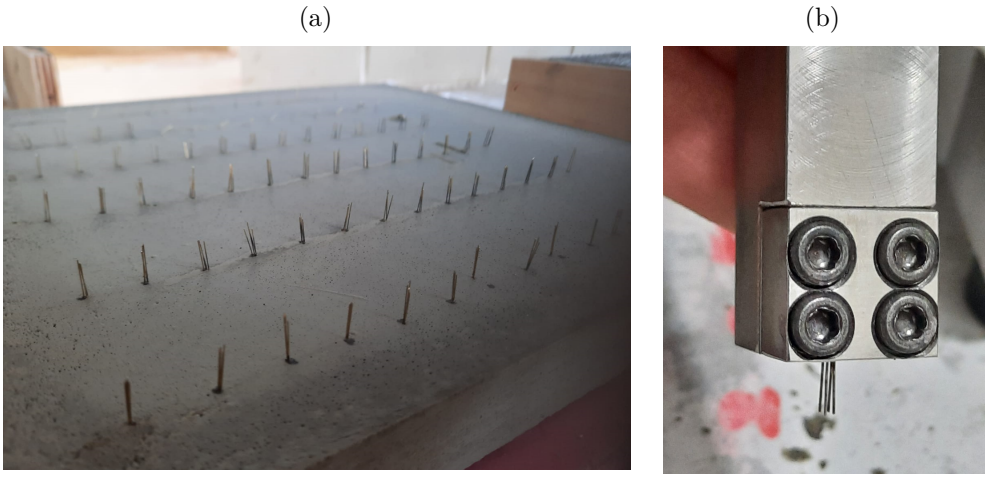

Source: the author.

Regarding the UHPC plate without fibers, the fiber/matrix bond strength was close to 23.6 MPa for fiber spacings of 2.50 mm, 1.80 mm, and 1.2 mm, close to 15.8 MPa (33.05% reduction) for spacings of 1.0 mm and 0.80 mm, and close to 2.82 MPa (88.05% reduction) for fibers without spacing. For the UHPFRC plate with 1% of fiber content, the fiber/matrix bond strength was close to 31.5 MPa for fiber spacings of 2.50 mm, 1.80 mm, and 1.2 mm, close to 20.4 MPa (35.24% reduction) for spacings of 1.0 mm and 0.80 mm, and close to 7.64 MPa (75.75% reduction) for fibers without spacing. The results clearly show the group effect influence on the bond strength.

Figure 84 – Results of fiber pullout test (a) UHPC (b) UHPFRC-1

(a)

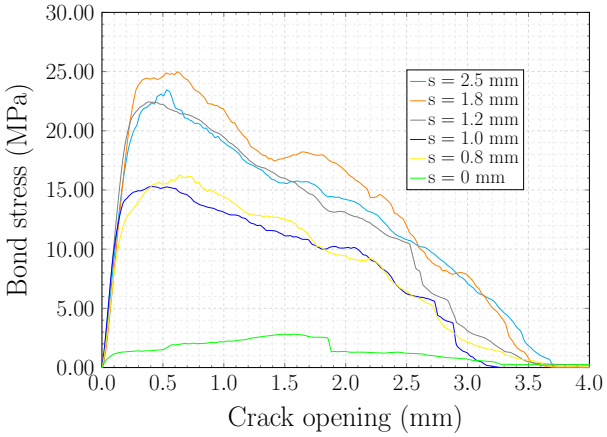

(b)

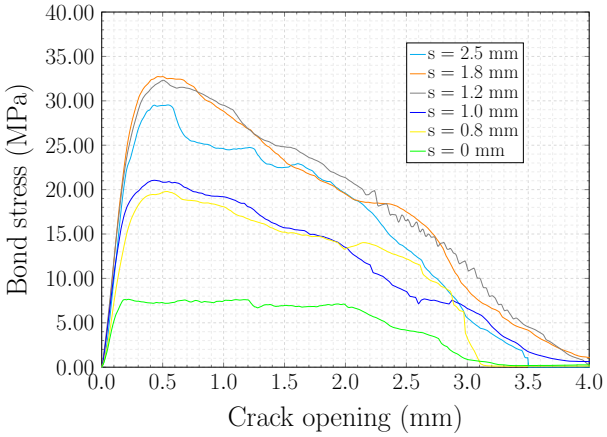

Source: the author.

As shown in fig. 85, the distribution of fibers is not uniform and the spacing between them varies. In regions of less spaced fibers, the pullout load is lower due to the group effect, as discussed elsewhere. Therefore, the group effect must be considered during the modeling or design of UHPFRC structures.

Figure 85 – Example of fiber distribution in a sample

Source: the author.

6.5 Conclusions

The effect of fiber content and arrangement on the UHPC mechanical behavior was investigated by experimental tests and the following conclusions have been drawn:

- Cylindrical specimens measuring 50 x 100 mm^2 were tested in compression. UHPC samples showed 116.51 MPa compressive strength and 41.23 GPa elastic modulus, and those with 1% of fibers showed 142.68 MPa average compressive strength and 43.53 GPa elastic modulus, representing 22.5% and 5.6% increases, respectively. UHPC samples with 2% of fibers showed 163.41 MPa compressive strength and 47.3 GPa elastic modulus, representing 40% and 14.7% increases, respectively. The results show the elastic modulus increases with fiber content, confirming the discussions in chapter 4.

- Dogbone specimens were tensile tested. The concrete placement methodology influenced fiber orientation and, hence, the tensile response of the composite. The addition of 1% and 2% of fibers to the matrix increased tensile strength by up to 36% and 54%, respectively. Another important aspect is fiber content allied to the concrete placement methodology determines the gain (or not) in strength after the onset of cracking (strain-hardening or strain-softening behavior).

- Prismatic specimens measuring 40 x 40 x 160 mm^3 were flexural tested. Three methods of casting concrete produced the samples. The influence of fiber arrangement on the composite response was evident. The addition of 1% of fibers to the matrix improved the flexural strength from 5.9% to 122.2%, according to the methodology used, and those with 2% fibers improved the flexural strength from 56.3% to 241.4%, in function of the methodology, thus confirming the importance of fiber orientation in UHPFRC structural element designs.

- Finally, a multi-fiber pullout test investigated the group effect. UHPC samples without and with 1% fibers were produced. The fibers were immersed in the matrix with $l_f/4$ embedding length. Groups containing four fibers spaced at 2.5 mm, 1.8 mm, 1.2 mm, 1 mm, 0.8 mm, and 0 mm distances were pulled – the smaller the spacing between the fibers, the more significant the group effect. The fiber-matrix bonding strength was reduced by up to 88.0% for bundled fibers. The literature reports few studies on group effect; however, its non consideration in design can overestimate the strength of the composite. In this sense, future studies should investigate other fiber configurations such as pulling out of inclined multiple fibers.

SEVEN

CONCRETE DAMAGED PLASTICITY MODEL FOR SIMULATING THE UHPFRC BEHAVIOR

The mechanical behavior of UHPFRC is highly sensitive to fiber orientation, as discussed in previous chapters, and the fiber orientation effect was well captured in the model proposed and validated (see chapter 5). However, a previous knowledge of the direction of the principal tensile stress is required for the adoption of the orientation coefficient. This chapter addresses the possibility of the user not knowing the direction of cracking in advance, which is important in more complex states of stress. So, this chapter presents a modification in the Concrete Damaged Plasticity (CDP) model for overcoming such a limitation. The proposed model calculates the principal tensile stress direction and the corresponding orientation coefficient at each integration point and adopt the tensile curve referring to the estimated orientation coefficient. The model assumes the material properties are different in different directions (anisotropic). The CDP model was implemented and validated in the first stage of the research and the modification was implemented in the second stage.

7.1 Background

Most studies that proposed constitutive models for simulating the UHPFRC nonlinear behavior were limited to assessments of the uniaxial tensile test, since the direction of the cracking plane can be known in advance and, consequently, the corresponding orientation coefficient can be adopted. However, a structural element may be subjected to a triaxial stress state, which hampers a previous definition of the crack propagation direction. A constitutive model that assesses the crack propagation direction at each loading increment and updates the tensile curve to be used should be developed. The literature examined reports no detailed study on a direction-dependent plasticity model for UHPFRC [98] and those proposing anisotropic plasticity models for fiber-reinforced

composites were developed for polymer or metal matrix [98, 118, 119, 120, 121]. According to the authors, the design of an anisotropic model is complex even for fiber-reinforced metal or polymer matrix, and such complexity increases for concrete matrix. Valente et al. [122], whose study is one of the most advanced in the field, developed a constitutive model for simulating the anisotropic behavior of UHPFRC implementing an orientation-dependent parameter. The model was validated by a four-point bending test, therefore, the principal tensile direction, which indicates the crack opening direction, is known beforehand and is parallel to the longitudinal plate axis. According to the authors, in cases of more complex geometries and load patterns, crack opening directions are not known beforehand and a more general description of the anisotropic tensile response is required.

This study proposes a model that considers the anisotropy introduced by steel fibers. The direction of crack propagation at each loading step at each integration point is determined. The orientation coefficient is calculated in the principal tensile stress direction according to the orientation coefficient in three previously known directions (in a reference coordinate system). The tensile curve is updated with the orientation coefficient, as shown in the previous chapter, and the direction dependency is incorporated into the model, thus overcoming the limitation of current models. The Concrete Damaged Plasticity model (CDP) was implemented through UMAT subroutine and the directionality dependency was included in the algorithm.

7.2 Concrete Damaged Plastiticity (CDP)

CDP is a model implemented in Abaqus® finite element software and widely used to simulate concrete and other quasi-fragile materials [65]. In the present research, modifications to the model are proposed towards including the anisotropic behavior of UHPRFC due to the fiber orientation distribution. Initially, CDP was studied, implemented, and validated and, subsequently, modifications were made for incorporating the directionality dependence.

7.2.1 Model

CDP is an elastoplastic damage model that simulates concrete structures computing the plastic strain accumulation and the reduction of the elasticity modulus due to material damage by the theory of plasticity and damage mechanics. The model is based on the research developed by Lubliner et al. [96] and Lee and Fenves [97].

Overview

The stress-strain relationship is governed by eq. (7.1)

$$\sigma = (1-d)\mathbf{D}_0^{el} : (\varepsilon - \varepsilon^{pl}) = \mathbf{D}^{el} : (\varepsilon - \varepsilon^{pl}) \tag{7.1}$$

where $\mathbf{D}_0^{el}$ is the initial stiffness of the material; $\mathbf{D}^{el} = (1-d)\mathbf{D}_0^{el}$ is the damaged stiffness matrix, and d is a scalar damage variable ranging from zero (undamaged material) to one (totally damaged material). Therefore, damage results in the isotropic degradation of the material's elastic stiffness. According to the theory of damage mechanics, effective stress is defined by

$$\bar{\sigma} \overset{def}{=} \mathbf{D}_0^{el} : (\varepsilon - \varepsilon^{pl}). \tag{7.2}$$

The plasticity model is decoupled from the damage model and, consequently, effective stress is used in the yielding function. Cauchy stress is related to the effective stress through the scalar damage variable.

$$\sigma = (1-d)\bar{\sigma}. \tag{7.3}$$

Yielding function

The yielding function is based on the function proposed by Lubliner et al. [96] and modified by Lee and Fenves [97] for considering the difference in the strength evolution under tension and compression:

$$F(\bar{\sigma}, \tilde{\varepsilon}^{pl}) = \frac{1}{1-\alpha}(\bar{q} - 3\alpha\bar{p} + \beta(\tilde{\varepsilon}^{pl})\langle\hat{\bar{\sigma}}_{\max}\rangle - \gamma\langle-\hat{\bar{\sigma}}_{\max}\rangle) - \bar{\sigma}_c(\tilde{\varepsilon}^{pl}) \leq 0 \tag{7.4}$$

where:

$$\bar{p} = -\frac{1}{3}\bar{\sigma} : \mathbf{I}$$

is the effective hydrostatic stress,

$$\bar{q} = \sqrt{\frac{3}{2}\bar{\mathbf{S}} : \bar{\mathbf{S}}}$$

is Mises equivalent effective stress,

$$\alpha = \frac{\sigma_{b0} - \sigma_{c0}}{2\sigma_{b0} - \sigma_{c0}}$$

is a dimensionless coefficient from the relation between initial yield compressive stress (σ_{c0}) and biaxial initial yield compressive stress (σ_{b0}),

$$\beta(\tilde{\varepsilon}^{pl}) = \frac{\bar{\sigma}_c(\tilde{\varepsilon}^{pl})}{\bar{\sigma}_t(\tilde{\varepsilon}^{pl})}(1-\alpha) - (1+\alpha)$$

is a dimensionless coefficient based on hardening/softening evolution law provided by the user,

$$\gamma = \frac{3(1-K_c)}{2K_c - 1}$$

is a dimensionless coefficient obtained from K_c constant that governs the spacing between compression and tension meridians and the section shape of yielding surface on the deviatoric plane. The lower and upper limits of K_c are 0.5 and 1, and

$\langle\hat{\bar{\sigma}}_{\max}\rangle$ is the algebraically largest eigenvalue of the effective stress tensor. Note β is introduced if the maximum principal stress is positive, whereas γ is introduced if it is negative.

Figure 86 shows the yield surfaces on the deviatoric plane for different K_c values. The value suggested by Abaqus is 2/3.

Figure 86 – Yield surfaces (a) different K_c [123] (b) hardening on the deviatoric plane

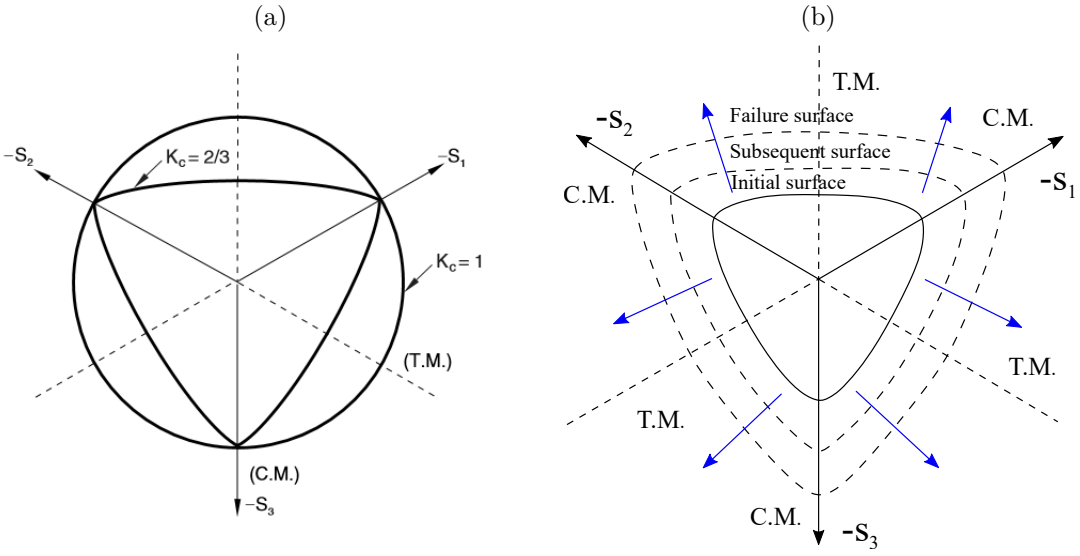

Source: adapted from Chi el al.[99].

Hardening/softening law

The evolution of the yielding function is controlled by tensile equivalent plastic strain $\tilde{\varepsilon}_t^{pl}$ and compressive equivalent plastic strain $\tilde{\varepsilon}_c^{pl}$, related to the failure mechanisms under tension and compression, respectively. Effective tensile ($\bar{\sigma}_t$) and compression ($\bar{\sigma}_c$)

stresses are obtained from those variables and the stress-strain curves provided by the user.

The model assumes both concrete uniaxial tension and compression response are characterized by plasticity and damage, as shown in fig. 87.

Figure 87 – Uniaxial stress-strain response of concrete in CDP

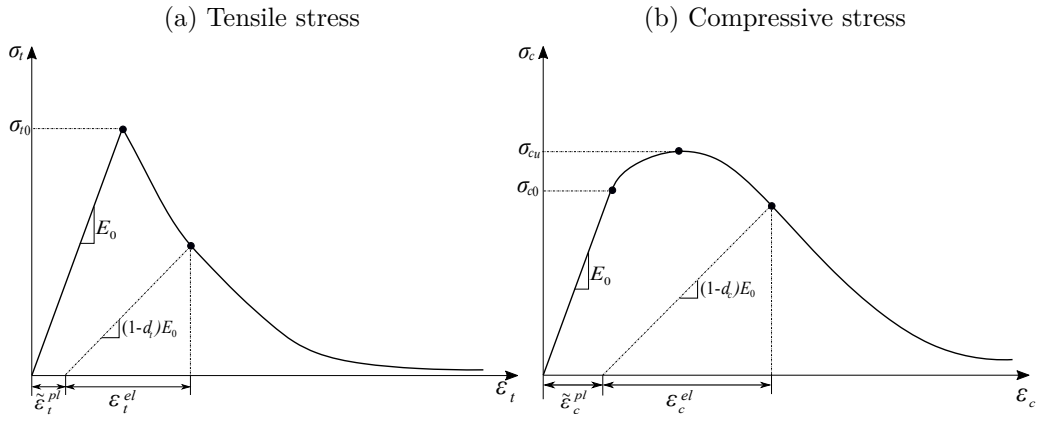

Source: adapted from Abaqus [123].

The user provides the stress-inelastic strain curve ($\tilde{\varepsilon}^{in}$), with $\tilde{\varepsilon}^{in} = \varepsilon - \sigma/E_0$ and Abaqus automatically converts the inelastic strain into plastic strain through eqs. 7.5 and 7.6.

$$\tilde{\varepsilon}_t^{pl} = \tilde{\varepsilon}_t^{in} - \frac{d_t}{1-d_t}\frac{\sigma_t}{E_0} \tag{7.5}$$

$$\tilde{\varepsilon}_c^{pl} = \tilde{\varepsilon}_c^{in} - \frac{d_c}{1-d_c}\frac{\sigma_c}{E_0} \tag{7.6}$$

Note if only the plasticity model is adopted, d_t and d_c are zero. Therefore, plastic strain coincides with inelastic strain. The compression and tension stresses used in the yielding function are defined by

$$\bar{\sigma}_t = \frac{\sigma_t}{(1-d_t)}, \tag{7.7}$$

$$\bar{\sigma}_c = \frac{\sigma_c}{(1-d_c)}. \tag{7.8}$$

Plastic potential

The model assumes a non-associative plastic flow. The plastic potential adopted is the hyperbolic Drucker-Prager function presented in eq. (7.9).

$$G = \sqrt{(\epsilon\sigma_{t0}\tan\psi)^2 + \bar{q}^2} - \bar{p}\tan\psi, \tag{7.9}$$

where ψ is the dilation angle, σ_{t0} is the uniaxial tensile strength of concrete, and ϵ is an eccentricity parameter that defines the rate at which the function approaches the asymptote. The plastic potential, which is continuous and smooth, ensures flow direction is uniquely defined. Figure 88 displays the plastic potential surface in the meridional plane.

Figure 88 – Plastic potential in the meridional plane

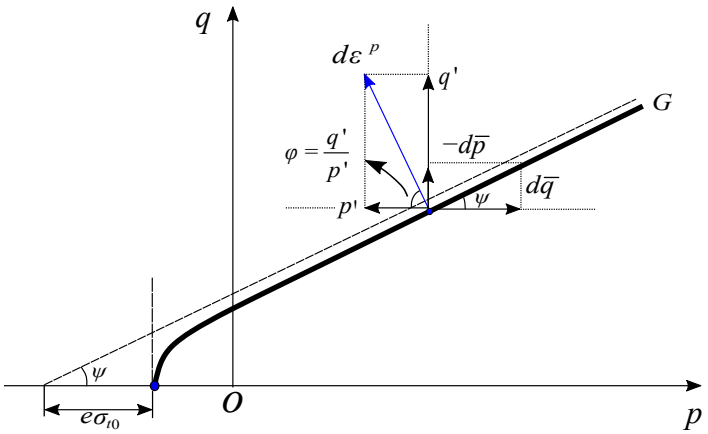

Source: adapted from Chi el al.[99].

The non-associative plastic flow is defined as:

$$\dot{\varepsilon}^{pl} = \dot{\lambda}\frac{\partial G(\bar{\sigma})}{\partial \bar{\sigma}}, \tag{7.10}$$

where λ is the plastic multiplier.

Evolution of hardening variables

Based on Lee and Fenves[97], the tension and compression equivalent plastic strain rate are calculated according to eq. (7.11) and eq. (7.12), respectively.

$$\dot{\tilde{\varepsilon}}_t^{pl} \overset{def}{=} r(\hat{\bar{\sigma}})\dot{\hat{\varepsilon}}_{\max}^{pl}, \tag{7.11}$$

$$\dot{\tilde{\varepsilon}}_c^{pl} \overset{def}{=} -(1 - r(\hat{\bar{\sigma}}))\dot{\hat{\varepsilon}}_{\min}^{pl}, \tag{7.12}$$

where $\dot{\hat{\varepsilon}}_{\max}^{pl}$ and $\dot{\hat{\varepsilon}}_{\min}^{pl}$ are, respectively, maximum and minimum plastic strain rates of tensor $\dot{\varepsilon}^{pl}$ and

$$r(\hat{\bar{\sigma}}) \overset{def}{=} \frac{\sum_{i=1}^{3}\langle\hat{\bar{\sigma}}_i\rangle}{\sum_{i=1}^{3}|\hat{\bar{\sigma}}_i|}; \quad 0 \leq r(\hat{\bar{\sigma}}) \leq 1.$$

Note $r(\hat{\bar{\sigma}})$ is one if all principal stresses are positive; therefore, $\dot{\tilde{\varepsilon}}_t^{pl}$ coincides with $\dot{\hat{\varepsilon}}_{\max}^{pl}$, and $\dot{\tilde{\varepsilon}}_c^{pl}$ is zero. If all the principal stresses are negative, $r(\hat{\bar{\sigma}})$ is zero, so $\dot{\tilde{\varepsilon}}_t^{pl}$ is zero, and $\dot{\tilde{\varepsilon}}_c^{pl}$ is $-\dot{\hat{\varepsilon}}_{\min}^{pl}$ (since the hardening variables are positive values). For general cases,

$r(\hat{\bar{\sigma}})$ works as a weight, resulting in both equivalent tensile and compression strain rates. Such variables control the evolution of the yielding surface and the degradation of elastic stiffness.

The isotropic damage model is adopted and, consequently, the stiffness degradation is the same in all directions and a scalar variable d characterizes the damage. Therefore,

$$\mathbf{D}^{el} = (1-d)\mathbf{D}_0^{el}; \quad 0 \leq d \leq 1. \tag{7.13}$$

In a state of mutiaxial stress,

$$(1-d) = (1-s_t d_c)(1-s_c d_t); \quad 0 \leq s_t, s_c \leq 1, \tag{7.14}$$

where:

$$s_t = 1 - w_t r(\hat{\bar{\sigma}}); \quad 0 \leq w_t \leq 1,$$

$$s_c = 1 - w_c(1 - r(\hat{\bar{\sigma}})); \quad 0 \leq w_c \leq 1.$$

Experimental observations on almost fragile materials, including concrete, have shown the compression stiffness is recovered when cracks close by reversing the tension load into compression. On the other hand, the tension stiffness is not recovered in loading changes from compression to tension. This behavior, which corresponds to $w_t = 0$ and $w_c = 1$, is the standard used by Abaqus [65]. Figure 89 illustrates a uniaxial load cycle assuming default behavior.

Figure 89 – Uniaxial load cycle (tension-compression-tension) assuming default values for stiffness recovery factors: $w_t = 0$ e $w_c = 1$

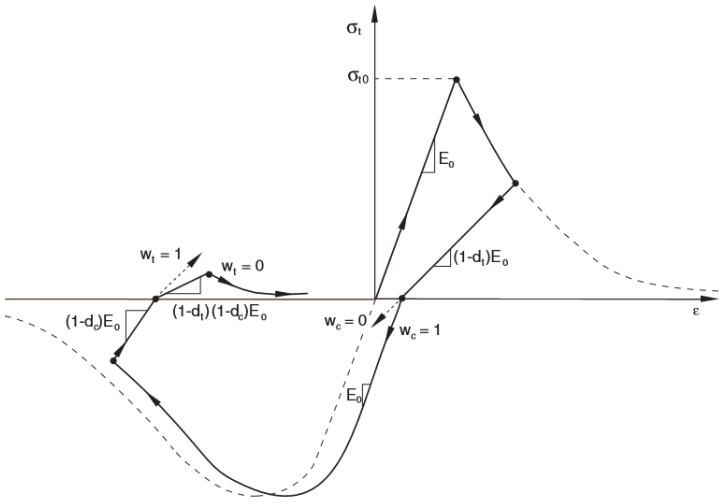

Source: Abaqus [123].

The user provides curves as a function of inelastic strain and the program converts such strain into plastic strain and calculates both damage variables and stresses.

7.2.2 Implementation

The plasticity and damage model was implemented via Fortran code (UMAT subroutine), which was used at all integration points during analyses.

The plasticity model is disassociated from the damage model, thus becoming attractive for numerical implementation [65]. Backward-Euler algorithm presented in detail by Zeng, Horrigmoe, and Andersen [124] was applied at each integration point for a given deformation state following the steps presented below [125].

Algorithm 1: Plasticity Model

(1) Compute trial stress

$$\sigma_{n+1}^{tr} = D_0^{el}(\varepsilon_{n+1} - \varepsilon_n^{pl})$$

(2) Check yielding criteria

$$f_{n+1} = f(\sigma_{n+1}^{tr}, \bar{\sigma}_{c,n}, \bar{\sigma}_{t,n})$$

if $f_{n+1} < 0$ **then** $\sigma_{n+1} = \sigma_{n+1}^{tr}$ and go to **(7)**.

(3) Initial return

$$a_{n+1} = \left.\frac{\partial f}{\partial \sigma}\right|_{\sigma=\sigma_{n+1}^{tr},\bar{\sigma}_c=\bar{\sigma}_{c,n},\bar{\sigma}_t=\bar{\sigma}_{t,n}}$$

$$b_{n+1} = \left.\frac{\partial g}{\partial \sigma}\right|_{\sigma=\sigma_{n+1}^{tr}}$$

$$H = -(1 - r(\hat{\tilde{\sigma}}))\frac{\partial f}{\partial \tilde{\varepsilon}_c^{pl}}\frac{\partial g}{\partial \sigma}\bigg|_{\min} + r(\hat{\tilde{\sigma}})\frac{\partial f}{\partial \tilde{\varepsilon}_t^{pl}}\frac{\partial g}{\partial \sigma}\bigg|_{\max}$$

$$H_{n+1} = H|_{\sigma=\sigma_{n+1}^{tr},\bar{\sigma}_c=\bar{\sigma}_{c,n},\bar{\sigma}_t=\bar{\sigma}_{t,n}}$$

$$\lambda = \frac{f_{n+1}}{(a_{n+1})^T D_0^{el} b_{n+1} - H_{n+1}}$$

$$\sigma_{n+1} = \sigma_{n+1}^{tr} - \lambda D_0^{el} b_{n+1}$$

(4) Iterative return

(4.1) Yielding criteria and application of backward-Euler algorithm

$$b_{n+1} = \left.\frac{\partial g}{\partial \sigma}\right|_{\sigma=\sigma_{n+1}}$$

Update of $\dot{\varepsilon}^{pl}$, $\dot{\varepsilon}_t^{pl}$, $\dot{\varepsilon}_c^{pl}$, $\bar{\sigma}_c$, and $\bar{\sigma}_t$

$$f_{n+1} = f(\sigma_{n+1}, \bar{\sigma}_{c,n+1}, \bar{\sigma}_{t,n+1})$$

$$r = \sigma_{n+1} - (\sigma_{n+1}^{tr} - \lambda D_0^{el} b_{n+1})$$

$$B_{n+1} = \left(\frac{\partial}{\partial \sigma}\right)^T \left.\frac{\partial g}{\partial \sigma}\right|_{\sigma=\sigma_{n+1}}$$

$$Q = I + \lambda D_0^{el} B_{n+1}$$

$$R = Q^{-1} D_0^{el}$$

(4.2) Convergence control. **If** $||r|| < tol$ and $f_{n+1} < tol$ **then** go to **(5)**

(4.3) Continuation of the iterative process

$$a_{n+1} = \left.\frac{\partial f}{\partial \sigma}\right|_{\sigma=\sigma_{n+1}, \bar{\sigma}_c=\bar{\sigma}_{c,n+1}, \bar{\sigma}_t=\bar{\sigma}_{t,n+1}}$$

$$H_{n+1} = H|_{\sigma=\sigma_{n+1}, \bar{\sigma}_c=\bar{\sigma}_{c,n+1}, \bar{\sigma}_t=\bar{\sigma}_{t,n+1}}$$

$$\dot{\lambda} = \frac{f_{n+1} - (a_{n+1})^T Q^{-1} r}{(a_{n+1})^T R b_{n+1} - H_{n+1}}$$

$$\lambda = \lambda + \dot{\lambda}$$

$$\dot{\sigma} = -Q^{-1}(r + \dot{\lambda} D_0^{el} b_{n+1})$$

$$\sigma_{n+1} = \sigma_{n+1} + \dot{\sigma}$$

(4.4) Return to **(4.1)**

(5) Plastic strain update

$$\varepsilon_{n+1}^{pl} = \varepsilon_n^{pl} + \lambda b_{n+1}$$

(6) If necessary, update tangent matrix

$$D^{ep} = R - \frac{R b_{n+1} (a_{n+1})^T R}{(a_{n+1})^T R b_{n+1} - H_{n+1}}$$

(7) End

Figure 90 shows the backward-Euler algorithm schematically.

Figure 90 – Backward-Euler algorithm

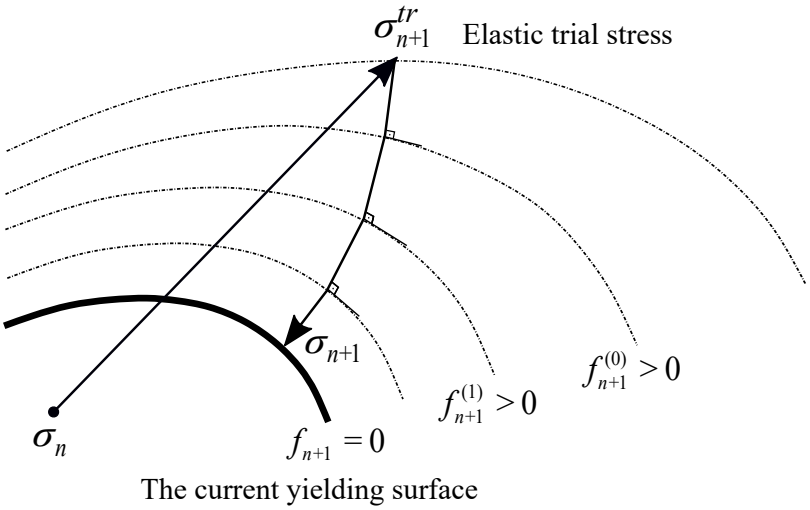

Source: adapted from Zeng, Horrigmoe, and Andersen [124].

The damage model is applied after the plasticity model has obtained plastic strain. The framework of the damaged plasticity model is briefly presented in what follows.

Algorithm 2: Damaged Plasticity Model

(1) Applies the previous plasticity model

$\bar{\sigma}$, $\dot{\tilde{\varepsilon}}^{pl}_t$ and $\dot{\tilde{\varepsilon}}^{pl}_c$ are calculated.

(2) Calculation of d_t and d_c

With $\dot{\tilde{\varepsilon}}^{pl}_t$ and tension damage evolution curve, d_t is determined.

With $\dot{\tilde{\varepsilon}}^{pl}_c$ and compression damage evolution curve, d_c is determined.

(3) Calculation of d

$$d = 1 - (1 - s_t d_c)(1 - s_c d_t)$$

(4) Calculation of Cauchy stress

$$\sigma = (1 - d)\bar{\sigma}$$

(5) End.

7.2.3 Numerical validation

UMAT subroutine was validated through numerical tests developed in Abaqus® and the response obtained was compared with that acquired by CDP.

The data adopted in the constitutive model were:$f_c = 40MPa$, $f_t = 3MPa$, $E = 30000MPa$, $\nu = 0.2$, $\phi = 30^{o}$, $\epsilon = 0.1$, $f_b/f_c = 1.16$, $kc = 0.67$, $\mu = 0$, $w_t = 0$, and $w_c = 1$.

The tension and compression curves adopted were proposed by Carreira and Chu [126] and Carreira and Chu [101], respectively, and the evolution curves for tension and compression damage were presented in Birtel and Mark [127]. Figure 91 shows the model's input curves.

Figure 91 – Model's input curves

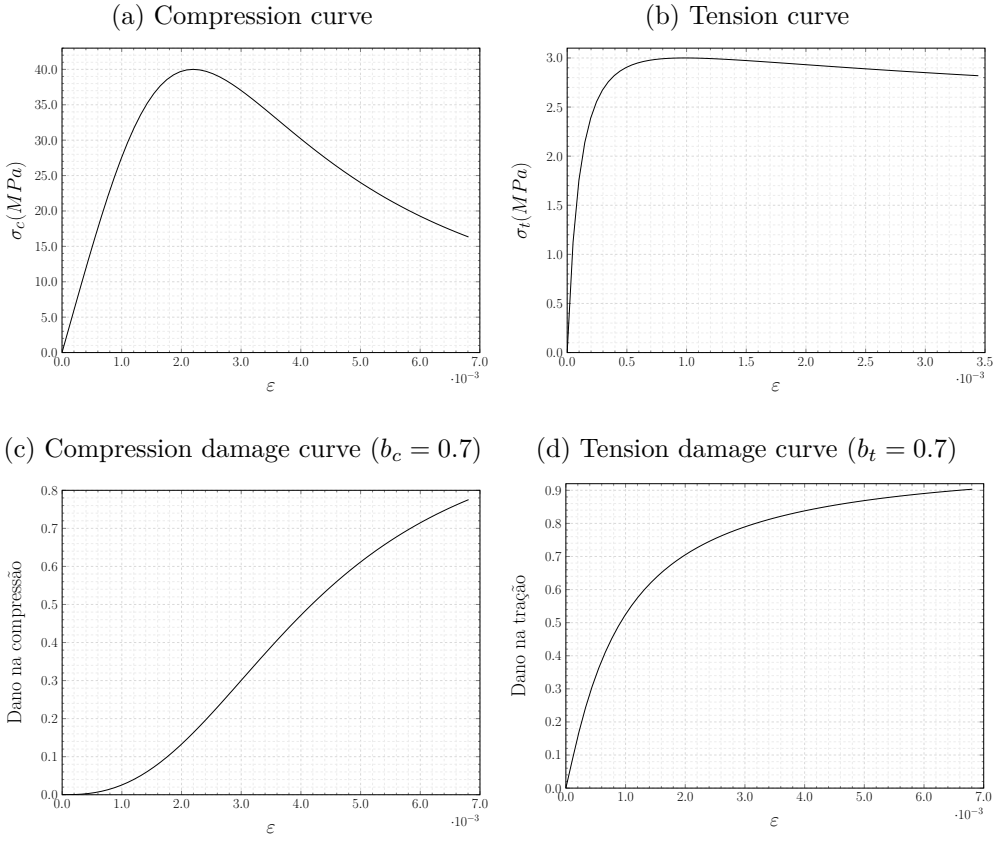

Source: the author.

Backward-Euler algorithm, used in the plasticity model, adopted 10^{-10} tolerance and 100 as the maximum number of iterations.

A cube of 100 mm side was used in the numerical tests and the finite element size was 25 mm. C3D8 element, which has eight nodes per element and complete integration, was employed in the model. The following figures show some results

Figure 92 – UMAT validation

(a) Compression

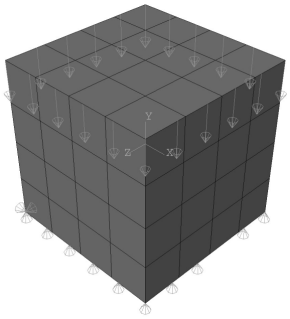

(b) Result

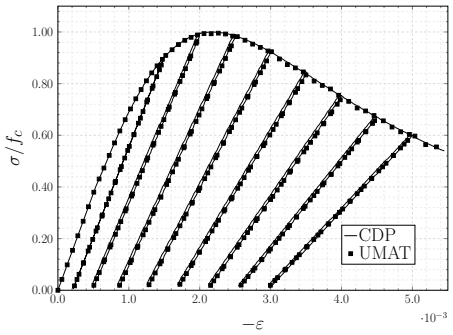

(c) Tension

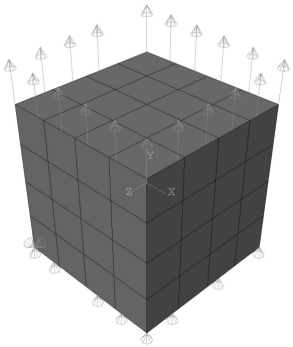

(d) Resultt

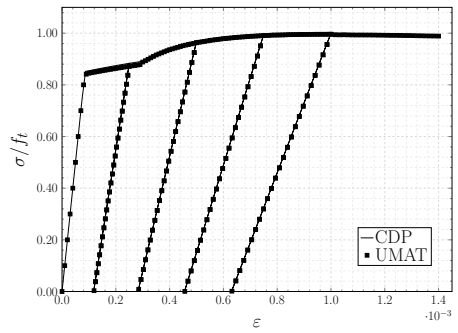

(e) Tension-compression-tension test

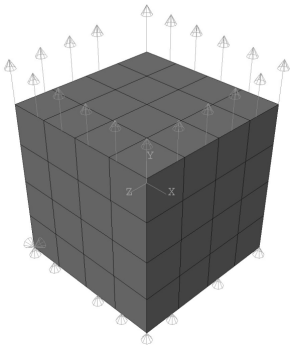

(f) Result

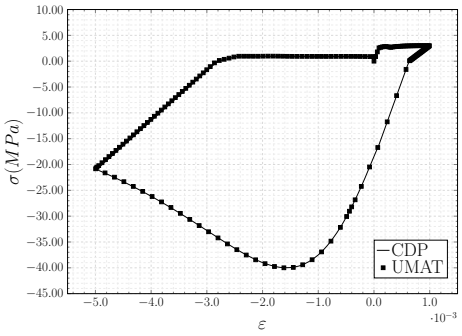

(g) Confinement

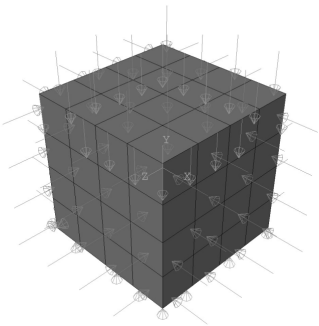

(h) Result

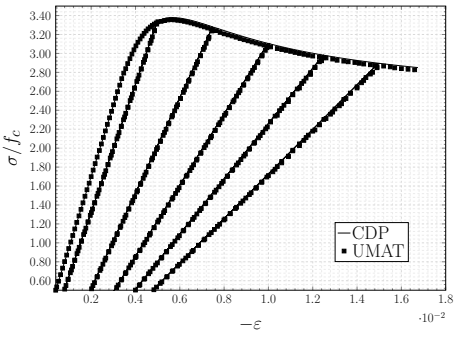

Source: the author.

7.2.4 Validation with experimental bending test

The constitutive model simulated the bending test presented in chapter 6. Figure 93 depicts the numerical model designed by Abaqus. The mesh adopted was composed of 9074 elements of C3D8 type. Displacement was applied in the middle of the span in the simulation (see fig. 93).

Figure 93 – Numerical model - three-point bending test

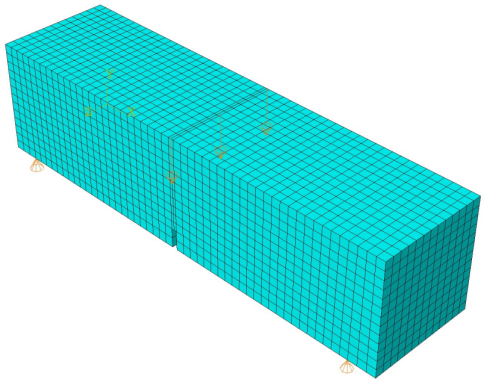

Source: the author.

Table 20 shows the input data of the constitutive model obtained experimentally. ξ and $\bar{\beta}$ were calibrated. Note the value of bond strength τ is low. Regions of weakness are probably formed in areas where the fibers are more clustered, limiting the composite's strength.

Table 20 – Input data in the numerical model

Parameter	UHPFRC-1 (η_θ=0.680)	UHPFRC-1 (η_θ=0.746)	UHPFRC-1 (η_θ=0.797)	UHPFRC-2 (η_θ=0.699)	UHPFRC-2 (η_θ=0.753)	UHPFRC-2 (η_θ=0.810)
E_f (MPa)	200000	200000	200000	200000	200000	200000
V_f	1%	1%	1%	2%	2%	2%
τ (MPa)	8	8	8	8	8	8
ξ	0.10	0.70	1.0	0.40	0.60	0.75
$\bar{\beta}$	-0.07	-0.07	0	-0.07	0	0
L_f (mm)	13	13	13	13	13	13
d_f(mm)	0.2	0.2	0.2	0.2	0.2	0.2
η_θ	0.680	0.746	0.797	0.699	0.753	0.810
E_m (MPa)	41230	41230	41230	41230	41230	41230
f_{mt} (MPa)	6.86	6.86	6.86	6.86	6.86	6.86
G_{Fm}(N/mm)	0.04	0.04	0.04	0.04	0.04	0.04

Source: the author.

Figures 94 and 95 show the curves obtained by both numerical and experimental models. The numerical model can capture the effect of fiber content and orientation.

Figure 94 – Numerical and experimental results of the bending test

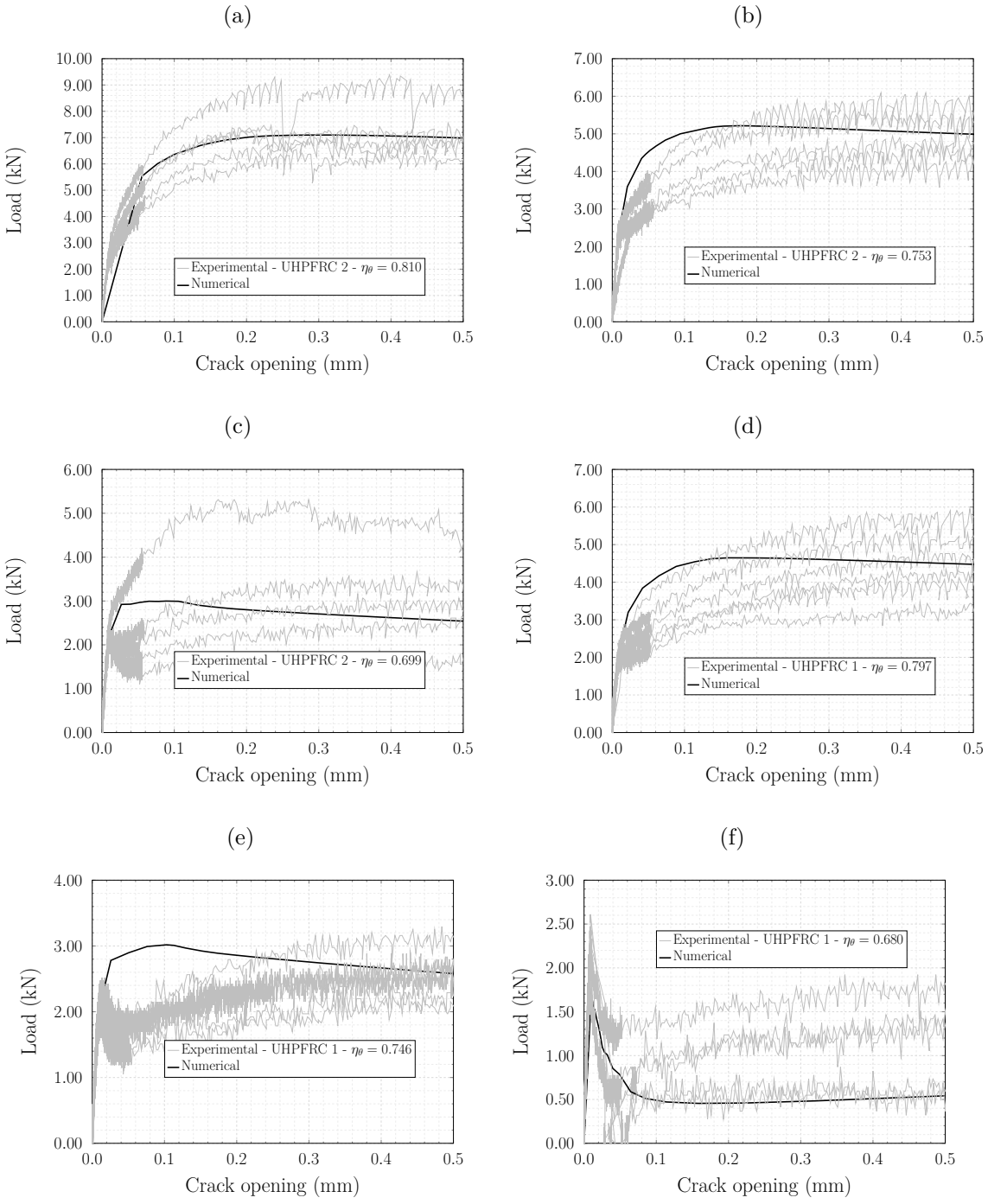

Source: the author.

Figure 95 – Numerical results of the bending test

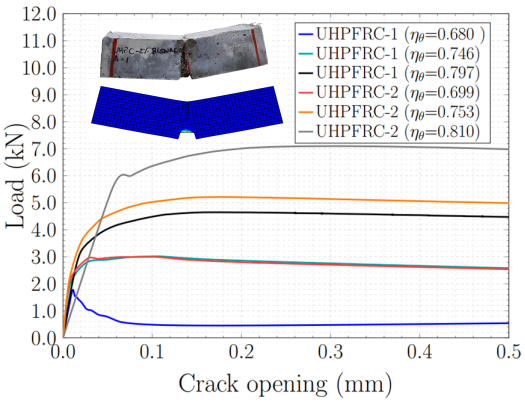

Source: the author.

7.3 Modified CDP model for UHPFRC

A modification was introduced in the algorithm after the stresses had been calculated and before the yield function had been verified. The user must provide the orientation coefficient in three known orthogonal axes that constitute the vector $(\eta_{\theta 1}, \eta_{\theta 2}, \eta_{\theta 3})$. The model automatically calculates the principal tensile stress direction for each integration point and the corresponding orientation coefficient. First, the orientation coefficient is obtained by the dot product between the vector $(\eta_{\theta 1}, \eta_{\theta 2}, \eta_{\theta 3})$ and the direction vector referring to the principal tensile stress. The tensile curve used in the yield function is then adopted according to the orientation coefficient calculated. UMAT is called at every increment throughout the analysis and integration point and the yielding criteria are initially checked. The material response is then calculated with elastic or plastic behavior.

The model was applied in the simulation of the test of a notched UHPFRC specimen under wedge split loading, as in Qsymah [12]. Figure 96 displays the specimen dimensions and the test setup.

Figure 96 – (a) Specimen dimensions (b) Wedge split test setup

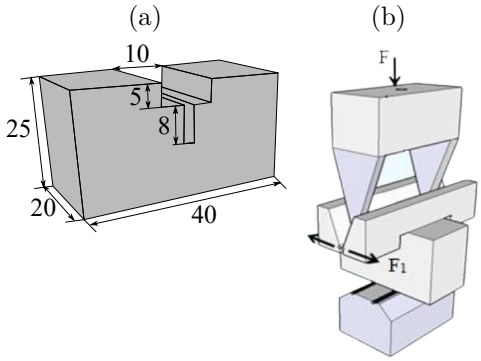

Source: Qsymah [12].

The mortar was reinforced with 2% straight steel fibers of 13mm length, 0.2mm diameter, 2000MPa strength, and 200GPa elastic modulus. The basic properties of the material at 28 days from standard tests were 150.56MPa compression strength, 9.07MPa tensile strength, and 45.55 GPa Young's modulus, whereas UHPC showed 121.32 MPa, 5.36 MPa, and 42.08GPa, respectively. Microscale X-ray computed tomography (μXCT) visualized and analyzed the internal micro-structures of the composite. The distribution of the fiber orientations was investigated and the orientation coefficients with respect to x-, y-, and z-axes were 0.64, 0.30, and 0.56, respectively (see fig. 97).

Figure 97 – Distribution of fibers obtained by μXCT

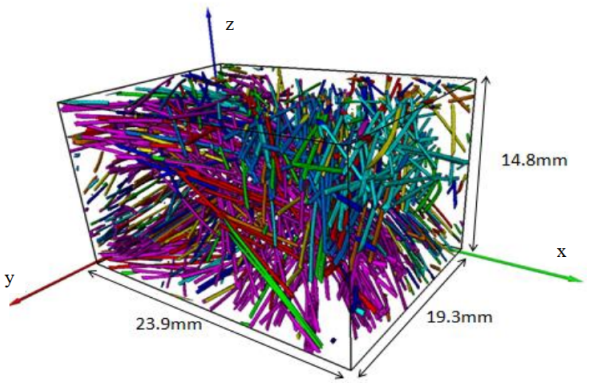

Source: Qsymah [12].

Table 21 shows the constitutive model input data. The numerical model was composed of 18680 finite elements of type C3D8, as illustrated in fig. 98.

Table 21 – Model input data

V_f (%)	τ (MPa)	ξ	$\bar{\beta}$	E_m (GPa)	f_{mt} (MPa)	$\eta_{\theta x}$	$\eta_{\theta y}$	$\eta_{\theta z}$
2	8	0.30	-0.10	42.08	5.36	0.64	0.56	0.30

Source: the author.

Figure 98 – Mesh and boundary conditions of the numerical model

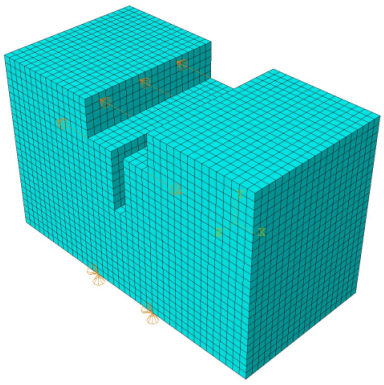

Source: the author.

Figure 99 shows the results from the numerical model designed in the present study, by the experimental and two-phase numerical models developed by Qsymah [12]. The results are consistente and the homogeneous model offers advantages in terms of computational cost. The model with no fibers was also evaluated. The positive effect of the fibers can be easily visualized. Figure 100 displays the cracking pattern of numerical and experimental models.

Figure 99 – Numerical model result

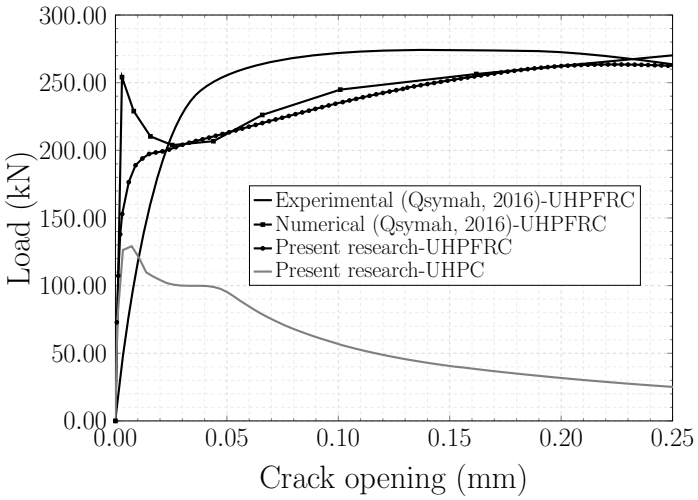

Source: the author.

Figure 100 – Cracking pattern (a) numerical model (b) experimental model

(a)

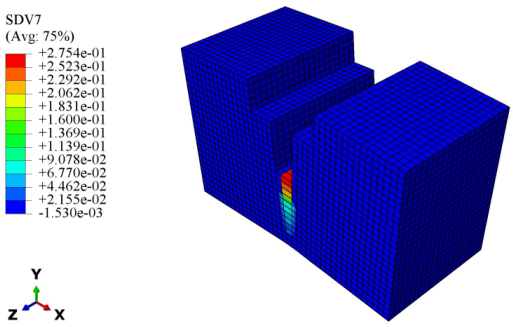

(b)

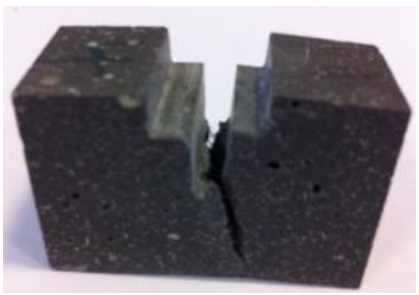

Source: a) the author b) Qsymah [12].

7.4 Potential and limitations of the developed model and proposals for future research

This item aims to evaluate the potential of the constitutive model proposed in chapter 5 in the simulation of elements subjected to shear stress. The UMAT subroutine developed simulates only simple concrete samples; however, the literature reports no study that tested UHPFRC samples subjected to shear stress with the fiber orientation characterization. Therefore, CDP, implemented in Abaqus, evaluated the shear strength of reinforced UHPFRC beams.

Voo, Poon and Foster [128] performed tests on shear in prestressed UHPFRC beams with no stirrups. Figure 101 shows the support positioning and the load application on simulated 8.6m long beams X-B1, X-B2, and X-B3, pre-tensioned with a 200 kN force per strand. Figure 102 displays the cross-section of the beam.

Figure 101 – Positioning of supports and application of loading

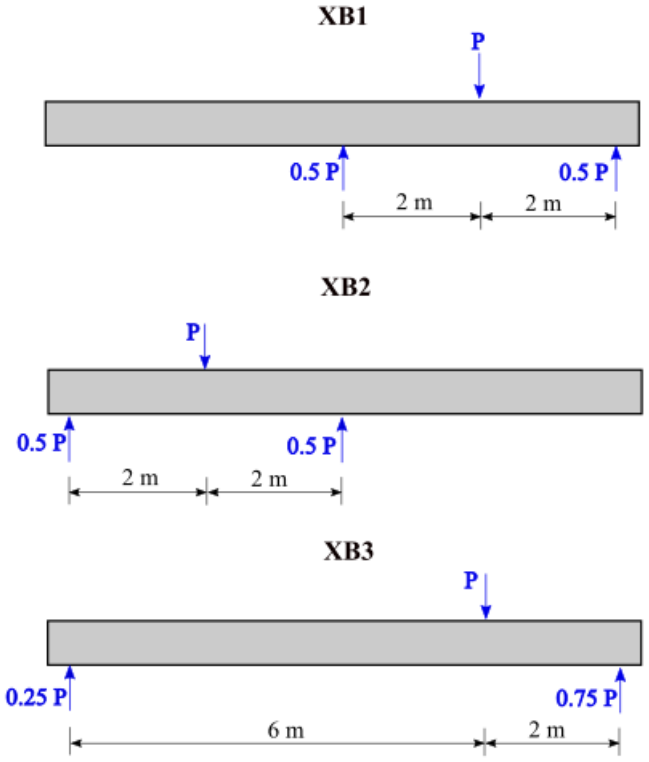

Source: the author.

Figure 102 – Cross section of prestressed UHPC test specimens

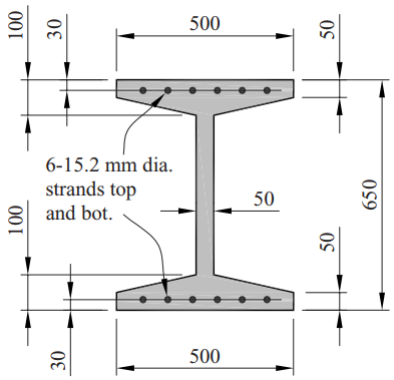

Source: Voo, Poon and Foster [128].

Table 22 shows the details of the UHPC mix designs adopted. The steel fibers used were a straight wire of 0.2 mm diameter and 15 mm length.

Table 22 – Mix Designs Material Quantities in kg per m^3 of UHPC

Component	XB-1	XB-2	XB-3
Cement	742	742	742
Fine sand	1100	1100	1100
Silica fume	149	149	149
Superplasticizer	40	40	40
Steel fiber	80	80	80
Total water	151	151	151
Total fiber ratio (%)	1	1	1
Curing regime	air cured only	air cured only	2 days head treatment in 90žC

Source: the author.

Figure 103 illustrates the numerical model developed. The concrete was modeled as a solid element C3D8R, which has eight nodes and three degrees of freedom per node, translations in main x, y, and z directions, and reduced integration. Steel bars were modeled as a T3D2 truss element with two nodes and totally embedded into the solid element (Concrete – C3D8R).

Figure 103 – Numerical model: mesh, boundary conditions, and steel bars

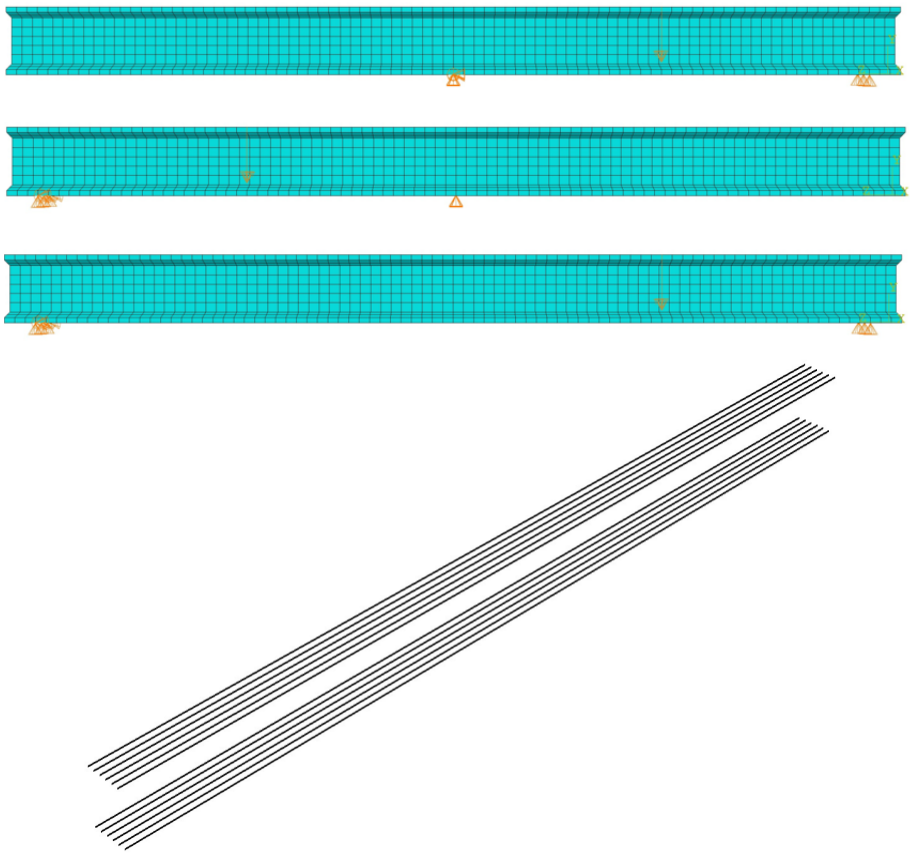

Source: the author.

The material was defined by CDP constitutive model. The model proposed by Chi et al. [99] was considered for compression behavior. The plasticity parameters of CDP were adopted according to Krahl, Carrazedo, and El Debs [2] and the micromechanical model developed in chapter 5 was used for the stress-crack opening tensile curve. The input data of the constitutive model, shown in table table 23, were adopted according to Voo, Poon, and Foster [128]. Only $\bar{\beta}$ and f_{mt} values were calibrated. The prestressing was simulated by applying a 1398.60 MPa stress, defined in the "predefined field" of Abaqus, in the axial reinforcement direction in a step preliminary to the load application.

Figure 104 shows a comparison between experimental and numerical results. Since no experimental fiber orientation analysis was performed, beams whose orientation coefficient ranged between 0.70 and 0.90, were simulated. A 0.80 orientation coefficient represented the experimental response well. The results were satisfactory, confirming the high potential of the proposed constitutive model. Therefore, the development of UMAT subroutine should continue towards its use in reinforced concrete elements and other states of stress whose direction and location of cracks are not previously known should be investigated. Moreover, experimental tests must be conducted with a complete description of the orientation of the fibers for the validation of future numerical developments.

Table 23 – Input data of the constitutive model

Property	XB-1	XB-2	XB-3
f_{cm} (MPa)	125	126	135
V_f(%)	1	1	1
$\xi \cdot \tau$ (MPa)	6.71	6.73	6.95
L_f (mm)	15	15	15
d_f (mm)	0.2	0.2	0.2
$\bar{\beta}$	-0.07	-0.07	-0.07
E (GPa)	40	40	42.3
f_{cf} (MPa)	13	15.6	13.6
f_{mt} (MPa)	8	8.5	8

Source: the author.

Figure 104 – Numerical and experimental results

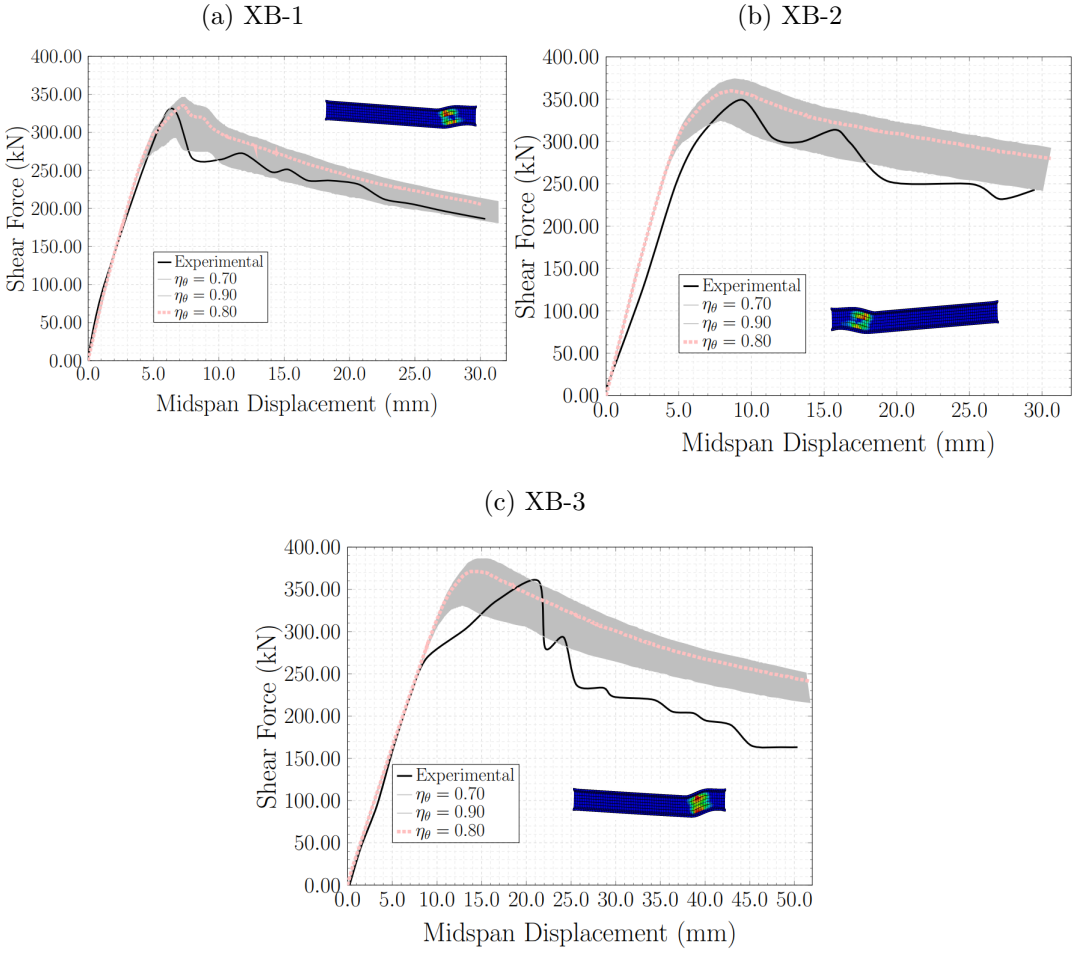

Source: the author.

7.5 Conclusions

This chapter addressed the capacity of the model proposed in chapter 5, initially developed to simulate the uniaxial tensile behavior of UHPFRC, for representing other states of stress and the following advances and conclusions have been reached:

- The constitutive model presented in chapter 5 is used in the CDP model as the tensile curve that represents the material. Conventional CDP is implemented in Abaqus commercial software. However, in this study, it was implemented via a UMAT subroutine in Fortran language towards a better understanding of it and modifications that enable a more realistic representation of UHPFRC. In the first stage of the research, CDP was implemented and later validated with numerical examples and the experimental bending tests presented in chapter 6.

- After the validation of the conventional CDP, modifications were made to UMAT subroutine towards overcoming the limitation of current models, i.e., the need for a previous knowledge of the location of the crack. The model automatically calculates the principal tensile stress direction for each integration point and the corresponding orientation coefficient. Finally, each integration point is analyzed with the tensile curve corresponding to the orientation coefficient considered at the point. As input, the average orientation of the fibers must be known in three orthogonal directions. The model was validated by the experimental wedge split test developed by Qsymah [12] and the results proved satisfactory. The author's study was the only one found in the literature that provided all input data, including a complete characterization of fiber distribution.

- Finally, the model developed in Chapter 5 simulated reinforced UHPFRC beams on the shear towards analyses of its ability for representing the UHPFRC shear behavior well. The results were satisfactory. As future research, the development of the UMAT subroutine should be continued and validated with other stress states.

EIGHT

CONCLUSIONS

A summary of the main conclusions and contributions of the study is presented below.

8.1 Effect of fibers on the dynamic properties of UHPFRC

The influence of the concrete pouring procedure on fiber orientation, obtained through image analysis, and on natural frequencies of UHPFRC samples were evaluated. Natural frequencies were obtained by an impact acoustic test guided by a modal analysis performed with the aid of a finite element model. The study showed the natural frequencies of samples with same geometry and fiber content can be statistically different in function of type of pouring procedure, indicating UHPFRC displays an anisotropic behavior, i.e., the material properties are dependent on the direction. The calibration of the numerical model was based on experimental natural frequencies considering two hypotheses for the material: isotropic or orthotropic. The orthotropic material provided the best fit between numerical and experimental models for all samples. The study has also demonstrated the concrete placement methodology and fiber arrangement must be taken into account in projects in which the dynamic properties of UHPFRC are important.

8.2 Effect of fibers on the elastic properties of UHPFRC

The effect of fibers on the elastic properties of UHPFRC was studied through a two-phase modeling of representative volume elements with different arrangements and fiber content and by the homogenization technique. Homogenization enables the replacement of a heterogeneous material by a homogeneous one that exhibits the same mechanical behavior globally. The application of appropriate boundary conditions promoted the determination of the equivalent elastic constants of the composite. The results showed the composite

behavior approaches isotropic in the case of fibers randomly distributed in the sample. However, with the likely preferred orientation of the fibers related to a given direction, the material tends to display an orthotropic or transversely isotropic behavior. The data provided by homogenization and the use of regression enabled the proposal of expressions that correlate elastic constants with both content and orientation of fibers. This study has contributed to the understanding of a composite behavior in the elastic phase and estimation of elastic constants in the design of UHPFRC structures.

8.3 Experimental evaluation of the mechanical behavior of UHPFRC

The samples subjected to an impact acoustic test were also subjected to compression, tension, and bending tests, thus enabling evaluations of the influence of fiber orientation on the mechanical response of UHPFRC. Fibers preferentially aligned with the tensile direction improved the tensile strength of samples with 1% and 2% fibers by 14% and 28%, respectively, and flexural strength more than doubled for fibers preferentially aligned with the tensile direction. According to the results, the tensile and flexural strength of the material is susceptible to fiber arrangement, hence, concrete placement methodology. Therefore, the arrangement of fibers must be considered when, for example, the strength of structural elements of UHPFRC are estimated.

The group effect was evaluated by a pullout test with multiple fibers and the results clearly showed the smaller the spacing between fibers, the greater the interaction between them, and the lower the fiber-matrix bond strength. The influence of matrix strength on bond strength was also evaluated and revealed higher when the fiber was immersed in a matrix with fibers. Therefore, the use of the results obtained by the single-fiber pullout in numerical modeling possibly overestimates the strength of the material. Few studies have addressed the group effect, thus showing the contribution of this thesis to this research area. However, more studies that consider, for example, multiple and inclined fibers in the group effect in the design of UHPFRC structures should be condudted.

8.4 Micromechanics-based constitutive modeling for UHPFRC

Initially, a homogeneous numerical model that considers various phenomena, such as fiber pullout, fiber content and orientation, group effect, and matrix strength based on micromechanics was developed towards simulating UHPFRC under tension. The group effect was evaluated through the calibration of the numerical model based on experimental results of UHPFRC samples under tension available in the literature. The results showed the importance of considering such an effect in both fiber-matrix bond strength and tensile response of the material. After the experimental stage, the constitutive model was adopted in the simulation of a three-point bending test. It represented the effect of orientation and

fiber content on the mechanical response of the composite, showing excellent agreement with the experimental results.

Finally, a modification was made in the CDP model so that the material dependence of fiber orientation could be considered in an automated way. Therefore, the model automatically calculates the principal tensile stress direction for each integration point and the corresponding orientation coefficient. Each integration point is then analyzed with the tensile curve corresponding to the orientation coefficient at the point. As input, the average orientation of the fibers must be known in three orthogonal directions. The model was validated by the experimental wedge split test performed by Qsymah [12] and the results proved satisfactory.

The major contributions of the thesis are a gain in confidence in the methodology for evaluating and predicting the UHPFRC behavior. Besides, considering fiber arrangement and group effect on evaluations and prediction of material behavior is very important. Studies that develop a consistent methodology for understanding the composite meso and micromechanical behavior help also solve the problem on a macroscale, contributing to the wide use of the material in real structures.

8.5 Proposals for future research

Some suggestions for future research include:

- **UMAT subroutine:** (i) adjustments necessary for the use of the subroutine in simulations of structural elements of reinforced concrete; (ii) improvement in the code for ensuring efficiency in terms of computational cost; (iii) investigation on the capacity of the constitutive model for representing other states of stress not validated in the present research; (iv) representation of non-homogeneity in the distribution of fibers.
- **Experimental tests:** tests on UHPFRC samples under shear and other states of stress different from those presented in this study with a complete characterization of the fiber arrangement for the validation and development of the constitutive model.
- **Multiple fiber pullout tests:** investigation on the group effect, evaluating other fiber cluster configurations such as testing of fibers inclined at different angles.

REFERENCES

1 FEHLING, E.; SCHMIDT, M.; WALRAVEN, J.; LEUTBECHER, T.; FRÖHLICH, S. **Ultra-high performance concrete UHPC: Fundamentals, design, examples**. [S.l.]: John Wiley & Sons, 2014.

2 KRAHL, P. A.; CARRAZEDO, R.; DEBS, M. K. E. Mechanical damage evolution in uhpfrc: experimental and numerical investigation. **Engineering Structures**, Elsevier, v. 170, p. 63–77, 2018.

3 DUQUE, L. F. M.; GRAYBEAL, B. Fiber orientation distribution and tensile mechanical response in uhpfrc. **Materials and Structures**, Springer, v. 50, n. 1, p. 1–17, 2017.

4 OLIVEIRA, C. O. **Estudo numérico e experimental da distribuição das fibras de aço em vigas de UHPFRC**. 2019. Tese (Doutorado) — Universidade de São Paulo, 2019.

5 KANG, S.-T.; KIM, J.-K. The relation between fiber orientation and tensile behavior in an ultra high performance fiber reinforced cementitious composites (uhpfrcc). **Cement and Concrete Research**, Elsevier, v. 41, n. 10, p. 1001–1014, 2011.

6 DUQUE, L. F. M.; GRAYBEAL, B. Fiber orientation distribution and tensile mechanical response in uhpfrc. **Materials and Structures**, Springer, v. 50, n. 1, p. 1–17, 2017.

7 WILLE, K.; NAAMAN, A. E. Fracture energy of uhp-frc under direct tensile loading. In: **FraMCoS-7 international conference**. [S.l.: s.n.], 2010. p. 65–72.

8 LI, V. C.; WANG, Y.; BACKER, S. Effect of inclining angle, bundling and surface treatment on synthetic fibre pull-out from a cement matrix. **Composites**, Elsevier, v. 21, n. 2, p. 132–140, 1990.

9 ZHOU, B.; UCHIDA, Y. Influence of flowability, casting time and formwork geometry on fiber orientation and mechanical properties of uhpfrc. **Cement and Concrete Research**, Elsevier, v. 95, p. 164–177, 2017.

10 ABRISHAMBAF, A.; PIMENTEL, M.; NUNES, S. A meso-mechanical model to simulate the tensile behaviour of ultra-high performance fibre-reinforced cementitious composites. **Composite Structures**, Elsevier, v. 222, p. 110911, 2019.

11 JR, L. A. B.; MANZOLI, O. L.; BITTENCOURT, T. N.; VECCHIO, F. J. Numerical modeling of steel fiber reinforced concrete with a discrete and explicit representation of steel fibers. **International Journal of Solids and Structures**, Elsevier, v. 159, p. 171–190, 2019.

12 QSYMAH, A. M. **In-situ X-ray Computed Tomography Tests and Numerical Modelling of Ultra High Performance Fibre Reinforced Concrete**. [S.l.]: The University of Manchester (United Kingdom), 2016.

13 CUNHA, V. M.; BARROS, J. A.; SENA-CRUZ, J. An integrated approach for modelling the tensile behaviour of steel fibre reinforced self-compacting concrete. **Cement and Concrete Research**, Elsevier, v. 41, n. 1, p. 64–76, 2011.

14 SOETENS, T.; MATTHYS, S.; TAERWE, L.; GYSEL, A. V. Basis of a finite-element simulation tool to predict the flexural behavior of sfrc prisms. In: **High Performance Fiber Reinforced Cement Composites 6**. [S.l.]: Springer, 2012. p. 91–98.

15 KANG, S.-T.; LEE, Y.; PARK, Y.-D.; KIM, J.-K. Tensile fracture properties of an ultra high performance fiber reinforced concrete (uhpfrc) with steel fiber. **Composite Structures**, Elsevier, v. 92, n. 1, p. 61–71, 2010.

16 DUTRA, V. P.; MAGHOUS, S.; FILHO, A. C. A homogenization approach to macroscopic strength criterion of steel fiber reinforced concrete. **Cement and concrete research**, Elsevier, v. 44, p. 34–45, 2013.

17 LEE, S.-C.; CHO, J.-Y.; VECCHIO, F. J. Diverse embedment model for steel fiber-reinforced concrete in tension: model development. **ACI materials Journal**, American Concrete Institute, v. 108, n. 5, p. 516, 2011.

18 LI, V. C. Postcrack scaling relations for fiber reinforced cementitious composites. **Journal of materials in civil engineering**, American Society of Civil Engineers, v. 4, n. 1, p. 41–57, 1992.

19 P18-470, N. **Concrete-Ultra-High Performance Fiber-Reinforced Concrete-Specifications, performance, production and conformity**. [S.l.]: AFNOR-French standard institute, 2016.

20 DU, S.; ZHOU, Y.; SUN, H.; LIU, W.; LUAN, C.; YUAN, L.; WANG, J.; DU, P.; ZHOU, Z.; CHENG, X. The effect of silane surface treatment on the mechanical properties of uhpfrc. **Construction and Building Materials**, Elsevier, v. 304, p. 124580, 2021.

21 ZHOU, Z.; QIAO, P. Tensile behavior of ultra-high performance concrete: Analytical model and experimental validation. **Construction and Building Materials**, Elsevier, v. 201, p. 842–851, 2019.

22 FU, S.-Y.; YUE, C.-Y.; HU, X.; MAI, Y.-W. Analyses of the micromechanics of stress transfer in single-and multi-fiber pull-out tests. **Composites science and technology**, Elsevier, v. 60, n. 4, p. 569–579, 2000.

23 ABRISHAMBAF, A.; PIMENTEL, M.; NUNES, S. Influence of fibre orientation on the tensile behaviour of ultra-high performance fibre reinforced cementitious composites. **Cement and Concrete Research**, Elsevier, v. 97, p. 28–40, 2017.

24 KRAHL, P. A.; GIDRÃO, G. d. M. S.; NETO, R. B.; CARRAZEDO, R. Effect of curing age on pullout behavior of aligned and inclined steel fibers embedded in uhpfrc. **Construction and Building Materials**, Elsevier, v. 266, p. 121188, 2021.

25 LARANJEIRA, F.; AGUADO, A.; MOLINS, C. Predicting the pullout response of inclined straight steel fibers. **Materials and structures**, Springer, v. 43, n. 6, p. 875–895, 2010.

26 LEUNG, C. K.; SHAPIRO, N. Optimal steel fiber strength for reinforcement of cementitious materials. **Journal of Materials in Civil Engineering**, American Society of Civil Engineers, v. 11, n. 2, p. 116–123, 1999.

27 LEE, Y.; KANG, S.-T.; KIM, J.-K. Pullout behavior of inclined steel fiber in an ultra-high strength cementitious matrix. **Construction and Building Materials**, Elsevier, v. 24, n. 10, p. 2030–2041, 2010.

28 HUANG, H.; GAO, X.; TENG, L. Fiber alignment and its effect on mechanical properties of uhpc: An overview. **Construction and Building Materials**, Elsevier, v. 296, p. 123741, 2021.

29 PAE, J.; KANG, S.-H.; LEE, N.; KIM, S.; MOON, J. Flow distance induced variation analysis of digitally segmented steel fibers in uhpfrc. **Construction and Building Materials**, Elsevier, v. 303, p. 124515, 2021.

30 ŠVEC, O.; ŽIRGULIS, G.; BOLANDER, J. E.; STANG, H. Influence of formwork surface on the orientation of steel fibres within self-compacting concrete and on the mechanical properties of cast structural elements. **Cement and Concrete Composites**, Elsevier, v. 50, p. 60–72, 2014.

31 BASTIEN-MASSE, M.; DENARIÉ, E.; BRÜHWILER, E. Effect of fiber orientation on the in-plane tensile response of uhpfrc reinforcement layers. **Cement and Concrete Composites**, Elsevier, v. 67, p. 111–125, 2016.

32 ZHOU, B.; UCHIDA, Y. Relationship between fiber orientation/distribution and post-cracking behaviour in ultra-high-performance fiber-reinforced concrete (uhpfrc). **Cement and Concrete Composites**, Elsevier, v. 83, p. 66–75, 2017.

33 WILLE, K.; TUE, N. V.; PARRA-MONTESINOS, G. J. Fiber distribution and orientation in uhp-frc beams and their effect on backward analysis. **Materials and structures**, Springer, v. 47, n. 11, p. 1825–1838, 2014.

34 KIM, J.-J.; YOO, D.-Y. Effects of fiber shape and distance on the pullout behavior of steel fibers embedded in ultra-high-performance concrete. **Cement and Concrete Composites**, Elsevier, v. 103, p. 213–223, 2019.

35 HUO, L.; BI, J.; ZHAO, Y.; WANG, Z. Constitutive model of steel fiber reinforced concrete by coupling the fiber inclining and spacing effect. **Construction and Building Materials**, Elsevier, v. 280, p. 122423, 2021.

36 CHAN, Y.-W.; CHU, S.-H. Effect of silica fume on steel fiber bond characteristics in reactive powder concrete. **Cement and concrete research**, Elsevier, v. 34, n. 7, p. 1167–1172, 2004.

37 BENTUR, A.; MINDESS, S. **Fibre reinforced cementitious composites**. [S.l.]: Crc Press, 2006.

38 SHEN, X.; BRÜHWILER, E. Influence of local fiber distribution on tensile behavior of strain hardening uhpfrc using ndt and dic. **Cement and Concrete Research**, Elsevier, v. 132, p. 106042, 2020.

39 BANTHIA, N.; SAPPAKITTIPAKORN, M. Toughness enhancement in steel fiber reinforced concrete through fiber hybridization. **Cement and concrete research**, Elsevier, v. 37, n. 9, p. 1366–1372, 2007.

40 BANTHIA, N.; MAJDZADEH, F.; WU, J.; BINDIGANAVILE, V. Fiber synergy in hybrid fiber reinforced concrete (hyfrc) in flexure and direct shear. **Cement and Concrete Composites**, Elsevier, v. 48, p. 91–97, 2014.

41 YOO, D.-Y.; KIM, S.-W.; PARK, J.-J. Comparative flexural behavior of ultra-high-performance concrete reinforced with hybrid straight steel fibers. **Construction and Building Materials**, Elsevier, v. 132, p. 219–229, 2017.

42 CHUN, B.; YOO, D.-Y. Hybrid effect of macro and micro steel fibers on the pullout and tensile behaviors of ultra-high-performance concrete. **Composites Part B: Engineering**, Elsevier, v. 162, p. 344–360, 2019.

43 YU, J.; CHEN, Y.; LEUNG, C. K. Micromechanical modeling of crack-bridging relations of hybrid-fiber strain-hardening cementitious composites considering interaction between different fibers. **Construction and Building Materials**, Elsevier, v. 182, p. 629–636, 2018.

44 MINDEGUIA, J.-C.; PIMIENTA, P.; NOUMOWÉ, A.; KANEMA, M. Temperature, pore pressure and mass variation of concrete subjected to high temperature—experimental and numerical discussion on spalling risk. **Cement and concrete research**, Elsevier, v. 40, n. 3, p. 477–487, 2010.

45 LI, Y.; ZHANG, D. Effect of lateral restraint and inclusion of polypropylene and steel fibers on spalling behavior, pore pressure, and thermal stress in ultra-high-performance concrete (uhpc) at elevated temperature. **Construction and Building Materials**, Elsevier, v. 271, p. 121879, 2021.

46 LI, Y.; TAN, K. H.; YANG, E.-H. Synergistic effects of hybrid polypropylene and steel fibers on explosive spalling prevention of ultra-high performance concrete at elevated temperature. **Cement and Concrete Composites**, Elsevier, v. 96, p. 174–181, 2019.

47 DING, Y.; ZHANG, C.; CAO, M.; ZHANG, Y.; AZEVEDO, C. Influence of different fibers on the change of pore pressure of self-consolidating concrete exposed to fire. **Construction and Building Materials**, Elsevier, v. 113, p. 456–469, 2016.

48 BANGI, M. R.; HORIGUCHI, T. Effect of fibre type and geometry on maximum pore pressures in fibre-reinforced high strength concrete at elevated temperatures. **Cement and Concrete Research**, Elsevier, v. 42, n. 2, p. 459–466, 2012.

49 LI, V. C. **Engineered Cementitious Composites (ECC): Bendable Concrete for Sustainable and Resilient Infrastructure**. [S.l.]: Springer, 2019.

50 YAO, J.; LEUNG, C. K. Scaling up modeling of strain-hardening cementitious composites based on beam theory: From single fiber to composite. **Cement and Concrete Composites**, Elsevier, v. 108, p. 103534, 2020.

51 CUNHA, V. M.; BARROS, J. A.; SENA-CRUZ, J. M. A finite element model with discrete embedded elements for fibre reinforced composites. **Computers & structures**, Elsevier, v. 94, p. 22–33, 2012.

52 STEPHEN, S. J.; RAPHAEL, B.; GETTU, R.; JOSE, S. Determination of the tensile constitutive relations of fiber reinforced concrete using inverse analysis. **Construction and Building Materials**, Elsevier, v. 195, p. 405–414, 2019.

53 BABY, F.; GRAYBEAL, B.; MARCHAND, P.; TOUTLEMONDE, F. Uhpfrc tensile behavior characterization: inverse analysis of four-point bending test results. **Materials and structures**, Springer, v. 46, n. 8, p. 1337–1354, 2013.

54 YU, J.; ZHANG, B.; CHEN, W.; HE, J. Experimental and multi-scale numerical investigation of ultra-high performance fiber reinforced concrete (uhpfrc) with different coarse aggregate content and fiber volume fraction. **Construction and Building Materials**, Elsevier, v. 260, p. 120444, 2020.

55 HAACH, V. G.; CARRAZEDO, R.; RIBEIRO, P. d. O.; FERREIRA, L. P. A.; ABE, I. P. Evaluation of elastic anisotropic relations for plain concrete using ultrasound and impact acoustic tests. **Journal of Materials in Civil Engineering**, American Society of Civil Engineers, v. 33, n. 2, p. 04020448, 2021.

56 SCHINDELIN, J.; ARGANDA-CARRERAS, I.; FRISE, E.; KAYNIG, V.; LONGAIR, M.; PIETZSCH, T.; PREIBISCH, S.; RUEDEN, C.; SAALFELD, S.; SCHMID, B. et al. Fiji: an open-source platform for biological-image analysis. **Nature methods**, Nature Publishing Group, v. 9, n. 7, p. 676–682, 2012.

57 KIM, S. W.; KANG, S. T.; PARK, J. J.; RYU, G. S. Effect of filling method on fibre orientation and dispersion and mechanical properties of uhpc. In: **Proceedings of the 2nd International Symposium on Ultra High Performance Concrete, Kassel, Germany**. [S.l.: s.n.], 2008. p. 185–192.

58 YOO, D.-Y.; KANG, S.-T.; YOON, Y.-S. Effect of fiber length and placement method on flexural behavior, tension-softening curve, and fiber distribution characteristics of uhpfrc. **Construction and Building materials**, Elsevier, v. 64, p. 67–81, 2014.

59 KANG, S.-T.; KIM, J.-K. Investigation on the flexural behavior of uhpcc considering the effect of fiber orientation distribution. **Construction and Building Materials**, Elsevier, v. 28, n. 1, p. 57–65, 2012.

60 YOO, D.-Y.; BANTHIA, N.; YOON, Y.-S. Predicting the flexural behavior of ultra-high-performance fiber-reinforced concrete. **Cement and Concrete Composites**, Elsevier, v. 74, p. 71–87, 2016.

61 MAHMUD, G. H.; YANG, Z.; HASSAN, A. M. Experimental and numerical studies of size effects of ultra high performance steel fibre reinforced concrete (uhpfrc) beams. **Construction and Building Materials**, Elsevier, v. 48, p. 1027–1034, 2013.

62 SINGH, M.; SHEIKH, A.; ALI, M. M.; VISINTIN, P.; GRIFFITH, M. Experimental and numerical study of the flexural behaviour of ultra-high performance fibre reinforced concrete beams. **Construction and Building Materials**, Elsevier, v. 138, p. 12–25, 2017.

63 SOETENS, T.; MATTHYS, S. Different methods to model the post-cracking behaviour of hooked-end steel fibre reinforced concrete. **Construction and Building Materials**, Elsevier, v. 73, p. 458–471, 2014.

64 GAL, E.; KRYVORUK, R. Meso-scale analysis of frc using a two-step homogenization approach. **Computers & Structures**, Elsevier, v. 89, n. 11-12, p. 921–929, 2011.

65 ABAQUS, F. et al. Dassault systemes simulia corporation. **Providence, Rhode Island, USA**, 2014.

66 MOBASHER, B. **Mechanics of fiber and textile reinforced cement composites**. [S.l.]: CRC press, 2011.

67 HILL, R. Elastic properties of reinforced solids: some theoretical principles. **Journal of the Mechanics and Physics of Solids**, Elsevier, v. 11, n. 5, p. 357–372, 1963.

68 LARANJEIRA, F.; GRÜNEWALD, S.; WALRAVEN, J.; BLOM, C.; MOLINS, C.; AGUADO, A. Characterization of the orientation profile of steel fiber reinforced concrete. **Materials and structures**, Springer, v. 44, n. 6, p. 1093–1111, 2011.

69 QSYMAH, A.; SHARMA, R.; YANG, Z.; MARGETTS, L.; MUMMERY, P. Micro x-ray computed tomography image-based two-scale homogenisation of ultra high performance fibre reinforced concrete. **Construction and Building Materials**, Elsevier, v. 130, p. 230–240, 2017.

70 LUO, Q.; LIU, D.; QIAO, P.; ZHOU, Z.; ZHAO, Y.; SUN, L. Micro-ct-based micromechanics and numerical homogenization for effective elastic property of ultra-high performance concrete. **International Journal of Damage Mechanics**, SAGE Publications Sage UK: London, England, v. 29, n. 1, p. 45–66, 2020.

71 DUTRA, V. **Um modelo constitutivo para o concreto reforçado com fibras de aço via teoria da homogeneização**. 2012. Tese (Doutorado) — PhD thesis, Federal Univesity of Rio Grande do Sul/Porto Alegre, 2012.

72 HUANG, Y.; YAN, D.; YANG, Z.; LIU, G. 2d and 3d homogenization and fracture analysis of concrete based on in-situ x-ray computed tomography images and monte carlo simulations. **Engineering Fracture Mechanics**, Elsevier, v. 163, p. 37–54, 2016.

73 HYER, M.; WHITE, S. **Stress Analysis of Fiber-reinforced Composite Materials: WCB McGraw-Hill**. [S.l.]: Inc, 1998.

74 HYER, M. W. **Stress analysis of fiber-reinforced composite materials**. [S.l.]: Mc. Graw Hill, 1998.

75 COX, H. The elasticity and strength of paper and other fibrous materials. **British journal of applied physics**, IOP Publishing, v. 3, n. 3, p. 72, 1952.

76 HOANG, A. L.; FEHLING, E.; LAI, B.; THAI, D.-K.; CHAU, N. V. Experimental study on structural performance of uhpc and uhpfrc columns confined with steel tube. **Engineering Structures**, Elsevier, v. 187, p. 457–477, 2019.

77 LI, Y.; LI, Y. Evaluation of elastic properties of fiber reinforced concrete with homogenization theory and finite element simulation. **Construction and Building Materials**, Elsevier, v. 200, p. 301–309, 2019.

78 XU, Y.; LIU, J.; LIU, J.; ZHANG, P.; ZHANG, Q.; JIANG, L. Experimental studies and modeling of creep of uhpc. **Construction and Building Materials**, Elsevier, v. 175, p. 643–652, 2018.

79 KRAHL, P. A.; GIDRÃO, G. d. M. S.; CARRAZEDO, R. Compressive behavior of uhpfrc under quasi-static and seismic strain rates considering the effect of fiber content. **Construction and Building Materials**, Elsevier, v. 188, p. 633–644, 2018.

80 POURBABA, M.; ASEFI, E.; SADAGHIAN, H.; MIRMIRAN, A. Effect of age on the compressive strength of ultra-high-performance fiber-reinforced concrete. **Construction and Building Materials**, Elsevier, v. 175, p. 402–410, 2018.

81 ALSALMAN, A.; DANG, C. N.; PRINZ, G. S.; HALE, W. M. Evaluation of modulus of elasticity of ultra-high performance concrete. **Construction and Building Materials**, Elsevier, v. 153, p. 918–928, 2017.

82 YOO, D.-Y.; BANTHIA, N.; KANG, S.-T.; YOON, Y.-S. Size effect in ultra-high-performance concrete beams. **Engineering Fracture Mechanics**, Elsevier, v. 157, p. 86–106, 2016.

83 ZHANG, J.; LIU, X.; YUAN, Y.; MANG, H. A multiscale model for predicting the elasticity modulus and the strength of ultra-high performance fiber reinforced concrete. **Computational Modelling of Concrete Structures**, CRC Press, p. 159, 2014.

84 WILLE, K.; EL-TAWIL, S.; NAAMAN, A. E. Properties of strain hardening ultra high performance fiber reinforced concrete (uhp-frc) under direct tensile loading. **Cement and Concrete Composites**, Elsevier, v. 48, p. 53–66, 2014.

85 HASSAN, A.; JONES, S.; MAHMUD, G. Experimental test methods to determine the uniaxial tensile and compressive behaviour of ultra high performance fibre reinforced concrete (uhpfrc). **Construction and building materials**, Elsevier, v. 37, p. 874–882, 2012.

86 LAI, J.; SUN, W. Dynamic mechanical behaviour of ultra-high performance fiber reinforced concretes. **Journal of Wuhan University of Technology-Mater. Sci. Ed.**, Springer, v. 23, n. 6, p. 938–945, 2008.

87 THOMAS, J.; RAMASWAMY, A. Mechanical properties of steel fiber-reinforced concrete. **Journal of materials in civil engineering**, American Society of Civil Engineers, v. 19, n. 5, p. 385–392, 2007.

88 LI, V. C.; STANG, H.; KRENCHEL, H. Micromechanics of crack bridging in fibre-reinforced concrete. **Materials and structures**, Springer, v. 26, n. 8, p. 486–494, 1993.

89 LEI, D.-Y.; GUO, L.-P.; LI, Y.; LIU, J.-P.; CHEN, B.; LI, D.-X.; LI, S.-C.; MECHTCHERINE, V. Micro-mechanical model for ultra-high strength and ultra-high ductility cementitious composites (uhs-uhdcc). **Construction and Building Materials**, Elsevier, v. 267, p. 120668, 2021.

90 NF, P. P 18-470.(2016a). **Concrete—ultra-high performance fibre-reinforced concrete—specifications, performance, production and conformity, Francis de Pressensé, France**.

91 YOO, D.-Y.; KIM, J.-J.; PARK, J.-J. Effect of fiber spacing on dynamic pullout behavior of multiple straight steel fibers in ultra-high-performance concrete. **Construction and Building Materials**, Elsevier, v. 210, p. 461–472, 2019.

92 KUSUMAWARDANINGSIH, Y.; FEHLING, E.; ISMAIL, M.; ABOUBAKR, A. A. M. Tensile strength behavior of uhpc and uhpfrc. **Procedia Engineering**, Elsevier, v. 125, p. 1081–1086, 2015.

93 THAI, D.-K.; NGUYEN, D.-L.; NGUYEN, D.-D. A calibration of the material model for frc. **Construction and Building Materials**, Elsevier, v. 254, p. 119293, 2020.

94 BAHIJ, S.; ADEKUNLE, S. K.; AL-OSTA, M.; AHMAD, S.; AL-DULAIJAN, S. U.; RAHMAN, M. K. Numerical investigation of the shear behavior of reinforced ultra-high-performance concrete beams. **Structural Concrete**, Wiley Online Library, v. 19, n. 1, p. 305–317, 2018.

95 KANG, S.-T.; KIM, J.-K. Numerical simulation of the variation of fiber orientation distribution during flow molding of ultra high performance cementitious composites (uhpcc). **Cement and Concrete Composites**, Elsevier, v. 34, n. 2, p. 208–217, 2012.

96 LUBLINER, J.; OLIVER, J.; OLLER, S.; OÑATE, E. A plastic-damage model for concrete. **Int. J. Solids and Structures**, 1989.

97 LEE, J.; FENVES, G. L. Plastic-damage model for cyclic loading of concrete structures. **Journal of engineering mechanics**, American Society of Civil Engineers, v. 124, n. 8, p. 892–900, 1998.

98 FU, S.-Y.; LAUKE, B. An analytical characterization of the anisotropy of the elastic modulus of misaligned short-fiber-reinforced polymers. **Composites Science and Technology**, Elsevier, v. 58, n. 12, p. 1961–1972, 1998.

99 CHI, Y.; YU, M.; HUANG, L.; XU, L. Finite element modeling of steel-polypropylene hybrid fiber reinforced concrete using modified concrete damaged plasticity. **Engineering Structures**, Elsevier, v. 148, p. 23–35, 2017.

100 SOETENS, T.; MATTHYS, S. Implementation of fibre pull-out behaviour in a finite element model for sfrc. **Bond in concrete**, 2012.

101 CARREIRA, D. J.; CHU, K.-H. Stress-strain relationship for plain concrete in compression. In: **Journal Proceedings**. [S.l.: s.n.], 1985. v. 82, n. 6, p. 797–804.

102 HORDIJK, D. A. Local approach to fatigue of concrete. 1993.

103 CUNHA, V. **Steel fibre reinforced self-compacting concrete-from micromechanics to composite behaviour**. 2010. Tese (Doutorado) — University of Minho, Portugal, 2010.

104 STANG, H. Significance of shrinkage-induced clamping pressure in fiber-matrix bonding in cementitious composite materials. **Advanced Cement Based Materials**, Elsevier, v. 4, n. 3-4, p. 106–115, 1996.

105 NAAMAN, A. E.; NAMUR, G. G.; ALWAN, J. M.; NAJM, H. S. Fiber pullout and bond slip. i: Analytical study. **Journal of Structural Engineering**, American Society of Civil Engineers, v. 117, n. 9, p. 2769–2790, 1991.

106 PI, Z.; XIAO, H.; LIU, R.; LI, H. Combination usage of nano-sio2-coated steel fiber and silica fume and its improvement effect on sfrcc. **Composites Part B: Engineering**, Elsevier, p. 109022, 2021.

107 OH, T.; YOU, I.; BANTHIA, N.; YOO, D.-Y. Deposition of nanosilica particles on fiber surface for improving interfacial bond and tensile performances of ultra-high-performance fiber-reinforced concrete. **Composites Part B: Engineering**, Elsevier, p. 109030, 2021.

108 CHUN, B.; YOO, D.-Y.; BANTHIA, N. Achieving slip-hardening behavior of sanded straight steel fibers in ultra-high-performance concrete. **Cement and Concrete Composites**, Elsevier, v. 113, p. 103669, 2020.

109 YOO, D.-Y.; PARK, J.-J.; KIM, S.-W. Fiber pullout behavior of hpfrcc: Effects of matrix strength and fiber type. **Composite Structures**, Elsevier, v. 174, p. 263–276, 2017.

110 KIM, J.-K.; MAI, Y.-W. **Engineered interfaces in fiber reinforced composites**. [S.l.]: Elsevier, 1998.

111 BARTOS, P. Bond in fibre reinforced cements and concretes. **International Journal of Cement composites and Lightweight concrete**, Elsevier, v. 3, n. 3, p. 159–177, 1981.

112 YOO, D.-Y.; LEE, J.-H.; YOON, Y.-S. Effect of fiber content on mechanical and fracture properties of ultra high performance fiber reinforced cementitious composites. **Composite structures**, Elsevier, v. 106, p. 742–753, 2013.

113 KRAHL, P. A. **Lateral stability of ultra-high performance fiber-reinforced concrete beams with emphasis in transitory phases**. 2018. Tese (Doutorado) — Universidade de São Paulo, 2018.

114 ZHANG, H.; HUANG, Y.; YANG, Z.; XU, S.; CHEN, X. A discrete-continuum coupled finite element modelling approach for fibre reinforced concrete. **Cement and Concrete Research**, Elsevier, v. 106, p. 130–143, 2018.

115 STANDARD, A. C469/c469m-14. **Standard Test Method for Static Modulus of Elasticity and Poisson's Ratio of Concrete in Compression**, 2014.

116 VANDEWALLE, L.; NEMEGEER, D.; BALAZS, L.; PRISCO, M. D. Rilem tc 162-tdf: Test and design methods for steel fibre reinforced concrete: bending test. 2002.

117 RILEM, D. R. 50-fmc committee fracture mechanics of concrete,"determination of the fracture energy of mortar and concrete by means of three-point bending tests on notched beams". **Materials and Structures**, v. 85, n. 85, p. 285–290, 1985.

118 FU, S.-Y.; LAUKE, B. The elastic modulus of misaligned short-fiber-reinforced polymers. **Composites science and technology**, Elsevier, v. 58, n. 3-4, p. 389–400, 1998.

119 VOYIADJIS, G.; THIAGARAJAN, G. An anisotropic yield surface model for directionally reinforced metal-matrix composites. **International Journal of Plasticity**, Elsevier, v. 11, n. 8, p. 867–894, 1995.

120 HOFFARTH, C.; RAJAN, S. D.; GOLDBERG, R. K.; REVILOCK, D.; CARNEY, K. S.; DUBOIS, P.; BLANKENHORN, G. Implementation and validation of a three-dimensional plasticity-based deformation model for orthotropic composites. **Composites Part A: Applied Science and Manufacturing**, Elsevier, v. 91, p. 336–350, 2016.

121 LUCCIONI, B. M. Constitutive model for fiber-reinforced composite laminates. 2006.

122 VALENTE, R.; SINE, A.; PIMENTEL, M.; NUNES, S. Characterization of the anisotropic tensile response of ultra-high performance fibre reinforced cementitious composites.

123 SYSTEMES, D. Abaqus 2016-theory guide. 2016.

124 ZENG, L.; HORRIGMOE, G.; ANDERSEN, R. Numerical implementation of constitutive integration for rate-independent elastoplasticity. **Computational mechanics**, Springer, v. 18, n. 5, p. 387–396, 1996.

125 CARRAZEDO, R. **Mecanismos de confinamento em pilares de concreto encamisados com polímeros reforçados com fibras submetidos à flexo-compressão**. 2005. Tese (Doutorado) — Universidade de São Paulo, 2005.

126 CARREIRA, D. J.; CHU, K.-H. Stress-strain relationship for reinforced concrete in tension. In: **Journal Proceedings**. [S.l.: s.n.], 1986. v. 83, n. 1, p. 21–28.

127 BIRTEL, V.; MARK, P. Parameterised finite element modelling of rc beam shear failure. In: **ABAQUS users' conference**. [S.l.: s.n.], 2006. p. 95–108.

128 VOO, Y. L.; POON, W. K.; FOSTER, S. J. Shear strength of steel fiber-reinforced ultrahigh-performance concrete beams without stirrups. **Journal of structural engineering**, American Society of Civil Engineers, 345 E. 47 th St. New York NY 10017-2398 USA, v. 136, n. 11, p. 1393–1400, 2010.


PPG
SET


EESC • USP